Robot-based Component Testing on Software-defined Test Benches

Julian Hanke

Dissertation
zur Erlangung des akademischen Grades
Doktor der Naturwissenschaften (Dr. rer. nat.)

Universität Augsburg
University

Fakultät für Angewandte Informatik

October 2023

Robot-based Component Testing on Software-defined Test Benches

Erstgutachter:	Prof. Dr. Wolfgang Reif
Zweitgutachter:	Prof. Dr. Bernhard Bauer
Tag der mündlichen Prüfung:	19. Dezember 2023

Danksagung

Die vorliegende Dissertation entstand während meiner Arbeit als wissenschaftlicher Mitarbeiter am Institut für Software & Systems Engineering der Universität Augsburg. An dieser Stelle möchte ich meine aufrichtige Dankbarkeit gegenüber all jenen zum Ausdruck bringen, die mich unterstützt haben.

Als erstes möchte ich mich für die Betreuung und das Erstgutachten dieser Arbeit bei Herrn Prof. Dr. Wolfgang Reif ganz herzlich bedanken. Ich bin ihm für seine Unterstützung, sein Vertrauen, die spannenden Forschungsthemen und die zur Verfügung gestellte Forschungsumgebung sehr dankbar. Für die Tätigkeit als Zweitgutachter möchte ich mich bei Herrn Prof. Dr. Bernhard Bauer bedanken.

Gleichzeitig gilt mein Dank auch meinen Kolleginnen und Kollegen am Institut. Ich möchte insbesondere dem Team im Bereich Robotik meinen Dank aussprechen. Durch produktive Diskussionen und inspirierende Anregungen haben sie zu vielen großartigen Ideen beigetragen. Mein besonderer Dank gilt Daniel Bermuth, Dr. Johannes Kurth, Dr. Andreas Schierl, Martin Schörner, Matthias Stüben und Dr. Constantin Wanninger. Auch war Stefan Wolff stets eine unschätzbare Hilfe bei allen technischen Problemen in den Roboteranlagen und in der WiR-Zelle. Ich möchte auch Dr. Alwin Hofmann meinen aufrichtigen Dank aussprechen, der mich zu Beginn meiner Promotion tatkräftig unterstützt hat. Darüber hinaus möchte ich Dr. Dominik Haneberg für das aufmerksame Korrekturlesen meiner Arbeit danken. Ich möchte Alexander Poeppel für die zahlreichen konstruktiven Gespräche danken und dafür, dass er den Publikationen und Teilen dieser Arbeit den letzten sprachlichen Feinschliff verliehen hat. Des Weiteren möchte ich Julia Reichmann für die Unterstützung und die gemeinsame Zeit in der WiR-Zelle danken. Insbesondere danke ich meinem Bürokollegen Christian Eymüller für die zahlreichen fachlichen und persönlichen Gespräche sowie für die gemeinsame Zeit in der WiR-Zelle.

Ich danke allen Studierenden und wissenschaftlichen Hilfskräften, die mich tatkräftig bei meinen Forschungsarbeiten unterstützt haben. Besonderer Dank gilt Leonhard Heber, Lukas Kilian, Maximilian Müller und Tobias Thiele die eine große Hilfe waren.

Besonders möchte ich meine Eltern Jutta und Manfred Hanke würdigen, die mich kontinuierlich unterstützt und mit wertvollen Ratschlägen begleitet haben. Meine Mutter hat mich stets aufgemuntert und kulinarisch versorgt, und mein Vater hat viel Zeit und Mühe in das Korrekturlesen investiert.

Zuletzt möchte ich mich bei allen Personen bedanken, die zwar nicht namentlich genannt wurden, jedoch aktiv zur Unterstützung meiner Promotion beigetragen haben.

Julian Hanke

Abstract

The manufacturing industry has undergone significant transformations in the past, culminating in the current era of Industry 4.0. The main impact of this revolution is the transition of mass manufacturing to unique and individualized products tailored to customers' needs and preferences. Industries such as aerospace or automotive production, typically characterized by very rigid production and testing processes as a consequence of the high safety demands placed on their products, are also beginning the transition to increasingly customized production. Flexible testing methods are essential to test the diverse and complex components required by this paradigm. Robots, particularly in Non-Destructive Testing (NDT), have become valuable assets for ensuring component integrity and safety. However, destructive component testing still relies mainly on traditional, non-flexible testing machines. Industrial robots can be utilized to meet the demands of Industry 4.0 and the need for adaptability in component testing. Robots offer precision, repeatability, and adaptability, simulating real-world conditions and conducting complex tests. Robot-based software-defined test benches are characterized by their agility and adaptability through software. These systems are not bound to static test configurations. Instead, they use software to define and control test procedures, parameters, and criteria. Therefore, software-defined test benches represent a paradigm shift in the field of destructive testing in the context of Industry 4.0.

This thesis presents a holistic approach for software-defined robot-based component testing, which enables the flexible and automated destructive testing of various components using industrial robots. A versatile testing facility was realized as foundation for enabling robot-based component testing. Given the novelty of robot-based component testing, there is a lack of established practices in software development in this field. To address this shortage, a standardized testing procedure was introduced and an overarching architecture concept was developed to manage this procedure on the software-defined testing bench. The complexity of testing scenarios necessitates a systematic approach for describing motions and their sequences. A modeling framework for robot-based testing motions was introduced. Additionally, automated specimen placement is crucial for testing. The CASP (Computer Aided Specimen Placement) algorithmic approach was presented, automating specimen placement by considering reachability and applicable forces and torques of industrial robots. Four case studies were conducted to evaluate the holistic approach for software-defined robot-based component testing. The first case study was utilized to make an informed determination regarding the feasibility of employing robots in this domain. A tensile test setup on a conventional testing machine and the same setup on a robot-based test bench were compared to this end. The achieved results showed the applicability of robots for component testing in principle. In addition to this basic comparison, three further case studies with different components were evaluated. The results demonstrate the potential of robot-based testing in various real-world scenarios, highlighting the benefits of flexibility, reproducibility, and adaptability in testing complex components.

Contents

Summary. This chapter presents the potential of robot-based component testing on software-defined test benches and the open questions that exist in this regard. The research results of this thesis are presented, which contribute making robot-based component testing usable. Lastly, this chapter gives an overview of the structure of this thesis.

1 Introduction

This thesis aims to develop and implement a concept for robot-based component testing on software-defined test benches. This includes the development of methods to enable the efficient and automated testing of intricate components using robots and designing a control system for the robot-based component test bench.

In Section 1.1, the initial motivation for employing robot-based component testing on software-defined test benches is provided, along with an introduction to the objectives pursued through the approach presented in this work. The research results of this thesis are outlined in Section 1.2, and Section 1.3 offers a comprehensive overview of its structure.

1.1 Motivation

Manufacturing, often considered the backbone of economic progress, has traversed several significant phases over the years. From the use of steam power and the mechanization of production to the automation of industry, manufacturing has seen steady advancement and includes a profound transformation fueled by consumer demands for higher product quality, shorter development cycles, and customized solutions. However, the fourth industrial revolution, aptly termed Industry 4.0, is fundamentally altering the manufacturing landscape. At the heart of this transformation lies the production of complex and unique components, which are characterized by intricate designs, advanced materials, multifunctional attributes, and high precision requirements. They are omnipresent in industries ranging from aerospace, automotive, electronics, and medical devices to energy production. The modern era's reliance on these complex

components is indisputable, as they often form the core of advanced products. With the conversion of production to batch size one [87] and, consequently, unique dimensions and structures of increasingly complex components for each product, it must also be possible to adapt the testing of components flexibly. Furthermore, due to the increasing complexity of components, for example, produced through additive manufacturing, the setup for testing them is in turn also becoming more complex. The aerospace sector, e.g., is one of the promising sectors for using 3D printing technology due to the vast and numerous applications that could be adopted [67]. In this sector, as in many others, it is essential to ensure the product's functionality and safety through testing. Robots have emerged as dynamic and versatile assets in the context of component testing and Industry 4.0. Gone are the days when robots were confined to monotonous tasks on assembly lines. Today's robots have advanced sensors, control systems, and machine-learning capabilities. In the context of component testing, robots offer unique advantages and are already in use, especially in the field of Non-Destructive Testing (NDT). Robots for NDT are specialized robotic systems designed to inspect and evaluate the integrity of materials, components, or structures without causing any damage. NDT is crucial in various industries, including aerospace, automotive, construction, and other manufacturing industries, where critical components' safety and reliability is paramount. Robots have been integrated into NDT processes to enhance accuracy, efficiency, and safety while reducing human error and exposure to hazardous environments [22]. In contrast, robots are hardly used in the field of destructive component testing. In this area, standardized testing machines are still mainly used and are often tailored to specific components or groups of components. Usually, one or more linear cylinders are used to test components. Due to their design, these testing machines offer only a limited degree of freedom and are only suitable to a limited extent for more complex testing motions. For this reason, a dedicated test stand is usually built to test more complex structures. These traditional testing methods, which are often manual or semi-automated, struggle to meet the flexibility and adaptability required by the paradigm shift of Industry 4.0. and the associated components of higher complexity. Moreover, many components will be only available in small quantities, and it will not be profitable to design expensive test benches for each of these components, but it is still essential to test these components to ensure the quality of each individual component. In order to destructively test a large number of components, a flexible test setup is required that can be adapted to different component tests. Industrial robots can execute a wide range of testing procedures with unmatched precision, repeatability, and adaptability, due to the high number of movement directions and the extensive working range. They can simulate real-world conditions, subject components to varying stresses, and also perform complex tests on the components. Robot-based software-defined test benches are characterized by their agility and adaptability through software. These systems are not bound to static test configurations. Instead, they rely on software to define and control test procedures, parameters, and criteria. Therefore, software-defined test benches represent a paradigm shift in the way of destructive testing in manufacturing in the context of Industry 4.0. Software drives these test benches, allowing for dynamic configuration and adaptability. They empower manufacturers to define and redefine test procedures, parameters, and criteria on the fly.

While the concept of robot-based component testing on software-defined test benches holds immense promise, it comes with its challenges. Therefore, this thesis is based on the following central research question:

> *Which methods can be employed to enable the efficient and automated testing of intricate components using industrial robots, and how can the control system for the robot-based component test bench be programmed straightforwardly and intuitively?*

In the context of the present work, a holistic solution is presented as a viable answer to the central research question, enabling efficient and automated destructive testing of intricate components using industrial robots. The presented solutions span various technical fields, including robotics, algorithms, and software engineering. Many subordinate problems and challenges in these subject areas must be examined and solved. Combined with the holistic solution approach, research results were developed, which answer in detail the subordinate problem definitions. These results are now presented in more detail.

1.2 Main Contributions

Software-defined Robot-based Test Bench

In order to enable the efficient and automated testing of various components using robots, a concept of a flexible **software-defined robot-based test bench** for destructive component testing must be developed and realized. In this thesis, the requirements for such a new type of robot-based test bench are first presented and evaluated in a holistic manner. Based on these requirements, an exemplary realization for a robot-based testing facility with two heavy-duty industrial robots, additional sensors, and actuators is presented. The concept and the realization of such a robot-based test bench were published in [55].

Standard Testing Procedure

Besides the actual hardware realization, there is a need for software mechanisms that facilitate automatic mechanical testing to turn multi-functional industrial robots into flexible testing machines. Since robot-based component testing represents a new domain, there is hardly any experience or foundations in developing software in this domain. In order to define this domain fundamentally and to make the complexity of robot-based destructive component testing manageable, this thesis presents a **standardized testing procedure** This developed procedure outlines the core principles of software-defined robot-based component test benches, ensures test reproducibility, and represents, therefore, the basis for the further concepts developed in this work. This standardized testing procedure was published in [55].

Overarching Architecture

Flexibly testing components involves multiple robots, actors and sensors. While some processes are executed jointly, others must be executed consecutively. This can, for example, involve the coordination of the robots or the determination of the component position on the test bench. The sequence of these tasks is also determined with the help of the standardized testing procedure and has to be carried out on the developed test bench. This thesis presents an **overarching architecture** concept to manage this procedure and its execution on the software-defined testing bench.

Testing Motions

Motion Execution Sequence

The intricacy of testing scenarios encompasses multiple motions and their precise sequences. Since most robot controllers only support simple move commands, a methodical strategy is needed for describing such motions and their sequences. In this regard, this thesis introduces a modeling framework for **robot-based testing motions** and a model for structuring the **testing motion execution sequence**. The approach includes three categories of motions for robots or supplementary actuators. These concepts were partly published in [54, 55].

Using industrial robots in component testing introduces complexities in positioning the test object. Careful consideration of the object's test point reachability is crucial when placing it for testing purposes. While robots offer more flexibility compared to standard linear actuators, not every position on the test bench may be reachable. Additionally, industrial robots cannot apply the same forces and torques in all axis positions, even if a position is within reach. Therefore, a position must be calculated where the specimen can be tested, and all testing motions can be executed.

This thesis presents an approach for automatic specimen placement named CASP: Computer Aided Specimen Placement for Robot-Based Component Testing. It includes a format to map applicable forces and torques of industrial robots to positions on the test bench. Furthermore, it enables the execution of an automatic feasibility check for the required test motions and a resulting automatic specimen placement. At the time of writing the CASP approach is accepted for publishing in [56].

Basic Feasibility Check

Flexible destructive component testing represent a new field of application for robots. In order to be able to fundamentally decide whether robots are at all suitable for this domain, this must be evaluated based on a comparable example. This thesis presents a **basic feasibility check** for robot-based component testing. For this purpose, a tensile test setup on a conventional testing machine and the same setup on a robot-based test bench are compared. Parts of these results were published in [54]. In addition, the developed concepts are evaluated in three further case studies, which bring their own challenges.

The realized robot-based test bench and some of the research results obtained in this thesis have been developed in whole or in part within the research project WiR Augsburg (Wissenstransfer Region Augsburg), funded by the German Federal Ministry of Education and Research (BMBF) and the Bavarian Government.

1.3 Structure of the Thesis

Chapter 2 starts with introducing basic concepts. It gives a concise overview of material and component testing, delves into the prevalent sensor systems used for material characterization, and explains different types of motions in robotics.

In order to evaluate the proposed approach for software-defined robot-based component testing, Chapter 3 introduces four different case studies with diverse components. Each case study presents unique and component-specific challenges, which are addressed within the framework of the general approach. The basics and state-of-the-art are explained for each case study to highlight the requirements, which the software-defined

robot-based component testing bench approach must fulfill. The first case study is a tensile test, representing a classical use case for the early determination of specific properties of material components. In this case study, the results of the robot-based test bench will be compared with those of a universal testing machine. In the second case study, a bicycle frame is tested at different loading points on the frame, followed by the third case study for the evaluation of a complex testing motion on a snowboard. The fourth case study presents the test of an automotive component, which requires the simultaneous application of different forces and torques.

Chapter 4 describes the developed and realized robot-based testing facility. It outlines the particular requirements of robot-based component testing and gives a general overview of the test bench, followed by a detailed description of the plant, the robots' workspaces, and the additional integrated sensors and actuators. Finally, this chapter introduces existing concepts of robot-based and robot-assisted test benches for destructive and non-destructive testing scenarios.

In Chapter 5, the basis for the further chapters of this work is described. This chapter introduces the standardized test procedure and an overarching architecture concept to manage and realize this procedure and its included sub-steps.

The increasing need for complex tests of differing components involving multiple motions and their precise sequencing begets the need for more versatile and flexible software architectures capable of representing the entire scope of actuator motions required in component tests. In this regard, Chapter 6 introduces a modeling framework for the motions employed in robot-based component testing and their execution sequence. In addition, these concepts are compared with similar concepts from other domains.

Chapter 7 presents the approach for automatic computer-aided specimen placement (CASP) to calculate a position where a specimen can be tested in the robot-based testing facility. Additionally, it provides an overview of existing concepts for component placement in similar domains.

An overview of this approach's actual implementation is presented in Chapter 8. It first provides the necessary fundamentals and explains the implementation and execution of the actual motions and motion sequences in more detail.

The four case studies presented at the beginning are revisited in Chapter 9 to evaluate the developed approach of a software-defined robot-based testing facility.

Finally, this thesis concludes with a summary and an outlook in Chapter 10.

Summary. This chapter describes the basic concepts of material and component testing, sensor systems, and (industrial) robot motions that are important for understanding the domain of robot-based component testing.

2

Fundamentals of Robot-based Testing

This chapter is intended to provide the basics for further thesis descriptions. It introduces material and component testing, sensor systems, and (industrial) robot motions. The first section gives a brief introduction to material and component testing. The second section presents the commonly used sensor systems for material characterization. The last section concludes this chapter with an introduction to various types of motion in robotics.

2.1 Material and Component Testing

Material testing is a critical gateway to unlocking engineering, manufacturing, and construction progress. By subjecting materials to rigorous examination and analysis, to gain the confidence to design more robust, safer, and efficient structures and products. Whether it is ensuring the durability of sports equipment, bridges' resilience, or medical implants' performance, material testing provides the data and insights that drive advancements, enhance quality, and ultimately protect lives. Material testing is essential for qualitatively and quantitatively determining the properties of materials. This is a fundamental requirement for designing components in engineering, processing materials into finished products, quality assurance, and assessing instances of material damage. A **material** is defined as a substance that exhibits technically exploitable characteristics in at least one physical state, can be manufactured both technologically and economically, and is environmentally sustainable throughout and after its use. **Testing** involves the process of ascertaining whether a particular property exists within an object and, if

Material

Testing

Material Testing	
Scientific tests	Technological tests
Chemical tests	Physical tests
Destructive tests	Non-destructive tests
Static tests	Dynamic tests

Table 2.1. Structure of the subject areas of material testing. Each row is to be understood as a level for material testing, to which specific testing methods are assigned (adapted from [117]).

it does, determining the extent or value of that property. A material test involves a thorough examination of the specific material that is intended for use in fabricating a future workpiece. Within a material test, the material under scrutiny assesses its quality and response to various factors, including mechanical stresses, environmental conditions, and chemical exposures. Typical quality issues that material testing can reveal encompass variations in density, structural irregularities, the presence of voids, or the existence of hairline cracks. Conversely, a component test serves the purpose of evaluating a fabricated workpiece for its operational effectiveness. During these tests, components undergo examinations to assess their safety during use, their structural integrity or flexibility, as well as their durability and resistance to fatigue. Testing procedures can be categorized based on various criteria. An example is presented in Table 2.1, where each row is to be understood as a level for material testing to which specific testing methods are assigned. [16, 74, 117]

Material testing provides an unambiguous description by utilizing material characteristic values and thus makes materials comparable. The technological test methods are mainly used to determine characteristic values that depend on the specimen's shape. Their task is determining the suitability of primary products, especially semi-finished products, for further processing. In general a distinction is made between destructive and non-destructive material testing, depending on the effects of the testing procedures on the examined material. [16]

Destructive Component Testing

In destructive testing, also known as destructive physical analysis (DPA), tests are conducted until the specimen reaches failure. This approach is undertaken to gain insights into the specimen's performance or the material's behavior when subjected to varying loads. Destructive material testing typically involves mechanical testing methods, which are classified based on the type of load applied to the component. Destructive testing methods can be classified into mechanical, thermal, and chemical, as shown in Figure 2.1. Thermal testing involves subjecting materials or components to extreme temperatures, whether high, low, or cycling between them. Chemical testing delves into the molecular properties of materials. Typical techniques used in thermal and chemical testing include Metallography and Crystallography, among others. Materials and components to be tested are exposed to different mechanical loads. These can be further differentiated by the type of load acting on the component. This includes

tension, compression, torsion, bending, buckling, and shear. Different test procedures are carried out with the test specimen depending on the characteristic values to be determined. Typical mechanical testing methods include tensile tests, which determine tensile strength and other material properties, as well as shear tests. Mechanical testing methods are further distinguished based on their time sequence. In static methods, the test force is applied continuously and gradually increased until it reaches a maximum value. In contrast, dynamic tests subject materials to a sudden load. This is essential because certain materials can become brittle with an increased loading rate. Moreover, given that many components in practical applications experience periodic or cyclic loading, mechanical testing procedures can be classified as cyclic tests. As a result, the load undergoes periodic variations within the framework of these testing methods. Destructive testing of components is rarely automated, and there are few and very specialized test setups for it. More details on these so-called robot-based testing methods can be found in Section 4.4. [16, 117]

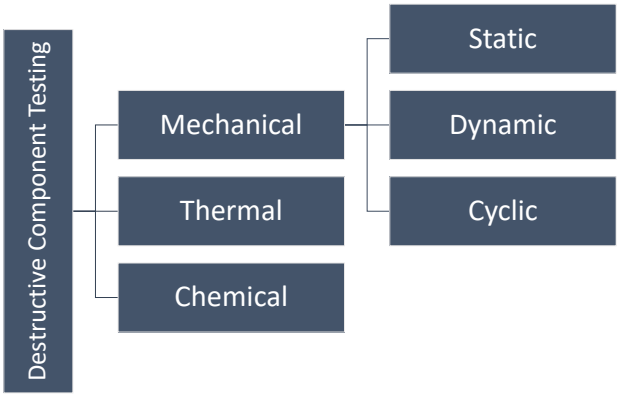

Figure 2.1. Classification of destructive testing methods (based on [117]).

Non-Destructive Component Testing

Safety-critical components, in particular, necessitate extensive testing efforts and, in certain instances, even 100% routine testing. When the test specimen incurs damage at the end of the material test and must be reprocessed for production, this becomes economically impractical, especially when dealing with large quantities. This challenge extends to complex components, such as the rotors of wind turbines. In such cases, manufacturing test components for testing purposes becomes prohibitively expensive. Consequently, non-destructive testing methods find application in these domains. These methods are primarily employed not to determine material properties but to detect defects on the workpiece's surface or within the material structure of the component. The significant advantage of non-destructive testing is that components remain undamaged

after the procedure, permitting their subsequent use. Figure 2.2 presents a potential categorization of non-destructive testing methods. [16]

Visual testing involves thoroughly inspecting the part using the naked eye or cameras. Ultrasonic testing is suitable for sound-conductive materials, allowing detection of external and internal defects in plastic components, cast parts, and welds. Radiographic testing employs gamma and X-rays to identify internal defects in plastics and metal materials, particularly ferromagnetic ones like steel, cobalt, nickel, and cast iron. Magnetic particle testing can find surface and subsurface defects in ferromagnetic materials. Eddy current procedures are used for electrically conductive materials, detecting even near-surface defects based on their permeability and electrical conductivity. Capillary testing involves applying a penetrant-like liquid, which seeps into every pore and defect due to capillary action. Automation, notably through robot-assisted testing, is gaining traction in non-destructive testing. More information on these robot-assisted testing methods is detailed in Section 4.4. [16]

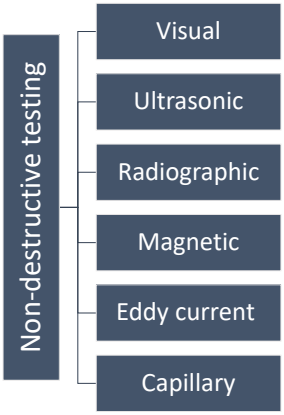

Figure 2.2. Classification of non-destructive testing methods (based on [16]).

Test Bench Technology

Following the exposition of classical material testing, an overview of test rig technology will be given. Components may encompass entire assemblies comprising multiple constituent parts or intricate individual entities. Various mechanical systems are available for performing component tests. Universal testing machines, in particular, stand as prevalent choices, highly suitable for conducting compression, tension, bending, and shear tests, rendering them adaptable for examining a broad spectrum of materials and components and will be explained in more detail in Section 3.1. Additionally, specialized testing apparatuses are meticulously engineered to cater to specific testing methodologies, e.g., for bike frames or automotive components. Systems constituted by one or more testing machines are conventionally termed test benches, primarily serving the

overarching objective of evaluating a given component's functionality and operational endurance. One way to distinguish different types of test benches from each other is to classify them according to their area of application. These are divided into two areas of application: product development and manufacturing. [109]

Development Test Benches

Durability Test Benches

Interim Test Benches

End-of-line Test Benches

In the realm of product development, there is a significant reliance on **development test benches**. These specialized testing setups are instrumental in evaluating the functionality of prototypes or newly designed components. Furthermore, **durability test benches** find application in both areas. In these contexts, components and products are subjected to real-world stresses until the material reaches its fatigue limit or the test specimen ceases to function. Within the domain of manufacturing, **interim test benches** are widely integrated. Positioned strategically between different production lines, these test benches meticulously inspect processed components before progressing to the next manufacturing stage. This setup allows for the early detection of any potential defects or issues. Towards the culmination of a production line, **end-of-line test benches** assume the role of assessing the final product's quality and functionality. They serve as the last checkpoint before the product reaches the end consumer. [109]

General Structure of Test Benches

Following a basic introduction to test benches, this paragraph will now delve into the software and hardware aspects of test benches. The software of test benches should also possess a modular structure to execute dynamically changing testing tasks automatically and efficiently. The required general architecture is depicted schematically in Figure 2.3 and comprises the following levels, organized from bottom to top [109]:

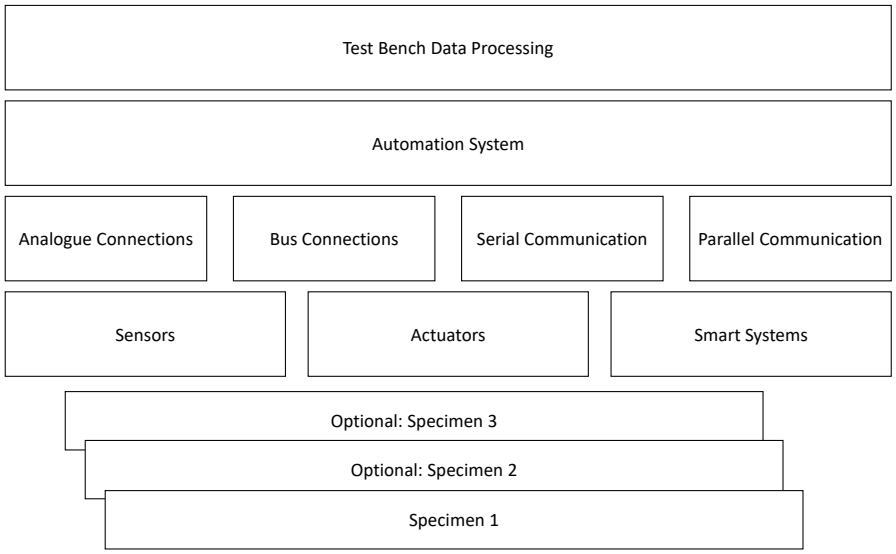

Figure 2.3. General structure of a test bench (adapted from [109]).

- The base always comprises the component or material under examination, referred to as the test specimen. In some test benches, multiple components can

be examined simultaneously. This is often the case when the samples have a simple geometric shape, are of small size, and a large number of tests need to be conducted.

- Physical Layer: Comprising sensors, actuators, conditioning systems, and intelligent components such as control units and advanced measurement systems.
- The intermediary layer linking the components of the physical layer to the automation system involves analog connections and bus connections.
- Automation layer: This level contains a wide variety of software, for example, for the execution of test motions or safeguarding the test bench by light barriers. Furthermore, it is responsible for adding different drivers, sensors, and actuators. This layer must also be modular in order to be able to perform rapidly changing test tasks automatically and efficiently.
- Test field data storage and data processing layer. The term test field refers to the test stand and other structures involved in the tests, such as logistical processes and data management systems. The aim is to ensure a uniform flow of information between all players within the test field.

2.2 Sensor Systems

As described above, different sensors are used in test benches to record the measurement results or to control the test itself. This section now briefly introduces the function of two types of sensors. First, the operating principle of torque sensors will be explained, and then the operating principle of stereoscopic cameras.

2.2.1 Force Torque Sensors

In the present time force torque sensors, the most prevalent method involves measuring the deflection when a force is applied to an elastic component. Occasionally, alternative methods are employed, such as balancing it against a magnetic force generated by the interaction between a current-carrying coil and a magnet or transducing the force into fluid pressure, followed by pressure measurement [43]. In many sensors, force is generated in response to a stimulus. However, this force is not directly converted into an electrical signal, necessitating additional steps. A typical force sensor combines a force-to-displacement transducer and a displacement sensor that converts the displacement into an electrical output. Typically, a force sensor incorporates an elastic element, such as a spring, polymer lattice, or silicon cantilever, along with a gauge, such as piezoresistive strain gauges, to measure the element's degree of compression or strain. This information is then converted into an electrical output signal. After conditioning, the sensing element typically produces low-level analog signals, which are converted into digital data using an analog-to-digital converter. Although various sensing technologies are available, the sensors primarily used in robots for force-torque sensing can be categorized into three main types: single-axis force sensors, single-axis torque sensors, and multi-axis force-torque sensors. The number of axes indicates how many spatial directions the sensor can measure. Single-axis force sensors provide information about

only one axis, while multi-axis force-torque sensors can simultaneously measure forces and torques in the entire three-dimensional space. Six-axis FT sensors are often equipped with strain gauges arranged to measure the forces and torques sensed at the sensor frame. Consequently, six-axis force-torque sensors provide comprehensive information about the sum of forces and torques exchanged between two objects, making them capable of directly conveying information about interactions with the environment. In a Cartesian coordinate system, as illustrated in Figure 2.4, there are three orthogonal forces (F_X, F_Y, F_Z) and their corresponding torques (T_X, T_Y, T_Z). These parameters define the entire six-dimensional space [48, 70].

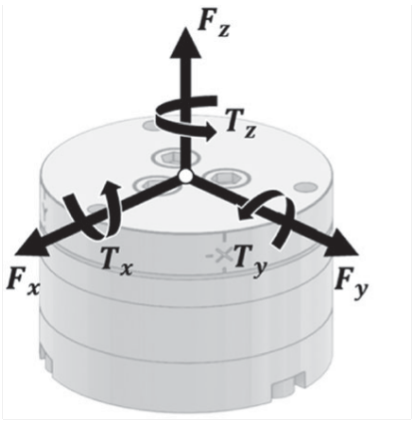

Figure 2.4. Schematics for a six-axis f/t-sensor showing the force and torque directions at a material point (adapted from [70]).

In robotics, single-axis torque sensors are commonly installed at the joints. These sensors play a pivotal role as they directly relate to the motors that actuate the joints, providing essential feedback for force-torque controllers. Due to their direct provision of this critical information, they find extensive use. On the other hand, multi-axis force-torque sensors are typically positioned between the robot's flange and the tool, where they detect the forces and torques acting on the tool. They are employed in various applications, including teleoperation and manipulation tasks like grinding drilling and delicate processes such as polishing. Moreover, they find utility in humanoid robots and surgical robots [70, 88]. Initially, integrating these sensors directly into the control system of a robot was challenging because the existing interfaces or robot motion control systems did not allow to influence the motion by measured force and torque. However, today, establishing this connection via interfaces, like the Robot Sensor Interface from KUKA, has become significantly more straightforward [82].

2.2.2 Stereoscopic Cameras

To calculate arbitrary 3D coordinates from a set of images, it is essential to satisfy one of two fundamental conditions. First, utilizing a single camera to capture at least two photos of an object from distinct, overlapping views. Alternatively, employing at least

two cameras, each capturing images of the same object from varying angles, overlapping their fields of view.

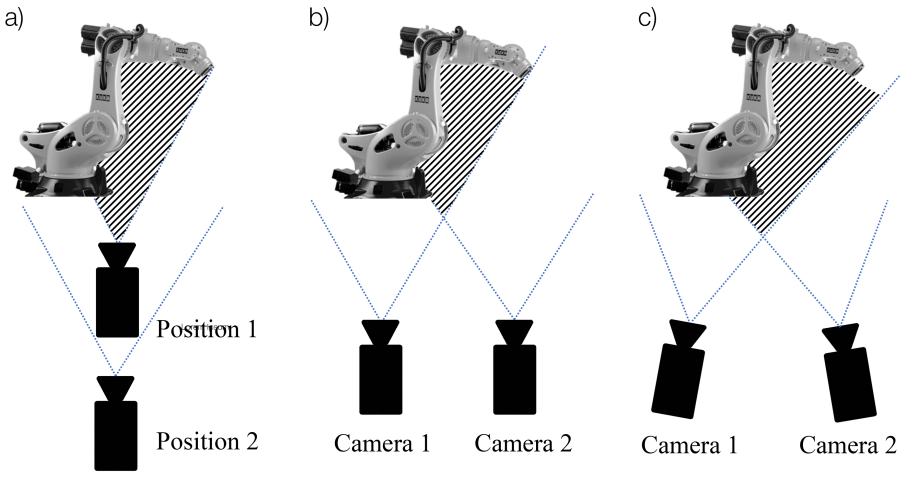

Figure 2.5. Schematic overview of possible arrangements for stereo camera measuring technology. A) shows the measuring principle with one camera and a position change. B) depicts the measurement with two parallel cameras, and c) shows the measurement with two convergent aligned cameras to increase the standard measurement volume.

Figure 2.5 schematically depicts these three potential configurations. Furthermore, it displays the setup involving two converging cameras, which enables an expansion of the shared image area in contrast to parallel cameras. Given that these cameras undergo a thorough calibration process, determining their internal parameters and relative positions, the converging arrangement does not necessitate any extra computational or setup complexity compared to the parallel setup. The third measurement principle (c) is employed in the subsequent sections to implement the robot's control.

These measurement methods acquire two images of an object from different positions or viewpoints. The subsequent step involves evaluating these measurement images. Based on these photographs, geometric principles rooted in central projection must be applied to image computation to determine the position and orientation of the robot Tool Center Point (TCP). In Figure 2.6, the principle of central projection in space is illustrated using the example of stereo vision with two cameras. The cameras should share the same focal length for practical application, with their X-axes intersecting and aligning along the baseline. Here, P represents the object point in the world coordinate system (X, Y, Z), U, V denotes the image coordinates for each camera, and b signifies the baseline. By combining these parameters with the focal length of the cameras, the coordinates of an object point can be determined using central projection for each camera (X, Y). It is important to note that for each image point P, an infinite number of object points can be associated with only one image. Therefore, as mentioned earlier, a second measurement

image of the same object point from a different perspective is essential to calculate the third coordinate, Z (depth). For precise derivations and mathematical relationships, further references are available in the literature [72, 93].

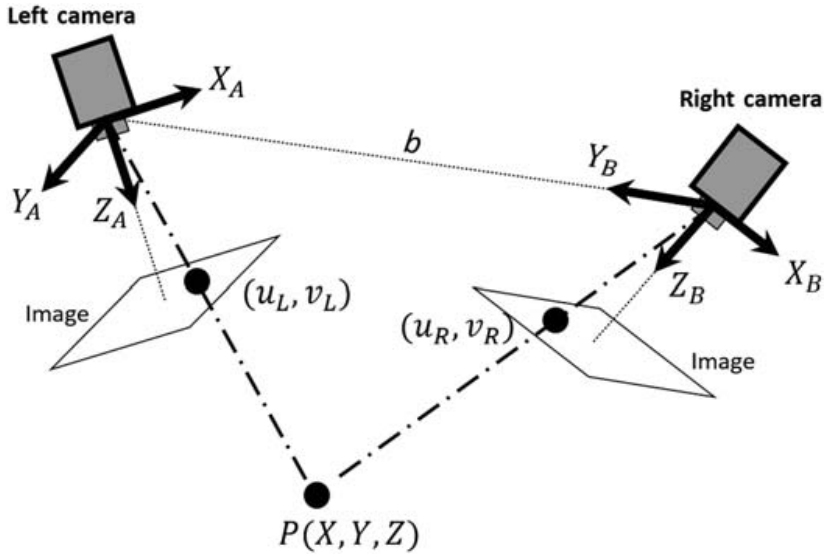

Figure 2.6. Principle of central projection in space using the example of stereo vision with two cameras (adapted from [53]).

In photogrammetry, a clear distinction is made between inner and outer orientation. The inner orientation encompasses all camera-internal parameters, including the camera constant and the image's principal point coordinates. These parameters are crucial for establishing a reference between the projection center and the image plane. On the other hand, the outer orientation defines the camera's position and orientation in space, allowing for the description of how the object point is projected relative to the world coordinate system. Typically, the manufacturer measures or calibrates the parameters of the inner orientation. However, determining the camera's position and orientation is an additional step. This can be achieved by incorporating fixed points into the image or equipping the robot with markers and moving it within its known coordinate system. This movement helps establish the transformation relative to camera coordinate system. Unique measurement markers are essential to consistently determine fixed 3D coordinates within the measurement volume of a stereo camera array (as seen in Chapter 9). These markers are characterized by retroreflective point features that remain recognizable by the cameras even in challenging backlight conditions. Ellipses are fitted around the circular markers during subsequent image analysis to account for potential skewing of the measurement marks. This approach enables the precise determination of the centers of the measurement marks [72, 93].

To directly derive pose information from image measurements captured by both cameras, a minimum of three coded marks within the camera's field of view is required. Ideally, these marks should form a triangle. When the user specifies which markers should

be used for pose calculation in the software, the camera controller can provide this information directly. When applied to a robot's end-effector, the end-effector should be equipped with measurement marks. To ensure maximum flexibility, placing several coded marks at various locations on the end-effector is advisable. This allows the robot to function effectively in diverse working positions, forming the foundation for the 6D pose control described in Section 8.4 [44].

2.3 Robots and Robot Motions

Industrial Robot

According to the ISO 8373:2021(en) [9] norm, an **industrial robot** and its components are defined as follows:

> *"An automatically controlled, reprogrammable, multipurpose manipulator, programmable in three or more axes, which can be either fixed in place or mobile for use in industrial automation applications". It consists of "the manipulator, including robot actuators controlled by the robot controller and the means by which to teach and/or program the robot, including any communications interface (hardware and software)"* [9, Section 3.6].

Contrary to Siciliano et al.'s definition [120], this standard introduces a distinct definition for industrial robots, distinguishing between the robot's manipulator and its controller. In this context, the term "controller" predominantly refers to the reprogrammable software component of the physical controller. The manipulator is a machine composed of a series of segments, typically interconnected by revolute and prismatic joints. Its primary function is to grasp and manipulate objects, such as workpieces or tools, often with multiple degrees of freedom [9, Section 4.14]. Industrial robots come in various configurations, differing in the nature and number of joints, directly affecting their ability to interact with the environment. To manipulate objects effectively in a 3D space, a manipulator requires a minimum of six degrees of freedom (DOF) distributed along its mechanical structure [120, p. 4]. The manipulator is usually anchored to the ground or ceiling via its base and is equipped with a mounting flange used to attach end-effectors, such as a gripper, responsible for handling workpieces. For this thesis, "robot" or "manipulator" refers specifically to an articulated arm featuring six revolute joints unless explicitly specified otherwise.

Position and Orientation

The robot controller encompasses a programmable motion controller responsible for planning and executing the manipulator's movements. This often involves using an industrial computer equipped with specialized software. The **position and orientation** of an end-effector can be entirely defined by its relationship to a reference coordinate system. A world coordinate system serves as a global reference for many applications, and each robot's position and orientation within a work cell are defined with respect to this world coordinate system. Additionally, each robot has its robot-base coordinate system, which defines its position and orientation by describing the translation and rotation relative to the world coordinate system. The Tool CenterPoint (TCP) is a further reference point for industrial robots. It signifies the point where the chosen end-effector operates. The TCP typically resides within the flange coordinate system on the sixth rotary axis when no end-effector is employed. If the tool's orientation is also specified,

it defines the TCP coordinate system. Measuring the positional relationship of the tool concerning the flange coordinate system is a crucial step for utilizing the tool in path generation within robot control. According to [120, p. 39-40], a vector is employed to define the position of a coordinate system O' concerning a reference coordinate system O. In the context of a three-dimensional cartesian coordinate system, a vector $\vec{o} \in \mathbb{R}^3$ composed of x, y, and z components is used to express the position of the coordinate system O' concerning the reference coordinate system O as $\vec{O'} = \vec{O} + x * \vec{e_x} + y * \vec{e_y} + z * \vec{e_z}$, where $\vec{e_x}$, $\vec{e_y}$, and $\vec{e_z}$ represent the unit vectors of the coordinate system O. These unit vectors can be combined into a single rotation matrix in coordinate system transformations. Using homogeneous coordinates, it becomes possible to describe the entire transformation from O to O' using a single transformation matrix. In robotics, however, instead of employing transformation matrices, it is more common to describe the orientation of a coordinate system using **Euler angles**. These angles characterize three successive rotations around the axes of a coordinate system. The order in which these rotations are applied can lead to different outcomes, necessitating the adoption of a standardized convention. [120, p. 52-56]

Euler Angles

For this work, the same convention as KUKA uses is utilized, often referred to in literature [120, p. 51] as Roll-Pitch-Yaw (RPY) angles, and defined as follows :

- Angle C defines the rotation around x-axis of the reference coordinate system.
- Angle B defines the rotation around y-axis of the reference coordinate system.
- Angle A defines the rotation around z-axis of the reference coordinate system.

There are two ways to determine the rotation sequence. Current frame rotations, which involve applying rotations to an object's local coordinate system, one after the other. The order of these rotations matters and determines the final orientation. Current frame rotation conventions include Euler angles. Fixed frames rotations involve applying rotations to an object's global coordinate system, one after the other. The order of these rotations also matters and determines the final orientation. In fixed frame rotations, the object's local coordinate system remains fixed. For instance, KUKA employs the fixed frame rotation sequence $X - Y - Z$. This sequence can be equivalently expressed using current frame rotations as follows: Z, Y', X''. The concept here is that, following a rotation around the z-axis, the subsequent rotation occurs around the newly established y-axis, and this pattern continues for the x-axis. This implies that the robot can also be moved within different coordinate systems, like the end-effector coordinate system or a camera's coordinate system. In such cases, only the translation and rotation must be converted into the robot's coordinate system. [120, p. 40-57]

The ability to reposition the robot's attached end-effector at the flange to various positions is a fundamental necessity in most robotic applications. When the robot shifts from one position to another, it necessitates planning a specific **trajectory** to perform this motion. This is crucial because, due to the innate inertia of physical objects, the robot cannot simply move at a constant speed. Instead, it must undergo phases of acceleration and deceleration before coming to a stop. Employing six axes provides the capability to approach identical target poses within the workspace using various axis configurations. This offers flexibility for collision avoidance and optimal path planning. However, it also

Trajectory

presents an issue when calculating the inverse kinematics and determining individual axis angles from a given pose, which can become over-determined. The arrangement of axes can result in singularities, where a slight change in position in space would cause one axis to rotate completely. Such situations typically arise when two rotation axes are identically oriented along a trajectory. Nonetheless, singularities can be avoided with an additional axis and careful path planning. Furthermore, the forces and moments cannot be determined correctly in such a pose. Notably, industrial robot control units often offer limited predefined motion types. For instance, KUKA's KRL (KUKA Robot Language) provides three primary movement types: Point-To-Point (PTP), Linear (LIN), and Circular (CIRC) motions. PTP motions are typically utilized when rapid repositioning of the robot is needed, and the specific path taken by the end-effector is of minimal importance. In LIN motions, the trajectory constitutes a straight-line path connecting the starting and target positions. Linear motions are preferred when the path traced by the end-effector holds significance in the application, e.g., in gluing operations. [120]

Some motion controls offer interfaces for external motion control, meaning that the desired trajectory is not planned and executed by the manufacturer-supplied hardware and software but rather by a system provided by the customer. External control can occur at various levels for electrical drives, including industrial robots. The external system can directly control the power applied to the drive or supply a desired velocity for the drives. Another possibility is providing the desired position or correction by the external motion controller.

Position Control

Within the scope of this study, particular emphasis is placed on **position control** and position correction. The external motion controller must provide new position points or corrections within defined time intervals in cyclic position control. The hardware device then endeavors to reach the specified position within a single interval. Therefore, it is essential that the points are reachable within this interval, and the trajectory's velocity must remain consistent. Otherwise, due to the system's inertia, the hardware device may struggle to follow the trajectory. Position correction can be executed with the aid of a sensor and can be termed **sensor-guided motion**. There are two prevalent strategies for interaction control in sensor-guided motions. The first is the force-controlled approach, which allows for the regulation of contact forces to a desired level, often involving the closure of a force-feedback loop [120, p. 364]. The second approach is visual control, where visual measurements are used as feedback in the control system to correct the positional error of the robot's end-effector [120, p. 408]. KUKA, for instance, offers two possibilities to implement force-based sensor-guided motions. First, the robot does not move to a preprogrammed endpoint during a sensor-guided motion. Instead, it commences movement from a starting point based on the measured sensor data and continues until a predefined stopping condition is met. An example of the first scenario, where a force-torque sensor guides the motion, is illustrated in Figure 2.7a. In this case, the robot moves along the Z-axis in the tool coordinate system until it attains the specified force set point. The second option involves the robot following a programmed path while simultaneously exerting defined force and torque set-points. Figure 2.7b exemplifies this scenario, where the robot moves along a predefined path in the XY plane within the base coordinate system. Additionally, it maintains a specified force set-point

Sensor-guided Motion

in the z-direction along the programmed path. Furthermore, it is worth noting that this correction can also be executed using other sensor systems, such as stereoscopic cameras.

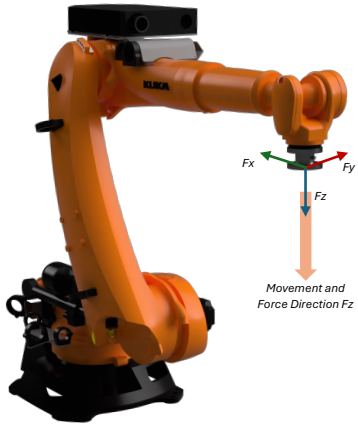

(a) Example of a force torque sensor-guided motion control. The robot moves in the z-direction in its tool coordinate system until a defined force set-point is reached.

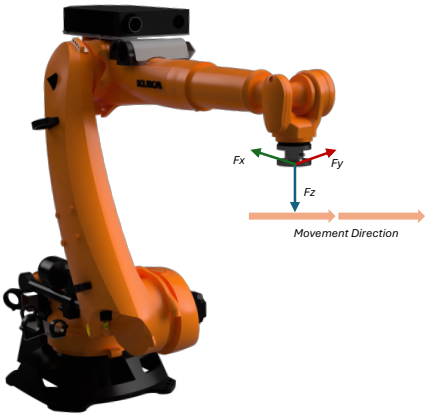

(b) Example of superimposed f/t-control. The robot executes a programmed path in the plane. Additionally, the robot exerts a defined force in the z-direction along the programmed path.

Figure 2.7. Two examples of force torque controlled sensor-guided motions performed by a KUKA robot (according to [81]).

Summary. The approach presented in this thesis is evaluated based on four case studies for its technical feasibility and the benefits of software-defined test benches. All four case studies, their domains, and related work are described in this chapter. In order to address general problems and challenges of component testing, the approach is applied to a classical tensile specimen and three different components. These three different components, the bicycle frame, the snowboard, and the automotive component, each have their additional testing requirements.

3 Case Studies

The advent of Industry 4.0 is revolutionizing production processes, aiming to produce customized products in small quantities without compromising quality. As production shifts towards unique dimensions and structures for each product, the testing of components must also be adaptable to these variations. Additionally, the increasing complexity of components, including those produced through additive manufacturing, poses challenges in designing suitable test setups.[87] Given the wide variety of components, developing expensive test benches for each component is not cost-effective. Nonetheless, ensuring the quality of every component remains crucial. Therefore, a flexible test bench is required to test various types of components.

The hardware and software concepts for a robot-based testing facility presented in this work allow destructive component tests for diverse components. In order to evaluate the added value and transferability of this approach to different components, four case studies with different testing characteristics are considered. Each case study presents

unique and component-specific challenges, which are addressed within the framework of the general approach. The first case study is a tensile test, representing a classical use case for the early determination of specific properties of material components. The following section (3.2) describes a case study in which a bicycle frame is tested at different loading points, followed by the third case study in Section 3.3 for the evaluation of complex testing motion on a snowboard. Subsequently, Section 3.4 presents the test of an automotive component to explain why multiple test motions are needed simultaneously.

3.1 Case Study 1: Tensile Test

As described in Section 2.1, material testing encompasses various testing methods used to assess the behavior and properties of standardized material samples (material analysis) or finished components (component testing) under mechanical, thermal, or chemical stress. It involves evaluating the material's purity, absence of defects, or load-bearing capacity, among other factors. The goal is to determine how a material performs and is appropriate for specific applications through mechanical, thermal, or chemical testing examinations. Within destructive mechanical material testing, tensile tests are used to determine material characteristics such as ultimate tensile strength, breaking strength, maximum elongation, and reduction in area. [34] Tensile tests are one of the most frequently performed tests in mechanical material testing and thus offer a reasonable basis for an initial comparison between a classic testing machine and a robot-based test bench.

3.1.1 Fundamentals and State of the Art

Uniaxial quasi-static tensile testing is a fundamental testing method and is the most commonly used one in materials science and engineering for obtaining the mechanical characteristics of materials. It involves applying controlled tensile forces (monotonous increase) to a specimen until it reaches failure. Some purposes of tensile testing are, e.g., to select a material or item for an application or provide standard data for other engineering, scientific, and quality assurance functions. [34] A **tensile test specimen** typically has a standardized shape and dimensions to ensure consistent testing conditions and facilitate comparison of results. The structure of a typical tensile test specimen is schematically shown in the upper part (a) of Figure 3.1. The gauge length is the central region of the specimen where the deformation and elongation are measured during the test. The reduced section, also known as the neck or waist, is between the grip sections and the gauge length. It has a smaller cross-sectional area than the gauge length and is where the specimen undergoes localized deformation prior to fracture. The grip sections are located on either end of the specimen and are securely held in the testing machine. These sections often have serrated surfaces or specialized grip designs to prevent slippage during the test.The choice of **grip type** depends on the material and the specific requirements of the test. The lower part (b) in Figure 5.1 illustrates the commonly used options regarding shoulder types for gripping systems. The specimen can be affixed to a threaded grip by screwing it in (depicted on the left)

Specimen Shape

Grip Type

or can be secured with a pin (depicted on the right side). Alternatively, butt ends, or wedges may be employed to hold the grip section. When selecting a gripping method, the primary consideration is to guarantee that the specimen remains securely held at the maximum load, avoiding slippage or failure in the grip section. Furthermore, it is crucial to minimize bending effects.

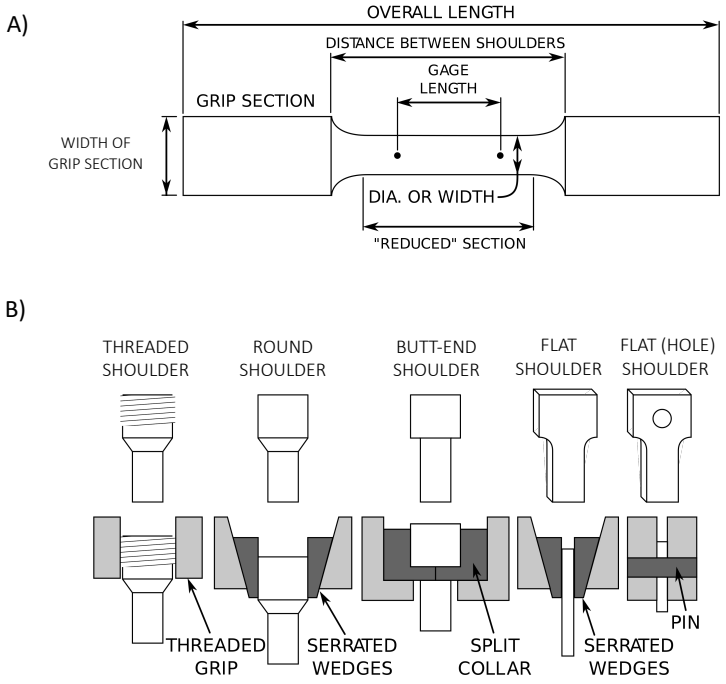

Figure 3.1. Schematic representation of the nomenclature of a generic specimen shape (a) and the various grip types and shoulder geometries (b) (based on [34]).

Universal Tensile Testing Machine

Tensile testing is often carried out at a material testing laboratory. The predominant testing machines utilized are **universal tensile testers**, which subject materials to tension, compression, or bending. The term "universal" in the name indicates its versatility in conducting various standard tensile and compression tests on materials. Their primary objective is to generate the stress-strain curve detailed in the subsequent part of this section. Testing machines are classified as electromechanical or hydraulic, with the key distinction in the load application method. Figure 3.2 shows a schematic setup of a universal testing machine reflecting the bone-shaped specimen gripped between the base and the moving crosshead with a wedge clamping jaw. Electromechanical machines operate using a variable-speed electric motor, one to four screws to control the upward or downward movement of the crosshead, thereby applying tension or compression to the specimen and a a gear reduction system. Hydraulic testing machines use a single or dual-acting piston that moves the crosshead. The velocity of the crosshead, along with the corresponding load rate, can be regulated by a microprocessor within a closed-loop controller. The strain can be recorded either through the traverse path of the machine

or by using additional sensors such as extensometers or optical systems. Determining the specimen's strain based on the traverse path is distorted by the deformation of the machine under load and mechanical play in the force transmission to the specimen. Extensometers or optical systems circumvent this issue by measuring strain directly on the specimen outside the force flow. The occurring forces are usually measured with built-in force sensors. The test **process** is detailed in a test method, often published by a standards organization. This specifies the sample preparation, fixturing, gauge length (the length under observation), and velocity ranges depending on the materials to be tested. [34]

Process

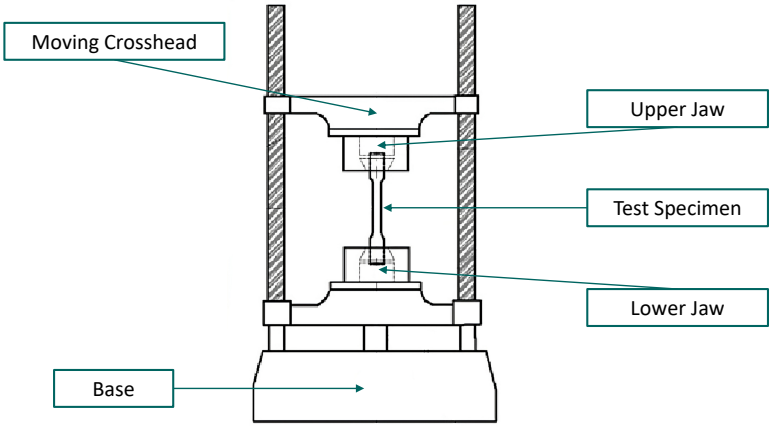

Figure 3.2. Schematic diagram of a universal tensile testing machine consisting of a clamped dog bone shaped specimen between the moving crosshead and the base (adapted from [31]).

In summary, a tensile testing machine stretches a standardized specimen with a defined cross-sectional area to failure, increasing the strain or displacement uniformly, without shock, and at a low rate. The primary use case of these processes is to facilitate direct comparison between different materials in a standardized manner and independent of the material's size. This can be achieved by analyzing and comparing the engineering stress-strain response, e.g., with a **stress-strain diagram**. For this purpose, the elongation of the gauge section is first recorded against the applied force on the specimen during the test. The force measurement is used to calculate the engineering **stress**, σ , using the following equation [38]:

Stress-Strain Diagram

Stress

$$\sigma = \frac{F_n}{A} \tag{3.1}$$

where F is the tensile force and A is the initial cross-section of the gauge section. The elongation measurement is used to calculate the engineering **strain** ε, using the following equation [38]:

Strain

$$\varepsilon = \frac{\Delta L}{L_0} = \frac{L - L_0}{L_0} \tag{3.2}$$

where ΔL is the change in gauge length, L_0 is the initial gauge length, and L is the final length. An idealized stress-strain curve of a polymer film is shown in Figure 3.3. Conventionally, the strain is represented on the horizontal axis, while the stress is depicted on the vertical axis. There are several **stages/regions** showing different behaviors, which suggests different mechanical properties. It should be noted that materials can miss one or more stages or have different stages. The first stage (A-B) is the linear elastic region, where the stress and strain exhibit a proportional relationship following Hooke's law, with the slope representing Young's modulus. During this phase, the material experiences solely elastic deformation. The transition point from this stage marks the onset of plastic deformation. The stress value at this point is referred to as the yield strength or **yield point** (B). Certain materials, like low-carbon steels, demonstrate stress-strain curves characterized by initial peaks followed by reduced stresses.. After the initial peak (upper yield point), deformation predominantly occurs within a localized specimen region, resulting in a relatively small area undergoing continued elongation (lower yield point). After the entire gauge section has been traversed in this region, the stress does rise again, and the subsequent phase, known as the strain hardening region, begins (B-C). It extends to the point of ultimate strength, the ultimate tensile strength (C). Throughout this region, the stress primarily increases in tandem with the elongation of the material, although certain materials like steel may exhibit a relatively flat portion at the initial stage. Work strengthening becomes more pronounced as strain accumulates until the stress reaches the ultimate tensile strength. The last phase (C-D) is referred to as the necking region. Once the material surpasses the tensile strength, localized deformation occurs in necking, where the cross-sectional area becomes significantly smaller than the average. This necking deformation is non-uniform and reinforces itself as stress concentrates more in the reduced section. This positive feedback mechanism leads to rapid necking development, resulting in fracture. It is important to note that even though the applied force decreases, work strengthening continues to progress. This means that the true stress increases while the engineering stress decreases due to the unaccounted shrinking section area. The necking region culminates in fracture (D), after which parameters such as percent elongation and reduction in section area can be calculated. [38]

Stages / Regions

Yield Points

Stress-strain curves reveal many of the properties of a material, such as Young's modulus, tensile strength, and elongation at break. The **Young's modulus** (Y-Modulus), also known as the modulus of elasticity in tension or compression, is a mechanical characteristic that assesses the stiffness of a solid material when subjected to lengthwise forces, either in tension or compression. It quantifies the correlation between the applied stress σ in tension or compression and the resulting strain ε:

Young's modulus

$$E = \frac{\sigma}{\varepsilon} \tag{3.3}$$

Young's moduli are generally of such magnitude that they are expressed in gigapascal (GPa).

Tensile strength R_{m} (also known as tear strength) is one of several strength characteristics of a material. It is the maximum mechanical tensile stress that the material can withstand. In the stress-strain diagram (see Figure 3.3), tensile strength corresponds

Tensile Strength

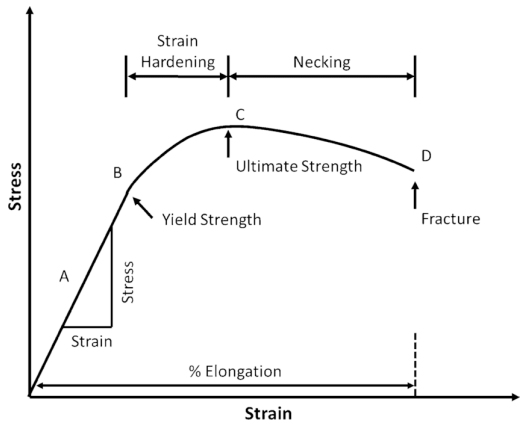

Figure 3.3. A typical stress–strain curve for a polymer undergoing a standard tensile strain testing [91].

to the highest point on the curve (C). It is typically determined through a tensile test, where the maximum applied tensile force (F_z) is divided by the test specimen's original cross-sectional area (A_0).

$$R_{\mathrm{m}} = \frac{F_z}{A_0} \tag{3.4}$$

The unit of tensile strength is force per unit area, measured in N/mm² or MPa.

Elongation at Break

Elongation at break is another common characteristics of a material. It defines the ratio between the changed length and the initial length after the breakage of the test specimen. It represents a material's ability to withstand deformation without developing cracks. A is the elongation ΔL of a specimen in a tensile test after fracture, related to the initial gauge length L_0:

$$A = \frac{\Delta L}{L_0} * 100\% \tag{3.5}$$

The unit of Elongation at break is a percentage.

Based on these stress-strain curves, materials can be categorized into two main groups: ductile and brittle. These groups exhibit distinct characteristics that allow for differentiation.

Ductile Materials

Ductile materials such as structural steel and various metals can undergo yielding at average temperatures. For instance, low-carbon steel typically demonstrates a stress-strain relationship that is highly linear until reaching a clearly defined yield point. The linear segment of the curve corresponds to the elastic region, with the slope representing the modulus of elasticity or Young's modulus. Plastic deformation continues at the upper yield point until the lower yield point is reached.

Brittle Materials

Materials with **brittle** behavior, such as cast iron, glass, and stone, exhibit fracture without significant elongation rate changes or yielding prior to failure. In the case of

brittle materials like concrete or carbon fiber, there is no distinct yield point or strain hardening. As a result, the ultimate strength and breaking strength are identical. Unlike ductile materials, brittle materials do not undergo plastic deformation and fail within the elastic range. The stress-strain curve for brittle materials typically follows a linear pattern.

3.1.2 Scenario Definition

Classical tensile tests are now considered the first case study to determine whether robot-based component testing is fundamentally suitable for material testing. In order to test a wide stress-strain range, three different materials for the tensile specimen were chosen, which represent the components: Steel (St 12), aluminum (1050-H16), and polypropylene (PPH).

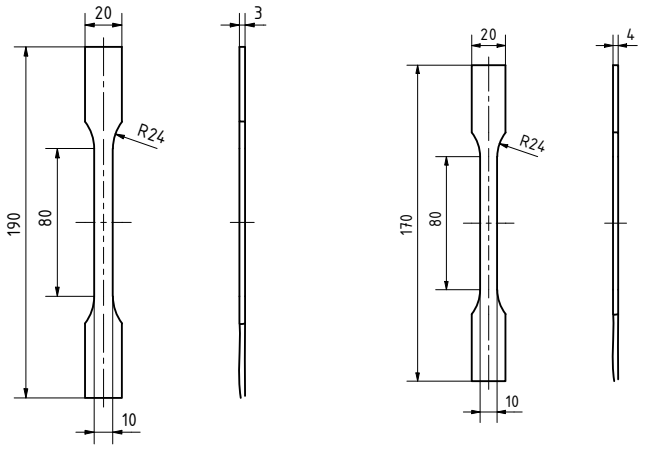

Figure 3.4. Specimen shape and dimensions in mm of the three chosen materials. Steel and Aluminium on the left side are identical and Polypropylene on the right side is smaller and thicker.

Classical specimens were chosen with flat shoulders for serrated grips. The Steel and Aluminium specimen have identical dimensions: $190\,\mathrm{mm}$ overall length, $20\,\mathrm{mm}$ width of the grip section, a gauge length of $80\,\mathrm{mm}$, a transition radius of $24\,\mathrm{mm}$ and a thickness of $3\,\mathrm{mm}$. The polypropylene specimen is smaller with $170\,\mathrm{mm}$ overall length, thicker with $4\,\mathrm{mm}$ thickness, and identical in the remaining dimensions. Based on the standards testing methods for the three chosen materials [6, 7], the following velocities were selected, and ultimate strength were expected:

The same tensile tests will be performed once on a classic testing machine and a robot-based test bench. In order to be able to carry out these tests, a suitable fixture and the appropriate end effector for the robot-based test bench must first be designed. The robot-based test bench also needs to be capable of achieving pulling forces up to $19\,500\,\mathrm{N}$ with

Material	Ultimate Strength	Testing Velocities
Steel	19 500 N	$1\,\mathrm{mm\,min^{-1}}$ until Y-Modulus at 200 N, continuing with $10\,\mathrm{mm\,min^{-1}}$
Aluminium	7700 N	$5\,\mathrm{mm\,min^{-1}}$
Polypropylene	750 N	$5\,\mathrm{mm\,min^{-1}}$ until Y-Modulus at 6000 N, continuing with $50\,\mathrm{mm\,min^{-1}}$

Table 3.1. Load case overview with corresponding forces and velocities for each specimen.

velocities between $1\,\mathrm{mm\,min^{-1}}$ and $50\,\mathrm{mm\,min^{-1}}$. Furthermore, the forces during the test sequence as well as the elongation of the specimen, need to be measured to evaluate the strain samples afterward, with a stress-strain diagram.

3.2 Case Study 2: Bike frame

During cycling, high loads can lead to excessive stress on the bicycle frame, potentially causing cracks that eventually result in structural failure. Even small loads can initiate microcracks in metallic materials, propagating into visible macroscopic cracks under continuous cyclic loading until the load-bearing structure fails. In brittle materials like carbon fiber composites (CFK), even a single overload event can cause catastrophic fractures. These damages are often caused by design, manufacturing, or material flaws. As explained in Section 2.1, material testing involves a range of techniques to evaluate the performance and characteristics of components, e.g., bicycle frames, when subjected to mechanical, thermal, or chemical stress. To prevent accidents, destructive mechanical testing procedures and test benches have been developed to assess bicycle structures at the component level and conduct overall structural tests. Testing a bicycle frame is suitable as a case study for robot-based component testing for two main reasons. First, as described in Section 3.2.2, most test benches are specifically designed for, e.g., bicycles and, therefore, are dedicated to the type of component that must be tested. Second, these test benches only map a few exceptional load cases. It is only possible to test one part of a bicycle frame on a test stand without rebuilding it or manufacturing a second one to test other parts of the bicycle frame. A flexible robot-based test bench can provide a remedy here. Robots have a much larger workspace and can flexibly test motions in almost all directions and orientations. How flexible a robot can implement different testing motions with different positions and orientations is to be investigated based on this case study. Furthermore, the concepts for planning and execution of these motions can be evaluated, and the requirements resulting from the tensile tests can also be extended.

3.2.1 Fundamentals

Before the basic test methodology and the related work are explained in detail, the critical technical terms relating to bicycles will be defined using Figure 3.5. A bicycle

frame is a primary structure onto which various components and wheels are attached. The prevalent design for upright bicycles is a diamond frame consisting of a central and rear triangle (see Figure 3.5). In addition to the widely recognized diamond frame, numerous alternative **frame designs** have been developed for bicycles, several of them remain popular and widely used in the present day. There are, for example, step-through or tandem frames. The former is often used for utility bicycles, with a low or absent top tube, whereas the second-mentioned are designed to allow multiple riders simultaneously on one bike. Fundamentally a (diamond) frame consists of two **frame parts**: The main frame and the rear triangle. The former is composed of the head tube, top tube, down tube, and seat tube. The rear triangle is composed of the seat tube along with the paired chain stays and seat stays.. The top tube connects the head tube to the top of the seat tube. In a diamond frame, the top tube is horizontal (parallel to the ground). The fork is attached to the head tube, with the steerer tube inside the head tube and the two fork sheaths. The down tube connects the head tube to the bottom bracket shell. The bottom bracket shell runs side to side and holds the bottom bracket. The seat tube contains the bike's seat post, which connects to the saddle. The chain stays are parallel and connect the bottom bracket shell to the rear fork ends or so-called dropouts. [123]

Frame Design

Frame Parts

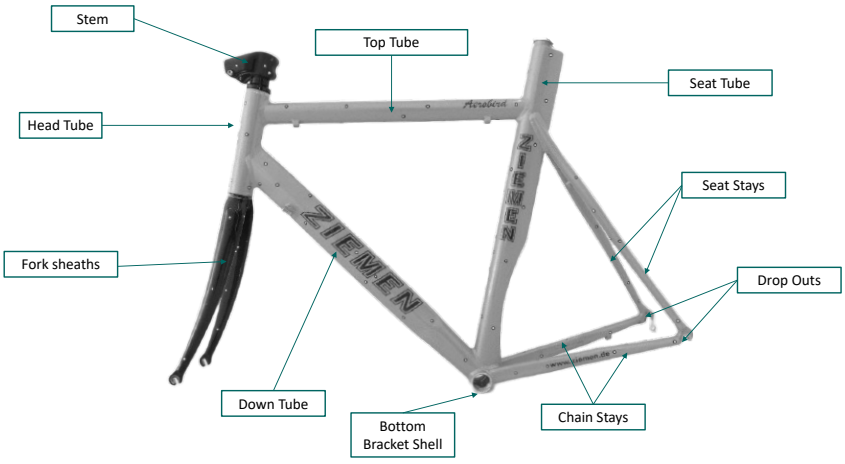

Figure 3.5. Basic nomenclature of a bicycle frame.

Strength, stiffness, and lightweight or other frame attributes can be achieved through the strategic selection of a frame design but also through the use of different **frame materials** or through the combination of both. The different material characteristics of the respective materials must be considered for achieving particular frame attributes. These include density, stiffness, yield strength elongation, and fatigue limit. Density quantifies the mass of a material relative to its volume, indicating its relative lightness or heaviness. A material's stiffness can impact both the comfort of the ride and the efficiency of power transmission. A material's yield strength determines the force required to cause

Frame Materials

permanent deformation, and elongation determines how much deformity the material allows. This is, e.g., relevant for crashworthiness. The fatigue limit of a frame determines its durability when exposed to cyclic stress from pedaling or encountering ride bumps. Throughout history, steel has been the prevailing material choice for bicycle frames. Steel frames can be constructed from various steel grades, from affordable carbon steel to pricier and superior chromium molybdenum steel alloys. Steel is known for its strength, ease of fabrication, and cost-effectiveness. However, it is characterized by a higher density than other structural materials, typically resulting in higher weight. Aluminum alloys have a lower density and lower strength than steel alloys. However, their strength-to-weight ratio is superior, making them advantageous in terms of weight reduction compared to steel. Titanium offers high specific strength and a high fatigue limit. However, titanium frames come with a higher material cost and are more challenging to process compared to steel or aluminum. Carbon fiber composites are renowned for their lightweight and high-strength properties. One of the significant advantages of carbon fiber is its ability to be molded into virtually any desired shape, allowing for optimal customization. This means the frame can be engineered to provide specific strength in areas where it needs to withstand the forces generated during pedaling while allowing for flexibility in other sections to enhance overall comfort. However, it is essential to note that while carbon frames excel in weight and strength, they may have lower impact resistance than frames made from alternative materials mentioned before. Combining different materials makes it possible to achieve the desired levels of stiffness, compliance, and damping in specific areas more effectively than with a single material. This approach often involves using carbon fiber with a metal, such as steel, aluminum, or titanium. [42, 73, 123] An example of this approach is a variation that involves a metal main triangle and chain stays paired with carbon seat stays. Carbon forks have become increasingly prevalent in racing bicycles, regardless of the frame material used.

3.2.2 State of the Art

Standardization

Various methods and test rigs exist in both research and industry for material testing of bicycle frames or bicycle components. As a basis for obtaining bicycle safety, many international **standards** were developed. The most common standard is the ISO 4210 standard [5], which specifies terms and definitions related to safety and performance requirements for the design, assembly, and testing of bicycles and sub-assemblies. It delineates a procedure for assessing the fatigue strength of components. Its testing criteria are based on three fundamental factors: fatigue (induced by cyclic loads), overloading, and impacts. Figure 3.6 shows the schematics for two frame testing examples, a drop-mass impact test on the left and a drop-frame impact test on the right. The drop-mass impact test (a) involves replacing the bicycle frame fork with a solid-steel bar inserted into the head tube. A striker is positioned vertically above the solid-steel bar, with a distance of $212\,\mathrm{mm}$ between them. The striker is released to fall downhill and impact the solid-steel bar freely. The resulting permanent deformation of the fork along the longitudinal direction of the frame can be measured and recorded as the striker stops on the solid-steel bar. During a drop-frame impact test (b), a $70\,\mathrm{kg}$ mass is securely

positioned on top of the seat tube of the bicycle frame. The entire system, including the mass, is vertically aligned above the rear axle. The bicycle frame system is rotated freely around the rear axle, allowing it to drop downhill and make contact with a steel anvil. The resulting permanent deformation along the longitudinal direction of the frame can be measured and recorded when the front fork stops on the steel anvil. [5, 32]).

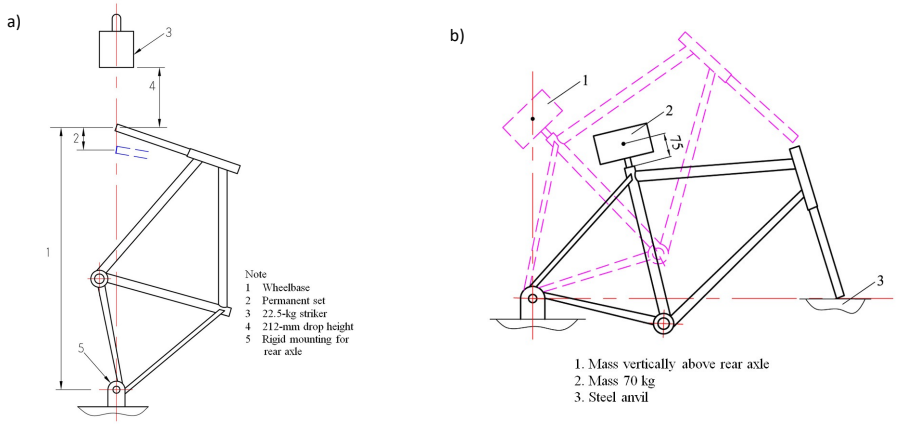

Figure 3.6. Schematic diagram of a drop-mass impact test on the left and a drop-frame impact test on the right (adapted from [32]).

Additional global standards address specifications for various bicycle components such as stems or spokes. Similar standards are also applicable in the United States, such as ASTM F2711 [4], which outlines test procedures for bicycle frames, and ASTM F2273 [3], which defines safety tests specifically for bicycle front forks. However, these standards do not include all the necessary test methods, e.g., no standardization is available for the stiffness performance of a bicycle frame [129]. Therefore, further methods have been developed both in research and in industry.

Test Simulation

Several research topics focus for example on **simulating** different tests of bicycle frames [23, 59, 132]. In 1986, Peterson and Londry conducted a study utilizing Finite Element Analysis (FEA) to optimize the design of the Trek 2000 aluminum frame [35]. In the Finite Element Analysis (FEA), products and systems are modeled within a virtual environment to identify and resolve potential (or existing) structural or performance issues. It allows for analyzing complex geometries and varying material properties, providing valuable insights into the system's behavior under different conditions. [122] Peterson and Londry compared it to two other existing designs, one made of steel and one made of aluminum, to evaluate its mass, strength, and stiffness characteristics. This research played a crucial role in establishing the foundation for utilizing FEA as a valuable tool in supporting bicycle frame design, development, and testing. Covill et al., e.g., used a model which simulates two standard loading conditions to understand the vertical compliance and lateral stiffness characteristics of 82 existing bicycle frames. [35] Cheng et al. [32] researched an integrated optimization procedure to reduce the bicycle frame's weight and the permanent deformations of the frame. This includes an FEA to

analyze permanent deformations of the bicycle frames under the two drop-mass impact tests as mentioned above. Figure 3.7 shows the results of an FEA of the drop-mass impact test. The simulation colorized the distribution of permanent deformation of the bicycle frame along the longitudinal direction of the frame. The permanent deformation of the bicycle frame reaches from $2.06\,\mathrm{mm}$ up to $6.61\,\mathrm{mm}$. For structural performance prediction of bicycle frames, supervised Machine Learning and Automated Machine Learning (AutoML) methods are used [113].

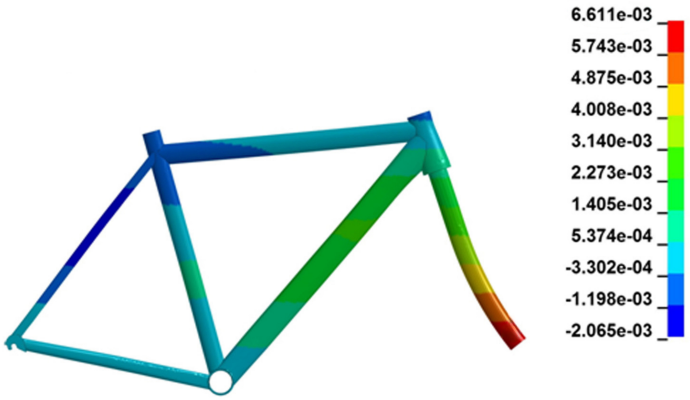

Figure 3.7. Deformation distribution of a bicycle frame along the longitudinal direction of frame for an exemplary drop-frame impact test (adapted from [32]).

Test Benches

Simulation results are often not as accurate as needed or are not in line with laboratory test results [69]. Hence **test benches** for bicycle frames are being developed in research and industry. Test benches focus, e.g., on vibration force measurements on the bicycle frame or frame stiffness measurements such as the test rig concept developed by Vanwalleghem et al. [129] (see Figure 3.8 a). The frame is mounted with the head tube between a column on one side and on the other side at the rear dropouts on the base plate of the test rig. The load on the frame is applied at the bottom bracket of the bicycle frame, either at the center or on both sides of the frame as well as at the center of the rear shaft, which connects the two dropouts. The frame was subjected to load using pneumatic actuators, which pressure regulators controlled in a closed-loop system. Feedback from force transducers, which measured the applied push or pull force on the frame, was used to regulate the actuators. The bicycle manufacturers and commercial test centers have already implemented similar concepts for frame stiffness tests [50]. In addition, bicycle frames are also often tested in situ measurements. Köllner et al. [86], e.g., presents the design and implementation of a measurement and analysis system for conducting field test studies on bicycles. This system can measure various structural responses, including strain and acceleration. It consists of 24 strain sensors, four acceleration sensors, and a compact data acquisition unit conveniently mounted behind the seat post. The system has been successfully deployed on a BMX bicycle, shown in Figure 3.8 c. The measurement and analysis system undergoes validation in typical cycling scenarios

and a race simulation conducted on a race track. In addition, individual components are also tested in conjunction with the frame. For example, this can also be done in situ, as illustrated in Figure 3.8 d. Drouet and Champoux [45] developed a specialized road bike stem with built-in sensors to facilitate on-site measurements of static and dynamic loads transferred through the stem-handlebar connection. The data acquisition system collects measurement data from the instrumented stem mounted on the bicycle. This system is connected to a modified backpack, which the cyclist wears during the data collection.

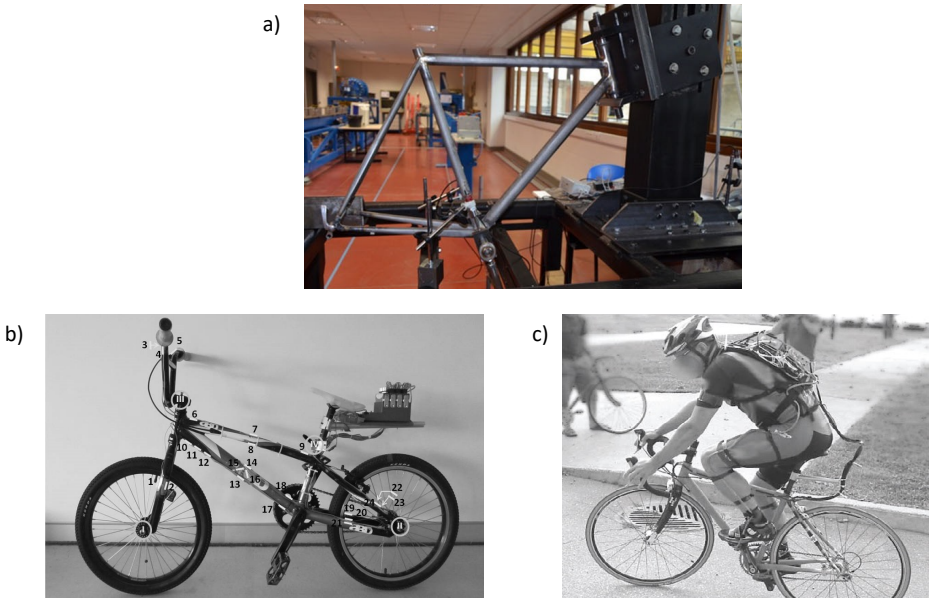

Figure 3.8. Overview of three different bicycle test benches. The upper part illustrates a standard test setups for frame (a). The lower part shows two test setups that allow in situ measurements (c, d) (adapted from [45, 86, 129]).

3.2.3 Problem Definition

The examination of a bicycle frame constitutes the second case study. The presented test benches in Section 3.2.2 only map exceptional load cases mostly from one direction, e.g., the seat post stiffness measurements from above. In order to determine the flexibility of the robot-based testing facility, a wide range of different test motions were selected (see Figure 3.9). The first load case applies a compression force to the seat post, the second load case applies a compression force to the head tube, and the last applies a compression force to the seat tube. In each case, linear compression motions that press horizontally on the corresponding bicycle component will be carried out with the velocities and compression forces as summarized in Table 3.2.

As an exemplary bicycle frame, an aluminum frame (yellow/orange) with a carbon rigid fork (black) from the manufacturer Ziemer was chosen (see Figure 3.9). In order to be

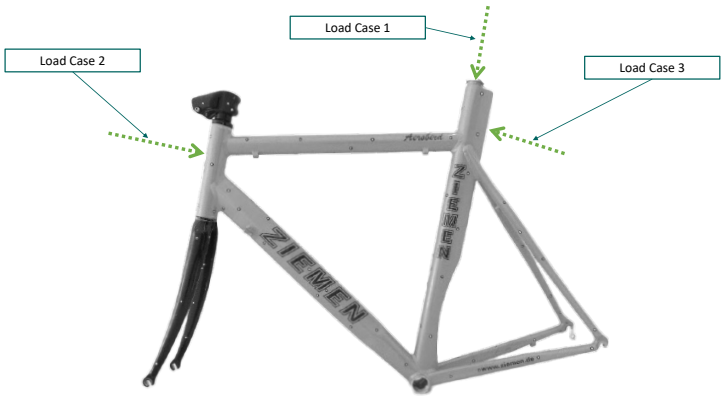

Figure 3.9. Overview of the different loading points with corresponding directions. The first load case applies a compression force to the seat post, the second load case a applies compression force to the head tube and the last applies a compression force to the seat tube.

Load Case	Forces	Velocities
1. Seat Post	2000 N	$5\,\mathrm{mm\,min^{-1}}$ until 100 N, continuing with $2\,\mathrm{mm\,min^{-1}}$
2. Head Tube	1000 N	$5\,\mathrm{mm\,min^{-1}}$ until 100 N, continuing with $2\,\mathrm{mm\,min^{-1}}$
3. Seat Tube	500 N	$2\,\mathrm{mm\,min^{-1}}$

Table 3.2. Bike load case overview with corresponding forces and velocities.

able to carry out these tests, a suitable fixture and the appropriate end effector for the robot-based test bench must first be developed. The respective frame shape must be taken into account in order to create a form fit. The robot-based test bench also needs to be capable of achieving compression forces up to $2000\,\mathrm{N}$ with velocities between $2\,\mathrm{mm\,min^{-1}}$ and $5\,\mathrm{mm\,min^{-1}}$. In addition, it must be possible to measure the forces during the test sequence as well as the elongation or movement of the bicycle frame. Furthermore, the accuracy of the placement of end-effector to the component must be investigated.

3.3 Case Study 3: Snowboard

Alpine winter sports, including skiing and snowboarding, attract a substantial part of the population. Like other sports, snowboarders require equipment that prioritizes safety and attends to the diverse skill levels of participants. In order to achieve this, manufacturers produce snowboards with a range of materials and designs, allowing for variations in flexibility, damping, weight, and cost. To enhance safety and to provide

desirable ride and handling characteristics or adequate strength, mechanical testing procedures and test benches have been devised to evaluate snowboards. The snowboard testing is suitable as a case study for robot-based components because snowboards have different material properties than the previous case studies. This results in other challenges for a robot-based test bench and will be discussed in Section 3.3.3.

3.3.1 Fundamentals

Snowboard Structure

The manufacturers have introduced a variety of different **snowboard structures** characterized by different shapes and materials. A geometrical representation of a (symmetric) snowboard is illustrated in Figure 3.11 and termed according to the ASTM1107 [2]. The nose and tail are a snowboard's front and rear ends, respectively. They can have various shapes, including round, pointed, or slightly tapered. The design of the nose and tail affects the board's float in powder snow and its performance in different terrain conditions. The snowboard's length refers to the distance from the tip (nose) to the tail. It determines the overall size of the snowboard and affects factors such as stability, flexibility, and maneuverability. The width of the snowboard is measured at its narrowest point, typically at the center between the bindings. A snowboard's sidecut radius (R_{avg}) represents the curvature of the edges along the snowboard's length. It determines the turning radius of the snowboard and influences its maneuverability. Snowboards feature mounting inserts where the bindings are attached. The snowboard stance refers to positioning a rider's feet on the snowboard. It involves the placement of the bindings on the snowboard and the angles at which the bindings are set. Finally, the contact length defines the length along the edge where the board interacts with the snow surface during turns, maneuvers, and overall riding. [26]

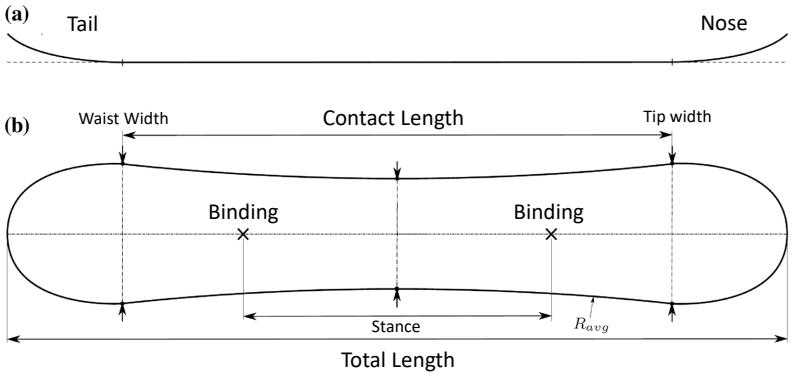

Figure 3.10. Geometrical representation of a symmetric snowboard from a side view (a) and a top view (b) (according to [26]).

Sandwich Construction

The majority of snowboards is constructed using a technique known as **sandwich construction**. This construction method involves layering individual elements in a mold, similar to assembling a sandwich. The assembled layers are then pressed and subjected to heat and pressure. This process effectively bonds all the elements together, forming

the snowboard. The mechanical properties of the sandwich structure and its constituents ultimately determine the characteristics of the snowboard, including factors such as bending and torsion stiffness, flex, and twist. An exemplary sandwich construction of a snowboard consisting of five individual layers is illustrated in Figure 3.11. The top sheet (1) is the visible outer layer of the snowboard. It is typically made of a polymeric material, such as P-Tex or ABS, and can feature various graphics or designs. While the top sheet adds aesthetic appeal, it does not significantly contribute to the board's structural properties. The Layers of fiberglass (2, 4) are applied to both the top and bottom of the core. Fiberglass provides stiffness and reinforcement to the board, enhancing its responsiveness and durability. The number of fiberglass layers and their orientation can vary depending on the desired characteristics of the snowboard. The core (3) is the heart of the snowboard and provides its central structural integrity. Most snowboards use a wood core, while other models incorporate materials like carbon fiber for added strength and performance. The core also contributes the most to the flex of a snowboard. The snowboard flex refers to the degree of stiffness or flexibility of a snowboard along its length. This includes the longitudinal flex along the length of the snowboard, from the tip to the tail, and the torsional flex, which refers to the twisting or rotational flexibility of the snowboard. The base (5) is the bottom surface of the snowboard that makes contact with the snow. It is typically made of high-density polyethylene material. The edges are usually bent into the shape of the corresponding snowboard and then glued to the base. Most snowboards have wrapped edges, meaning they go continuously along the snowboard's edge, tips, and tails. [24]

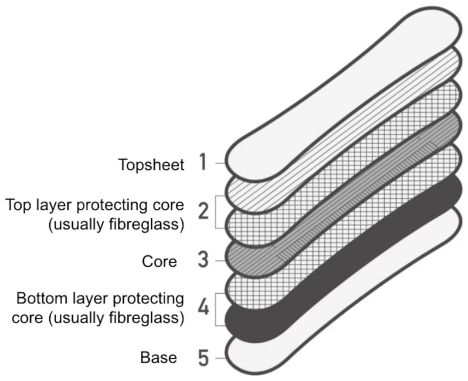

Figure 3.11. Exemplary sandwich construction of a snowboard consisting of five individual layers from the top sheet (1) to the base (5).

3.3.2 State of the Art

As with material testing of bicycle frames, various methods and test rigs for testing snowboards exist in research and industry, too. Simulative and practical approaches are also used to determine and test material properties to improve quality and avoid serious accidents.

Test Simulation

Several research topics focus on **simulating** bending, board shape and torsional stiffness distributions [27, 33, 116]. Sakata et al. [116], e.g., evaluated snowboarding performance quantitively by developing a simulation of the influence of board shape, elastic modulus, and stiffness on the characteristics of the turning motion. They used a finite element method (FEM) to simulate the snowboard's deformation, while the snowboard's translational and rotational motions were calculated by numerically solving the equations of motion with six degrees of freedom. Furthermore, Clifton et al. [33], e.g., developed a prediction model for calculating bending and torsional stiffness properties for snowboards with sandwich composite construction.

Test Benches

To validate the developed simulations and in order to gain further insights, snowboards are also tested mechanically on specifically designed **test benches**. Clifton et al. [33] validated, e.g., their previously mentioned simulation model with standard mechanical static bending and torsional deflection tests. They used standard tests described by Subic et al. [124], illustrated in Figure 3.12 a and b. The developed procedures for the tests are primarily based on ISO Standard 5902 [1], which defines the elastic properties of alpine skis. In order to adapt the procedures for snowboards, several modifications were implemented because, e.g., each ski only possesses one binding. The test bench illustrated in Figure 3.12 enables the determination of the bending stiffness in the body section of the test boards. It comprises a C-channel base measuring $1.5\,\mathrm{m}$ in length, along with two adjustable supports equipped with $20\,\mathrm{mm}$ diameter rollers capable of accommodating the entire width of the snowboard (from tip to tail). Additionally, there is a load application device denoted as F, which consists of two $20\,\mathrm{mm}$ diameter rollers supporting two $16\,\mathrm{kg}$ masses attached by hooks. Figure 3.12 b shows an test bench for the determination of the bending stiffness. They used an alternative clamping consisting of $40\,\mathrm{mm}$ wide metal plates to secure the snowboard. The section under examination was subjected to torsional forces using a dual system. This system involved suspending a mass on one side of the snowboard section, while on the opposite side, a mass was used to pull the board upward through a pulley and flagstaff mechanism. These specific test benches are often used in research [52, 135]. In addition, there are many even more specialized tests for evaluating more complex forces or torques. The dynamic rig displayed in Figure 3.12 c, e.g., consists of two separate pneumatic cylinders that replicate the movement of a rider's feet. Additionally, three adjustable pressure airbags are used to mimic snowboarding terrain. These airbags can vary their pressure to simulate different configurations of the terrain [125] to evaluate the on-snow performance of the snowboard. Figure 3.12 d, shows a testing machine that simulates a heel-side turn. For this purpose, four pneumatic actuators replicate the capability of a rider to exert forces at either the toes or heels of each leg [25]. Moreover, snowboards are also often tested with in situ measurements. Buffinton et al. [25], e.g., conducted field testing to gather a comprehensive database of snowboard dynamics. They applied multiple strain gauges and one accelerometer on a snowboard and investigated a variety of scenarios during field tests. Finally, it should be noted that, as with bicycles, individual components are also tested in conjunction with the snowboard. Wolfsperger et al. [135], e.g., investigated in mechanical and dynamical properties of racing snowboards and their modification by different binding plates.

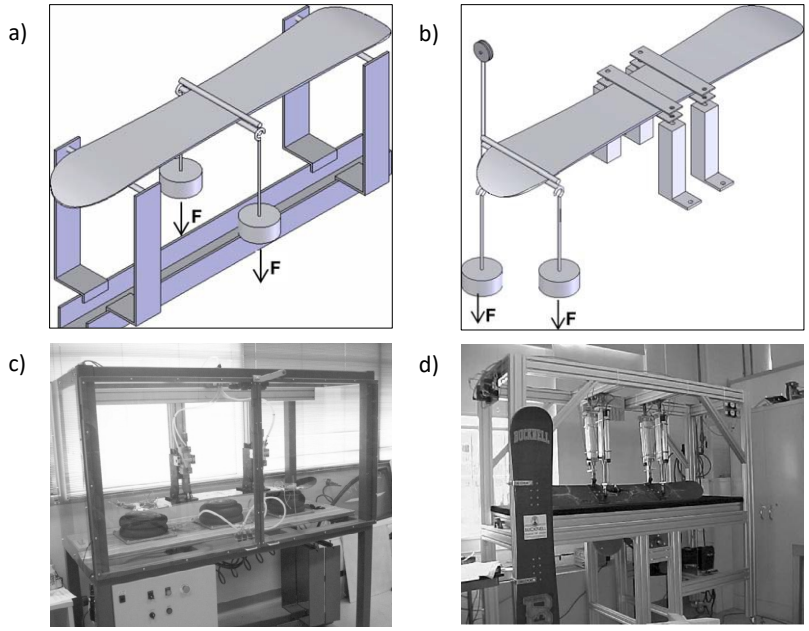

Figure 3.12. Overview of four different snowboard test benches. The upper part illustrates two standard test setups for bending (a) and torsional (b) stiffness. The lower part shows two test benches that replicate the motions of a rider's feet (adapted from [25, 124, 125]).

3.3.3 Problem Definition

As a third case study for the robot-based testing facility, the test of a snowboard was chosen. Besides the fact that the presented test benches in the previous Section 3.2.2 and the above presented snowboard test benches only map exceptional load cases for dedicated components, the testing of a snowboard evolves new challenges. Due to its defined design and sandwich construction, a snowboard is a test object that is soft to bending and torsion in contrast to very rigid test objects such as tensile or bicycle frames. A snowboard deforms immense when force or torsion is applied to it. Thus the test of a snowboard defines unique test motions and challenges to this test motions.

An exemplary snowboard (see Figure 3.13) and two test motions were chosen to identify and evaluate these challenges. The snowboard has an overall length of $160\,\mathrm{cm}$, a contact length of $134\,\mathrm{cm}$, a stance of $48\,\mathrm{cm}$, a waist and tip width of $30\,\mathrm{cm}$ and a thickness in the stance zone of $11\,\mathrm{mm}$ and at the tail or nose of $7\,\mathrm{mm}$

In this case study, two different test motions were selected, where the snowboard deforms to a great extend. The first motion (see Figure 3.14) tests bending stiffness as exemplarily described in Section 3.3.2 above. In contrast to the example above, in this case, the load vector, which is illustrated in Figure 3.14, should always be orthogonal to the snowboard over the whole testing motion, despite bending. This kind of motion, with the steady orthogonal load vector, cannot be implemented with standard testing machines. This is mainly due to linear actuators, which have only one degree of freedom. To overcome

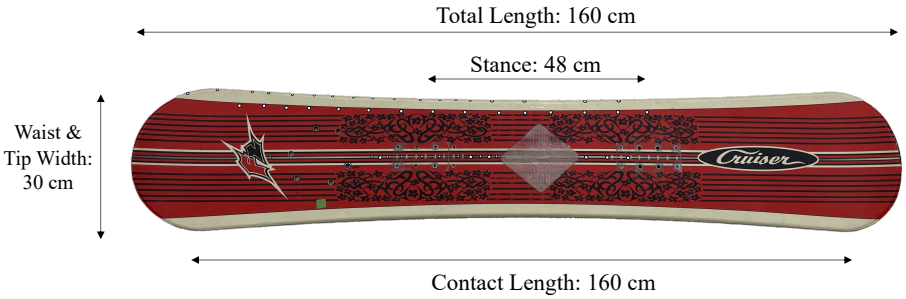

Figure 3.13. Dimensions of the selected snowboard

this issue, special testing machines with coupling rods or multiple linear actuators (see Figure 3.12 d)) are often used to enable such testing motions and, therefore are even more specialized for a singular component or use case.

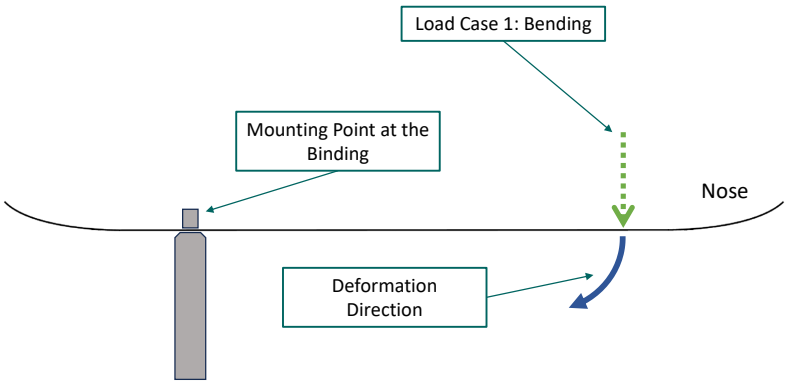

Figure 3.14. Exemplary illustration of the first load case including the bending motion direction and anticipated deformation direction.

The second testing motion goes even further. Here, superimposed loads are to be tested in which bending and torsion are applied simultaneously to the snowboard (see Figure 3.15). This test motion, too, can only be realized with a dedicated test bench. The in Figure 3.12 d implemented test bench, e.g., uses two linear actuators to enable the torsion of a snowboard. However, a more complex structure is necessary to expand this simple motion to a superimposed testing motion.

In addition to the motions, the velocities and loads also define the test case. Table 3.3 summarizes these requirements for testing the snowboard:

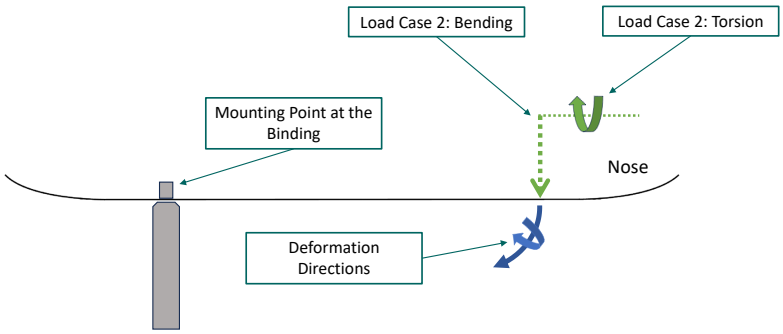

Figure 3.15. Exemplary Illustration of the second load case including the bending motion direction, torsion direction and anticipated deformation directions.

Load Cases	Forces	Velocities
1. Bending	150 N	$50\,\mathrm{mm\,min^{-1}}$
2. Bending and Torsion	150 N	$50\,\mathrm{mm\,min^{-1}}$ for bending and $10\,\mathrm{mm\,min^{-1}}$ for torsion

Table 3.3. Snowboard load case overview with corresponding forces and velocities.

In order to be able to carry out these tests, a suitable fixture and the appropriate end effector for testing snowboards must first be developed. The respective snowboard shape must be taken into account. For the second test motion, the end effector must be firmly connected to the snowboard to apply torsional forces. The robot-based test bench also needs to be capable of achieving (torsional) forces up to 150 N with velocities up to $50\,\mathrm{mm\,min^{-1}}$. In addition, it must be possible to measure the forces and torques during the test sequence as well as the elongation or movement of the snowboard. Furthermore, the accuracy of the placement of the end-effector to the component must be investigated.

3.4 Case Study 4: Automotive Component

The automotive industry, along with other manufacturing sectors, has also experienced a notable impact from the rise of Industry 4.0 and the adoption of the shift from mass production to mass customization in order to produce individual products in small quantities [87, 115]. However, to turn in account the benefits of Industry 4.0, e.g., in the automotive sector, mechanical testing needs to undergo a transformation to test individual products. When considering the mechanical testing of a vehicle, crash tests are commonly related as the primary focus. These tests aim to assess the impact behavior of structures, enabling the design of vehicles that minimize the severity of accidents. However, numerous load situations arise beyond these specific scenarios during vehicle operation. The body, the chassis, and all further parts of the vehicle must

be engineered to withstand such loads. Crucially, the connection points, such as the chassis suspensions, represent critical areas susceptible to crack formation, which can lead to structural failure under sustained loads. Similar to bicycle frames, these issues in automotive structures often stem from design, manufacturing, or material-related defects. Manufacturers conduct comprehensive testing on both individual components and complete automotive structures to mitigate accidents resulting from these factors. One vital part of a vehicle is the subframe, which, on the one hand, absorbs transmitted vibrations from the road or engine and, on the other hand, increases and optimizes the rigidity of the car body. Testing a subframe introduces additional complexities attributed to its intricate construction and multiple loading points that may require simultaneous loading. This characteristic renders it fitting for the fourth case study.

3.4.1 Fundamentals

A subframe is an integral part of a vehicle, whether an automobile or an aircraft, that utilizes a distinct and separate structure within a more significant component, e.g., a car body (see Figure 3.16). A subframe is securely attached to the vehicle through bolting or welding. Rubber bushings or springs are sometimes incorporated into the subframe to mitigate vibrations. Modern vehicles utilize separate front and rear **subframe positions**. A subframe supports and accommodates specific components like the engine, drivetrain, or suspensions. Subframes are usually made of pressed steel panels that are welded or spot welded together. Since lightweight is also a strong driver to apply aluminum or titanium in subframes. [111, 119] Subsequently, the automotive industry is working to bring carbon fiber reinforced polymer composite to vehicle's subframes [130].

Subframe Position

As mentioned before, a number of different vehicle **components** are mounted on subframes. The position of the single components is illustrated in Figure 3.17. The mounted components have the following functions [111]:

Subframe Components

- The **thrust panel** is attached to the underside of the subframe. It is often made of a sheet of aluminum and serves mainly to stiffen the entire front end of the car and to close off any free space below the engine.

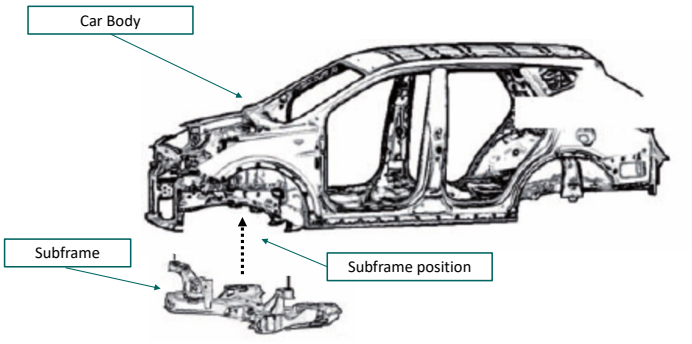

Figure 3.16. Position of a front mounted subframe (adapted from [85]).

- The **steering gear** converts the steering and turning movements of the steering wheel introduced by the driver into sliding movements of the track rod. This leads to a simultaneous rotation of both front wheels, resulting in a right or left vehicle movement.
- The **motor bearing** supports the weight of the motor. The bearings must not fall below a certain stiffness; otherwise, the natural vibrations of the motor will be passed on.
- The **drive shaft** serves the purpose of transferring power from the transmission to the drive wheel. The drive shaft is typically inserted into the transmission without being rigidly connected to the subframe. The subframe in Figure 3.17 features two large circular openings on each side through which the drive shaft is inserted. However, since the drive shaft is not permanently attached to the subframe it does not transmit any forces.
- The **stabilizer bar** connects the front wheels through the wheel suspension, effectively minimizing the vehicle's roll angle during cornering. When cornering, the roll angle occurs as a result of the unequal deflection of the wheels on the outer and inner sides of the curve, with the outer wheels experiencing more significant deflection. The stabilizer bar comprises a coiled spring connected to the wheel suspension and, thus, to the subframe using elongated rods. When there is a variation in wheel deflection, the spring undergoes torsion, creating a twisting force. This torsional moment counteracts the rolling motion of the vehicle, effectively limiting the roll angle. The subframe in Figure 3.17 uses a different stabilizer technique, so none is shown here.
- The **wishbone** is classified as a suspension control arm that is positioned horizontally across the wheel (see Figure 3.17). Its purpose is to connect the wheel to the subframe via its pivot points, providing vertical guidance to the wheel carrier via the carrier joint and maintaining its position (see Figure 3.18). The wishbone

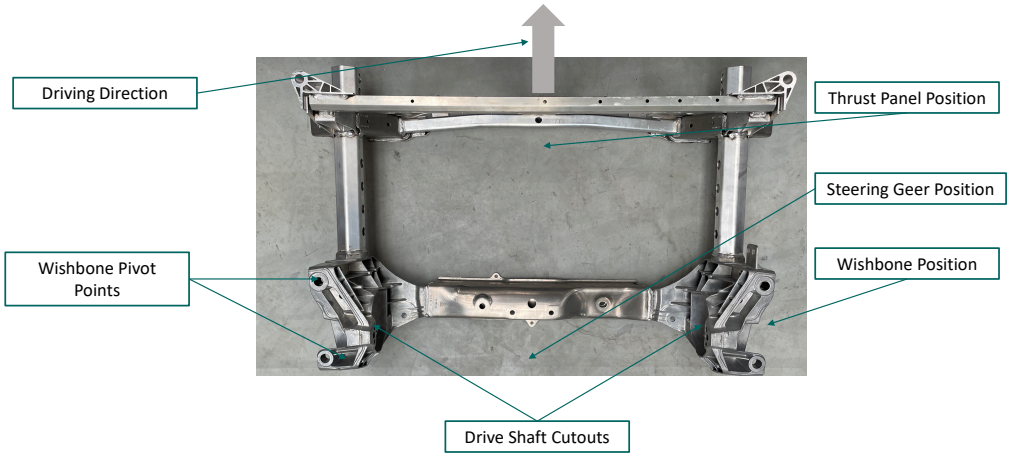

Figure 3.17. Subframe components and their position.

experiences significant tensile and compressive forces that are transferred to the subframe. Its primary function is to absorb lateral forces transmitted to the vehicle through the tires.

The primary function of a subframe is to distribute and absorb high loads. These loads can originate from the vehicle or its components themselves. For instance, in an automobile where the powertrain is contained within a subframe, the forces generated by the engine and transmission can be sufficiently dampened to avoid disturbing passengers. External forces and moments acting on a vehicle can be classified according to their direction of action. Thus, a distinction is mainly made between **longitudinal, vertical, and lateral dynamics**. Forces that act along the vehicle axis can be categorized into longitudinal dynamics. The driving force is generated when the vehicle accelerates, overcoming frictional forces between the tires and the road to set the vehicle in motion. Conversely, the braking force is applied to decelerate the vehicle and bring it to a stop. Vertical dynamics, on the other hand, involve forces acting along the vehicle's vertical axis. These forces mainly arise from uneven road surfaces and rolling and pitching motions that result in vehicle vibrations. Dampers and springs are designed to absorb these movements and provide optimal ride comfort by minimizing vibrations and natural frequencies within the vehicle. Lateral dynamics encompass forces that act transversely to the vehicle axle, primarily generated by steering movements. These forces are only present when the vehicle moves around its vertical axis. The cornering force, acting on each tire, is directed toward the center of the curve and ensures the vehicle maintains a stable path. In contrast, the centrifugal force pushes the vehicle outward from the curve. The cornering and centrifugal forces are transmitted to the road through the tire's contact surface. The magnitude of these forces and moments is influenced by factors such as the curve radius, wheel steering angle, acceleration, and aerodynamic flows. The lateral forces and moments are transferred from the wishbone to the subframe, as depicted in Figure 3.18. [46, 96, 111]

Driving Dynamics

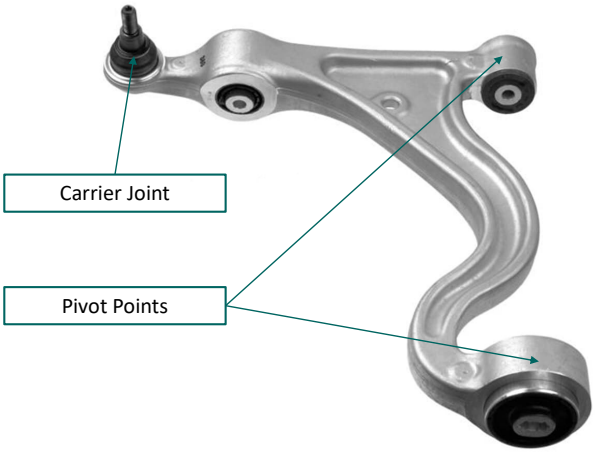

Figure 3.18. Exemplary Illustration of a wishbone.

3.4.2 State of the Art

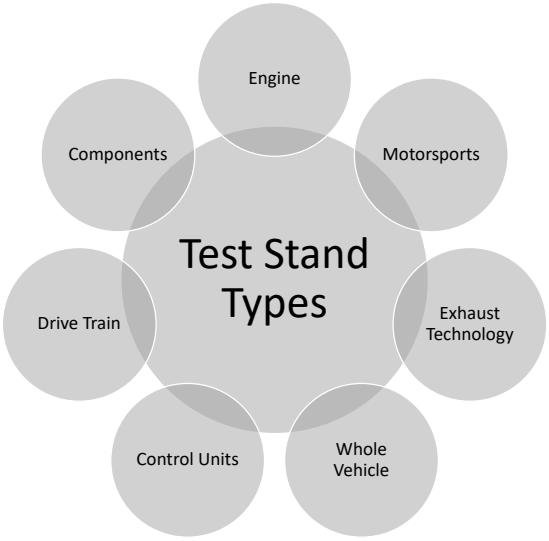

Figure 3.19. Classification of test benches according to test specimens in automotive engineering (based on [109]).

Test Rig Classification

A vehicle is a much more complex component than a bicycle or snowboard. This complexity also affects the variety of methods and the complexity of test rigs for testing automotive components. A possible **classification of test rig types** by test specimen is shown in Figure 3.19. There is a single test stand for almost every type of test specimen. There are dedicated test benches for control units, engines, exhaust technologies, drive trains, components, or the whole vehicle. In addition, there are also test rigs for more particular applications, such as automotive racing. Both stationary and transient test benches are available for engines, offering stepwise or dynamic load adjustment capabilities. Component test rigs are used to test various components, such as transmission components, fuel cells, and electric motors, subjecting them to various load tests to evaluate their functionality. This allows assigning the subframe as a single component to the component test. While some test benches focus on individual specimens, comprehensive systems are capable of testing complete systems comprising multiple assembled components. These include powertrain test rigs, which accommodate a powertrain consisting of an engine, transmission, and drive shaft. For example, the forces acting on the subframe are also tested on such test rigs. Subframes can be tested individually or in conjunction with other components.

Test Simulation

Several research topics focus on **simulating** different mechanical characteristics of the subframe component. This includes the optimization of the subframe mounting system to reduce the interior booming [49] or the optimization of weight optimization design, e.g., for alloy subframes [97] or a titanium subframe s[119]. Moreover, fatigue or durability simulation analysis [89, 101] and structural strength modal analysis on

subframes are carried out [107]. As with the bicycle frame or the snowboard, FEM simulations are often used [97, 101].

Test Benches

To validate the developed simulations and in order to gain further insights, subframes are also tested mechanically on specifically designed **test benches**. For example, the gap between simulation and accurate mechanical testing is closed by Abrahamsson et al. [14] or Nam et al. [101]. They first mentioned calibrating their FEM model of a car front subframe against measured test data. They collected the data by applying vibrating forces with a shaker (1 N load magnitude) to the subframe and measuring these vibrations with accelerometers and force sensors directly mounted on the subframe [14]. Nam et al. [101] validated their nonlinear model (see Figure 3.20 a) on the prediction of the fatigue life of a subframe by applying forces at the center of wheels which were connected to the subframe via the suspension (see Figure 3.20 b). They attached strain gages on the subframe and measured the strain. Afterwards, they compared the real measured strain with the strain obtained from virtual test simulations. A test rig, depicted in Figure 3.20 c, was designed by the Technical University of Dresden [21] to facilitate static and dynamic chassis characterization. This test rig can accommodate different vehicle axles and accurately simulate wheel movements and forces in both horizontal and vertical directions. To achieve the kinematics, transmission between the hydraulic actuator and the wheel replacement system was realized with the bell cranks. To accurately measure the forces exerted on the body, strategically placed load cells are installed at critical points, including the connection points between the subframe and the body. The purpose of this test rig is to enable precise and reliable measurement of the forces acting on the vehicle's body during various dynamic scenarios.

3.4.3 Problem Definition

As the last and fourth case study for the robot-based testing facility, the test of a subframe was chosen. All test rigs presented up to this point, e.g., for tensile test specimens, bicycle frames, snowboards, and automotive parts, have in common that they were only designed for dedicated components. The presented load cases for the tensile and the bike frame require only one load case at a time and can thus be performed with only a single robot. Furthermore, using a robot to apply loads to a snowboard also enables even more complex load motions, which are made possible by its degree of freedom. Testing a subframe presents at least one more challenge, testing the component with more than one load at a time.

An exemplary subframe of a Porsche Panamera and three test motions were chosen to identify and evaluate these challenges. The in Figure 3.21 illustrated frame is made of an aluminum-magnesium alloy (AlSi10MnMg) and has the part number 971400048AH and external dimensions $1000\,\mathrm{mm}$ x $650\,\mathrm{mm}$. The subframe is a cast aluminum node construction with multiple transverse and longitudinal struts. Internally in the vehicle, this component is assigned to the front axle or axle beam assembly and is attached to the body. The two side parts of the subframe play a unique role, as they have a hexagonal structure (see Figure 3.21b). This ensures that even large forces are absorbed by the subframe in the event of a crash and that it is not completely crushed, as otherwise, the

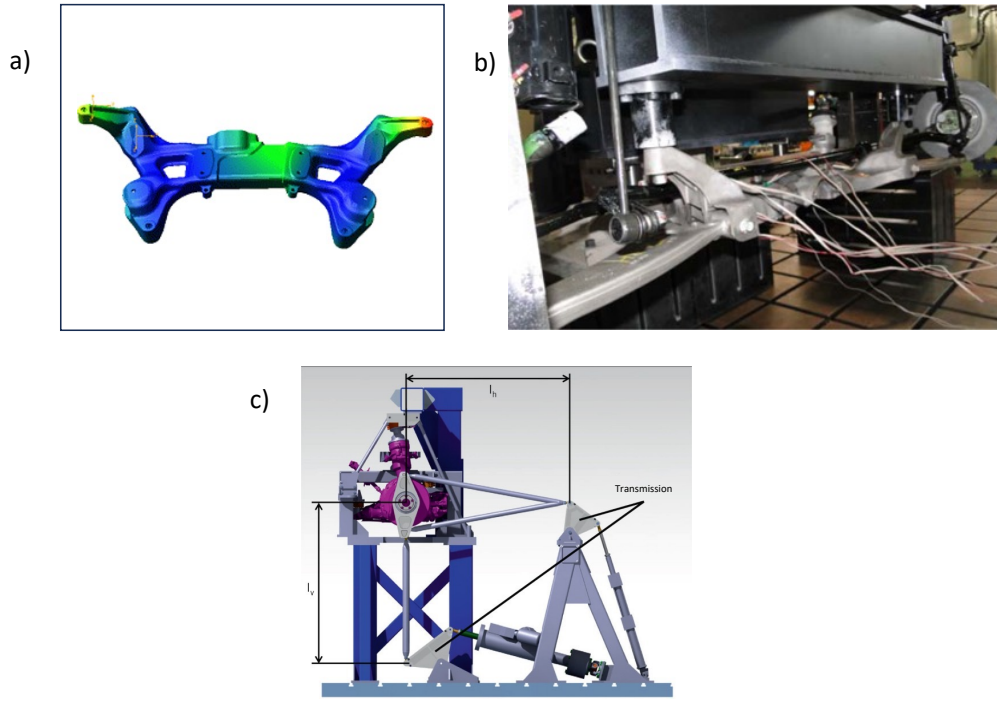

Figure 3.20. Overview of two different subframe test benches and one subframe simulation model. The upper part illustrates one subframe simulated model (a) which gets later compared to the measured data from the test stand shown in (b). The lower part shows a test benches that replicate car driving motions (adapted from [21, 101]).

entire engine of the vehicle would be pressed into the legroom of the driver and front passenger. Another peculiarity is that this subframe does not directly accommodate the stabilizers and steering gear.

As mentioned, lateral cornering and centrifugal forces are occurring, which are transmitted to the subframe via the wishbone. Therefore, three test motions were selected to simulate these forces and simultaneously act on the frame: Two compressive loads (load 2 and load 3) and one tensile load (load 1) (see Figure 3.22). These forces should be applied at the pivot points of the subframe where the wishbone is located.

In addition to the motions and the contact points, the velocities and loads also define the test case. Table 3.4 summarizes these requirements for testing the subframe:

Load Cases	**Forces**	**Velocities**
1. Tensile	5000 N	$5\,\mathrm{mm\,min^{-1}}$
2. Compression	5000 N	$5\,\mathrm{mm\,min^{-1}}$
3. Compression	5000 N	$5\,\mathrm{mm\,min^{-1}}$

Table 3.4. Subframe load case overview with corresponding forces and velocities.

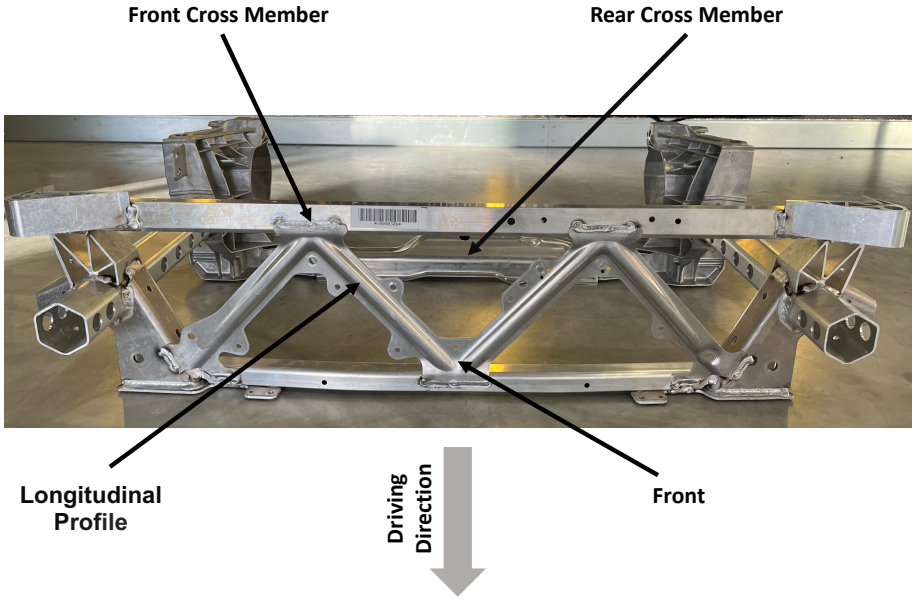

(a) Front view of the Porsche Panamera subframe.

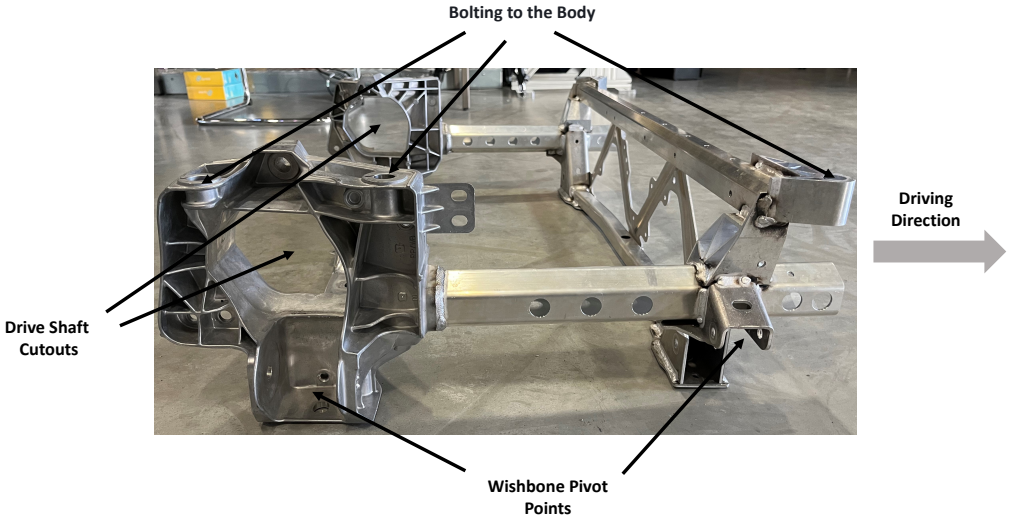

(b) Sideview of the Porsche Panamera subframe.

Figure 3.21. Overview over the chosen Porsche Panamera subframe component.

In order to be able to carry out these tests, a suitable fixture and three appropriate end-effectors for the subframe must first be developed. The respective subframe shape must be taken into account. For the test motion, the end-effectors need to be firmly connected to the subframe via the pivot points to apply the forces. The robot-based test bench also needs to be capable of achieving forces up to $5000\,\mathrm{N}$ with velocities up to $5\,\mathrm{mm\,min^{-1}}$ in parallel. In addition, it must be possible to measure the forces

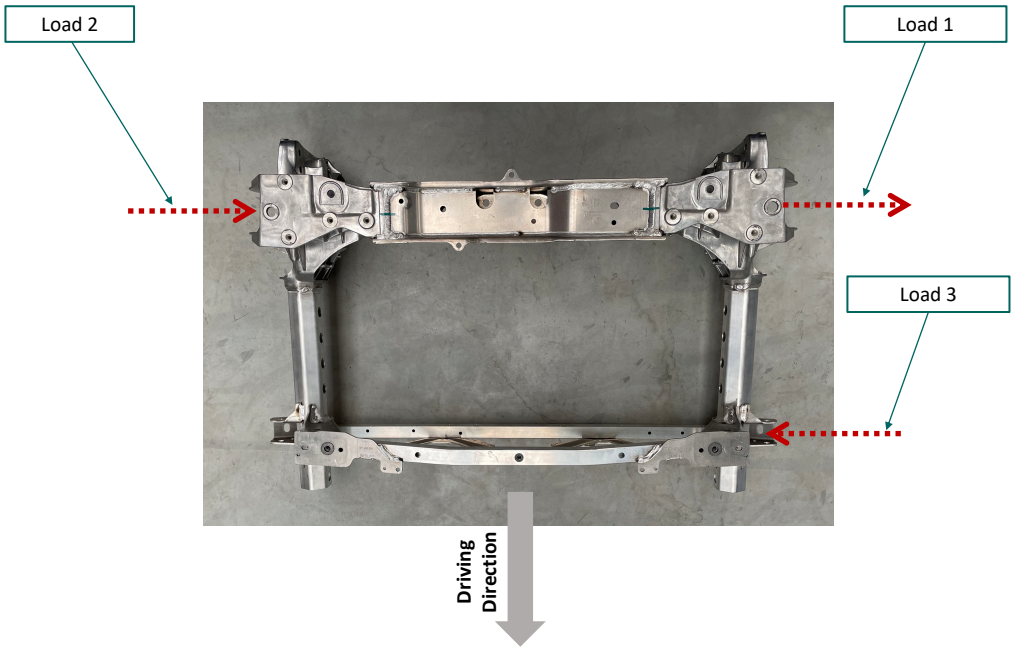

Figure 3.22. Exemplary Illustration of the three load case directions and load points on the subframe.

and torques during the test sequence and the elongation or movement of the subframe. Furthermore, the accuracy of the placement of the end-effector to the component must be investigated.

Summary. Based on the requirements of robot-based component testing, this chapter describes the developed and implemented robot-based testing facility. This includes the basic structure and all extensions, including additional sensors and actuators. Finally, an overview of the current state of the art and related work is given.

4

Development of a Robot-based Test Bench

The manufacturing industry is transitioning from mass production to mass customization, focusing on producing unique products in smaller quantities. However, this shift in production methods also necessitates innovations in methods to test these individualized products or their components. Building elaborate and specialized test benches for each unique component is no longer cost-effective, yet it remains crucial to perform thorough testing to ensure product quality. Traditional testing machines typically offer limited testing capabilities and are designed to meet the specific requirements of a single component. As a result, there is a growing need for a flexible test bench to accommodate various types of components and different testing motions. Robots offer the advantages of high reproducibility and flexibility in their movements (6 DoF) to perform such destructive component tests. Therefore, a development for a robot-based test bench is presented in this chapter.

The robot-based testing facility presented below shows how a test bench with two heavy-duty industrial robots, additional sensors, and actuators can be realized. It was first introduced in [55]. The first section outlines the particular requirements of robot-based component testing. The next section (4.2) shows a general overview of the test bench, followed by a detailed description of the plant and the robots' workspaces.

Subsequently Section 4.3 presents the sensors and actuators resulting from derived requirements. Finally Section 4.4 gives an overview of already existing concepts of robot-based and robot-assisted test benches for destructive and non-destructive testing scenarios.

4.1 Requirements of a Robot-based Test Bench

Based on the previously presented challenges of the selected case studies, the following hardware and software requirements (RE) for implementing a robot-based test bench need to be addressed to ensure accurate and reliable results.

RE 1 Flexibility
In order to create dynamic and customizable test setups, allowing for the examination of a wide range of components, such as the four distinctive components from the case studies, the testing facility must be designed as flexibly as possible. Flexibility can be achieved on the one hand by using hardware that is as flexible as possible, such as flexible clamping devices, and on the other hand by the developed software, which turns the polyfunctional robot into a flexible testing machine. The software is intended to customize the testing procedures and adapt to specific requirements resulting from different components. In doing so, designing and implementing simple and complex test motions or test sequences should be possible. The software should organize and present the data in a structured and flexible manner, allowing for easy analysis and interpretation. This data-driven approach enables researchers to extract valuable insights and make decisions based on the test results.

RE 2 Extensibility
Moreover, the collection and analysis of data during the testing process must be designed to be extensible since different components require different data records, such as force or displacement, or both at the same time. It should also be possible to quickly integrate new sensors if additional materials are to be tested. Integrating new actuators or sensors should also be facilitated since even more complex test cases can occur.

RE 3 Reproducibility
Reproducibility through software is vital for industrial applications of test benches. In manufacturing or quality control environments, consistent and repeatable testing procedures are essential to ensure product reliability and compliance with standards. Thereby variations and uncertainties in the testing process should be minimized. Reproducibility allows fair and meaningful comparisons between experiments, systems, or components. Researchers can recreate specific test scenarios or conditions with software-controlled test benches, enabling direct comparisons and evaluations. This is especially important when assessing different robotic systems, components' performance, reliability, or efficiency. Hence the test procedures of a robot-based test stand must also be reproducible.

RE 4 Slow Velocities
Unlike dedicated testing machines that are designed for specific components, robots typically have higher velocities up to $8\,\mathrm{m\,s^{-1}}$ due to typical tasks such as quick approach or depart motion, e.g., for welding processes [121]. In contrast, classical tensile tests described in Section 3.1.1 require very slow velocities, e.g., 1 mm/min for a steel specimen [7]. Initial examinations on the constructed robot test bench revealed that achieving the desired constant velocity of 1 mm/min for the slow acceleration curves of linear motion under load, necessary for this type of tensile test, proved to be exceedingly slow. This ultimately resulted in a malfunction of the KUKA robot controller (KRC 4). However, the objective was to swiftly attain and sustain the low test velocity, which proved unattainable using this conventional motion control method. Therefore, this leads to an additional requirement for modeling the motions and the general control concept.

RE 5 High Loads
Even simple tensile tests require forces of up to $20\,\mathrm{kN}$, e.g., for a steel specimen. Therefore, the robot's standard payload ($1\,\mathrm{kN}$ for the force) must be exceeded, to reach higher loads. Exceeding the maximum payload leads to further challenges since robots cannot apply the same force or torque in each pose. Therefore, a component must be placed on the clamping field where the robots can apply the required force or torque. Additional actuators, e.g., linear cylinders, can be used if the forces are insufficient. However, these must be integrated into the overall control system but often have proprietary interfaces. In conclusion, applying very high forces or torques also promotes the intrinsic deformation of the robot itself, which leads to the next requirement.

RE 6 High Accuracy
As described before, the intrinsic deformation of the robot itself poses a significant challenge. When discussing precision tasks under load, it's evident that the robot's accuracy falls short compared to that of a typical machine tool. This discrepancy can primarily be attributed to the robot's reduced stiffness, as noted in a study by Pan et al. (2006). Given that destructive material testing frequently demands both very high loads and high accuracy simultaneously, it becomes imperative to enhance the robot's tool precision under load conditions.

4.2 Robot-based Test Bench

A new test facility was designed and implemented to enable robot-based component testing and to realize the previously specified requirements. The following Section (4.2.1) first overviews the facility, including the used robots. Later on, Section 4.2.2 describes the position and working spaces of the robots.

4.2.1 Overview

The basic structure of the robot-based test bench is shown in Figure 4.1. It consists mainly of three parts. The basis is a $7\,\mathrm{m}$ length, $2.5\,\mathrm{m}$ width and $0.3\,\mathrm{m}$ height clamping field ①. This field has integrated T-slots over the entire length, in which the test objects

can be fixed with the help of clamping jaws. This allows the very flexible clamping of components at different positions with different orientations. The two KR 1000 titan robots developed by KUKA [75] ② are the most important part of the test bench. This type of robot was chosen because it stands out as one of the largest and most powerful robots available, specifically designed to handle heavy-duty applications with high precision and efficiency (RE 5). It is a six-axis industrial robot with a payload of $1000\,\mathrm{kg}$ and a pose repeatability (ISO 9283 [64]) of $\pm\ 0.1\,\mathrm{mm}$. Both robots are controlled by a KUKA KRC4 [76] controller each. Since the component size and, respectively, the flexibility of this test bench is limited mainly by the accessibility of the robots, the working space, and the positioning around the clamping field are described in more detail in the next section.

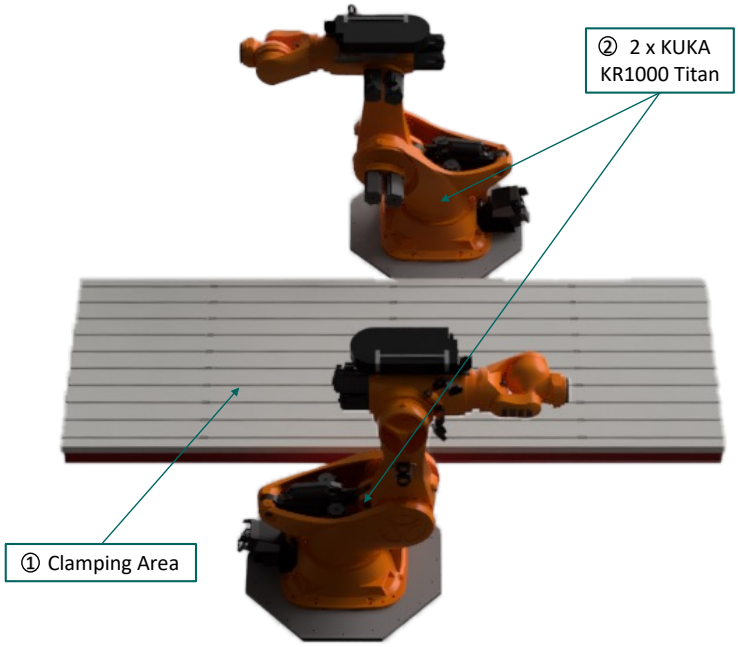

Figure 4.1. The facility for mechanical component testing consists mainly of a clamping area ① ($7\,\mathrm{m}$ x $2.5\,\mathrm{m}$) for the flexible positioning of testing components and two KUKA KR1000 titan heavy-duty industrial robots ②.

4.2.2 Dimensions and Working Spaces

The KR1000 Titan robot exhibits an extended horizontal and vertical reach, enabling it to access various points within its working space (see figure 4.2). It possesses a remarkable horizontal reach of $3.702\,\mathrm{mm}$. Vertically it can extend its manipulator arm up to $3.202\,\mathrm{mm}$ from its base. The working space, or the robot's overall reach, is defined by combining its horizontal and vertical dimensions. In the case of the KR1000 titan, the working space encompasses a substantial volume of $79.8\,\mathrm{m}^3$. The robot's end-effector can access any point within this spherical volume.

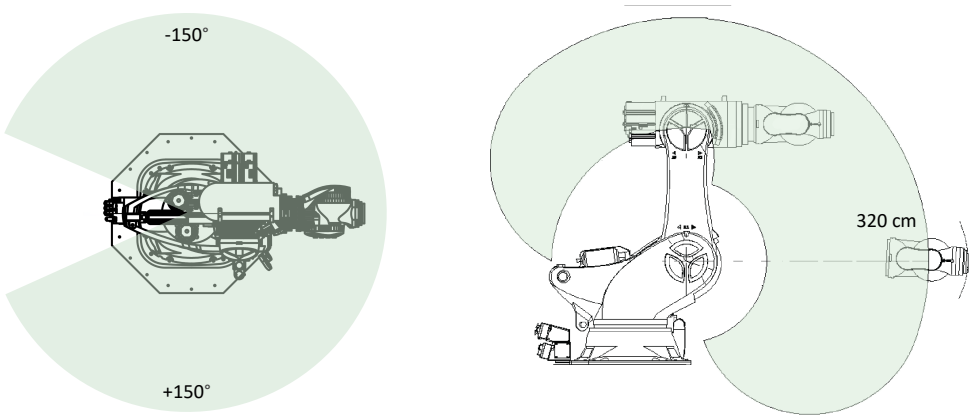

Figure 4.2. Working spaces of the KUKA KR1000 titan robot (extracted from [75]).

Furthermore, the position of the robots concerning the clamping field is significant. If, for example, a minor component needs to be tested, it must be placed within the range of both robots. The placement of the robots is illustrated in Figure 4.3. Both robots are $1250\,\mathrm{cm}$ away from the clamping field and are thus $5000\,\mathrm{cm}$ apart. Both robots are also slightly offset at a distance of $3000\,\mathrm{cm}$ from the left and right edge of the clamping field, respectively, so that they can better cover the clamping area with their reach. In order to utilize the entire working space of both robots, both are rotated 90 degrees to the clamping field and 180 degrees to each other. Furthermore, the Figure 4.3 depict the locations accessible by the robots, where forces or torques can be exerted. These areas are represented as circles within the clamping region, each with a diameter of 2.8 meters. This provides an initial estimate of the component size suitable for testing purposes. The possible workspace of each robot and the shared workspace is illustrated in a top-down view in Figure 4.3. In addition, the positions that the robots can reach and where forces or torques can be applied are illustrated as circles on the clamping area. Each circle has a diameter of 2.8 m. This gives an initial indication of the component size up to which testing can be carried out, and thus, it defines the limitations of these test benches. If the components are too small, the robots may obstruct each other. These problems can be solved using appropriate end-effectors. On the other hand, if the structures are too large, the problem occurs that they cannot be clamped onto the intended clamping field, or the reach of the robots may not be sufficient. The distance between the two robots gives a natural maximum size. If a component exceeds the width of 2.5 m or a height of 2.4 m and a rotation of this component is impossible, it cannot be tested. However, it also strongly depends on the component and the position of the load application points. In addition to the component measurements, other challenges will be explained in more detail in the next section.

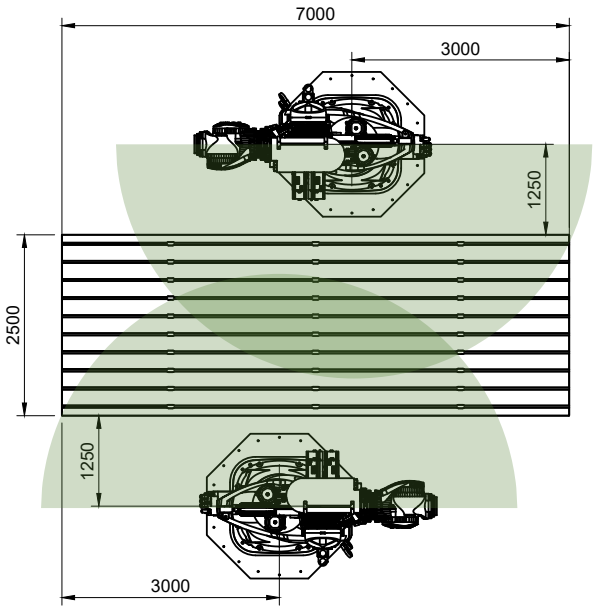

Figure 4.3. Robot placement and working spaces of the developed robot-based test bench.

4.3 Additional Sensors and Actuators

Addressing these challenges requires extensions of the generally developed robot-based test bench, involving sensor and actuator integration and adaptive control strategies, which can help overcome the challenges associated with flexibility, reproducibility, slow velocities, high accuracy, and high loads.

For higher loads, material characterization, as well as for motion execution and motion adjustment, additional sensors and actuators were integrated into the system. First, the integration of the additional linear cylinder EZ100 from the Manufacturer ZwickRoell is presented in Section 4.3.1. Section 4.3.2 depicts the extension of the robots with Multi-Axis Force / Torque Sensors. Section 4.3.3 explains the integration of the Stereoscopic Camera ATOS 5 from the manufacturer GOM. Finally, the developed robot-based test bench is compared with existing research and industrial test benches.

4.3.1 Additional Linear Actuator

To meet the requirements of flexibility and high loads even better, the test bench presented in Section 4.2 was expanded by an EZ100 linear test cylinder from ZwickRoell ③ and a clamping angle ④ as counterpart for axial force application. In order to remain as flexible as possible, these two parts can also be attached to the clamping field in any position (see Figure 4.4). The linear test cylinder can apply additional basic loads or stress conditions onto components. It is suitable for tensile and compressive loads up to $100\,\mathrm{kN}$ with speeds of up to $25\,\mathrm{mm/s}$ and a positioning repeatability with direction reversal $\pm\ 0.014\,\mu\mathrm{m}$. The range is defined by the position on the clamping

field and by the piston stroke of 200 mm. The cylinder is operated and controlled via the properties testXpert III control unit software from ZickRoell. In order to integrate the cylinder into the higher-level control system later on, it is possible to send it commands, such as starting and holding a certain force, via a telnet interface. Telnet is a network protocol used for remote terminal connections to communicate with devices in this case over ethernet-based network. It allows devices to access a remote host and perform tasks. Telnet provides a text-based interface for inputting commands and receiving responses [112].

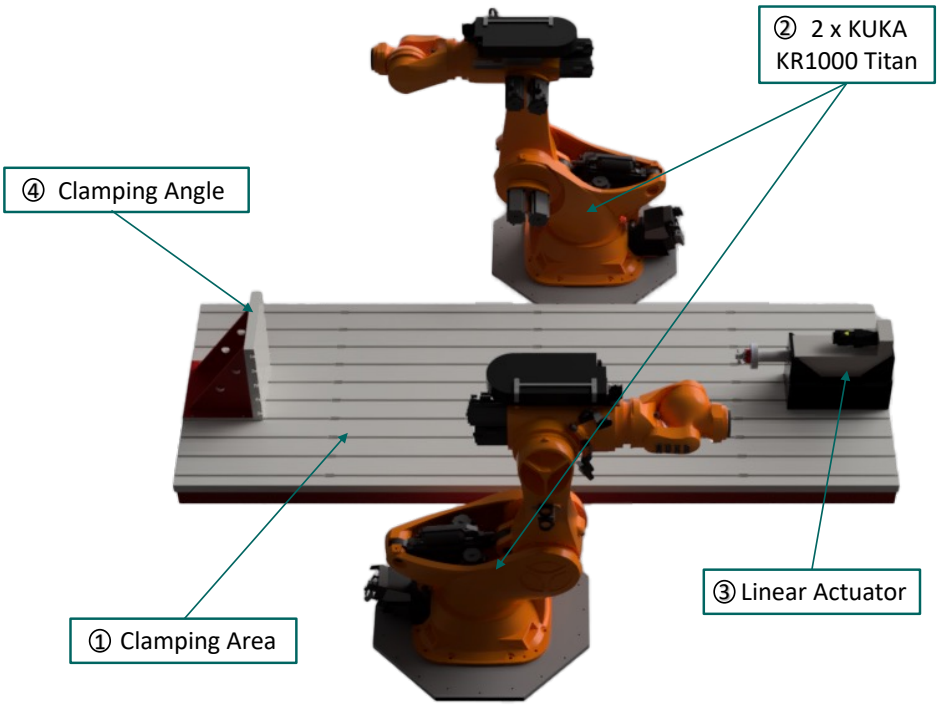

Figure 4.4. Extension of the facility for mechanical component testing with a linear test cylinder ③ and a clamping angle as counterpart ④. These two parts can also be flexible mounted on the clamping field.

4.3.2 Multi-Axis Force / Torque Sensors

For material characterization as well as for the motion execution and motion adjustment, both robots were equipped with a six-axis-Force-Torque-Sensor (see Figure 4.5). The sensor K6D175 from the manufacturer ME-Messsysteme was mounted directly on the robot's flange with an adapter plate. With this, it is possible to measure forces up to $\pm$ 100 kN in the z-direction and to measure forces in x- and y-direction up to $\pm$ 50 kN. In addition, it is also possible to measure torques up to $\pm$ 10 kN m in z-direction and torques up to $\pm$ 5 kN m in x-direction and y-direction. Whereas the z-direction represents the robot's tool impact direction , it is a right-handed coordinate system. Various end-effectors can be flexibly attached to the sensor. This sensor is directly connected to the GSV-8DS EC/SubD44H measuring amplifier, which is mounted on axis three on the robot. These amplifiers have a measuring frequency of 250 Hertz and provide their data via an EtherCAT interface. EtherCAT (Ethernet for Control Automation Technology) is a real-time industrial Ethernet communication protocol widely used in industrial automation. It is an open standard maintained by the EtherCAT Technology Group (ETG) and designed for fast and deterministic communication between industrial devices. EtherCAT utilizes standard Ethernet hardware and infrastructure, making it cost-effective and easily integrable into existing Ethernet networks. It achieves high-speed data transfer and low communication latency through a distributed clock synchronization mechanism. EtherCAT operates in a master-slave configuration, where the EtherCAT master controls the communication process and sends commands to the EtherCAT slaves. It supports various communication topologies like line, tree, star, and ring configurations, offering flexibility for different industrial automation applications. With this, it is possible to connect multiple measuring amplifiers in a line, one as a master and the others as slaves [65].

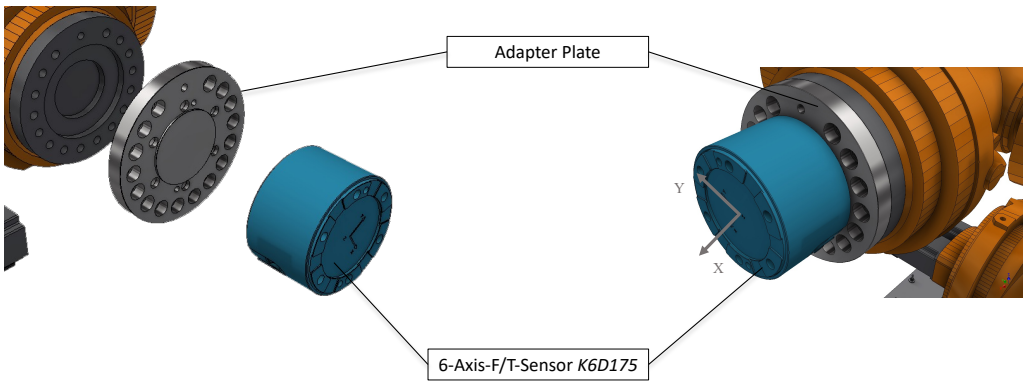

Figure 4.5. Mounting of the six-axis force/torque sensor K6D175 from ME on the flange of the KUKA KR1000 titan robot.

4.3.3 Stereoscopic Camera

To provide further valuable information for material characterization or components behavior and at the same time to have another possibility for sensor-guided motions, a digital image correlation (DIC) system was included in the robot-based test bench. The usage of these systems in the context of component testing is well established and common [127, 132]. The ATOS 5 system manufactured by Carl Zeiss GOM Metrology GmbH provides high-precision 3D metrology data, as explained in Section 2.2.2. This system can be used with different measurement volumes by switching lenses. In order to measure as many various component sizes as possible, three objectives were selected: MV 170, 700, 1000:

Name	Measuring Volumen	Working Distance	Data Density
MV 170	170 mm × 130 mm × 130 mm	880 mm	0.048 mm
MV 700	700 mm × 530 mm × 520 mm	880 mm	0.169 mm
MV 1000	1000 mm × 750 mm × 750 mm	880 mm	0.236 mm

Table 4.1. Three different lenses for the ATOS 5 System with different measuring volumes, diverse working distances and various data densities.

(a) Using the ATOS5 externally on a tripod.

(b) Using the ATOS5 mounted on the robots.

Figure 4.6. Two different mounting options for the GOM ATOS 5 Stereoscopic Camera System.

The MV 1000 can be employed for measuring larger volumes, such as when the robot's end-effector needs to be measured. However, it has a lower data density, which can pose issues when analyzing material properties. For instance, if the data density is too low, it may become impossible to observe material elongation. A smaller measuring volume with a data density, such as the MV 170, should be chosen in such cases. The ATOS 5 system also offers versatile mounting options, such as tripod mounting or direct attachment to the robot flange, as depicted in Figure 4.6. The adaptability in mounting and the possibility to switch lenses facilitate the inspection of various test component sizes, aligning with the concept of a flexible testing facility. For data processing during

experiments, the system employs ARAMIS Professional software. Two choices are available for real-time data processing. The first option records internally calculated values, including test space coordinates, in a local log file that continuously updates throughout the experiment. The second option features an SCPI Server (Standard Commands for Programmable Instruments), enabling access to measured data, such as the position and orientation of the robot's end-effector, over the network at a 10 Hz sample rate, along with supplementary information. SCPI is a standard communication protocol used in test and measurement equipment. It provides a standardized and consistent way to communicate with instruments, enabling seamless integration and automation in test systems and laboratory environments. SCPI defines a set of commands and queries that allow control and interaction with instruments over various interfaces, such as Ethernet or USB [118].

4.4 Related Work and State of the Art

In addition to the two component testing types described in Section 2.1, destructive and non-destructive, there are two distinct methods for utilizing robots in component testing: robot-assisted and robot-based. The first method involves combining a stationary standardized test machine with a robot. This combination is applied in various domains, ranging from material characterization, such as automated tensile testing [138], to applications in medical technology, like the analysis of stability and thermal wear of dental adhesive materials [36]. In this setup, the robot primarily loads specimens into the testing machine. In contrast, the second method, called robot-based approaches, primarily relies on robots, with other testing machines playing a secondary role in a supporting capacity.

Robot-assisted and robot-based approaches find their primary application in non-destructive material testing, particularly within manufacturing industries and production plants. They are typically used for in-line monitoring of clearly defined material or product properties, e.g., to check the tolerance or the quality of automotive resistance spot welds [66] or to enable fast and accurate inspection of the geometry of complex parts after stamping or other manufacturing processes with the help of vision technology [10]. However, there are already some robot-based test rigs for structure component testing. Beeh et al. [19] proposed a robot system for vehicle and airplane seat testing applications. The system setup manufactured and commercialized by the KUKA AG [79] consists of a KUKA industrial robot with a maximum payload of $150\,\mathrm{kg}$ with a flange mounted six-axis force/torque sensor. The KUKA OccuBot's software uses this force/-torque sensor to precisely reproduce human movements and loads. The test bench also allows realistic and practical simulations, such as boarding and disembarking procedures. Another commercial test rig is the Doorboto, a six-axis industrial robot system used at Nissan Technical Center North America. It is designed to mimic human-like actions and simulate repeated door-closing movements to ensure the durability and quality of Nissan vehicle doors. [104] A similar approach was published by Bhatkar et al. [20], which uses a six-axis industrial robot coupled with an intelligent gripper with sensors and feedback signal to simulate the effect of human touch during testing, e.g., for door

slam tests or door inner latch tests [20]. All mentioned approaches have in common that they are specially designed for a couple of use cases and are not very flexible.

In addition to the manufacturing industry, robot-based destructive material characterization plays a crucial role in medical technology. The utilization of robots in this domain offers the benefit of replicating realistic load scenarios under physiologically and repeatable conditions, allowing robots to simulate human body movements such as chewing motions [15] or knee joint motion sequences [68]. However, these robots are generally designed for specific use cases.

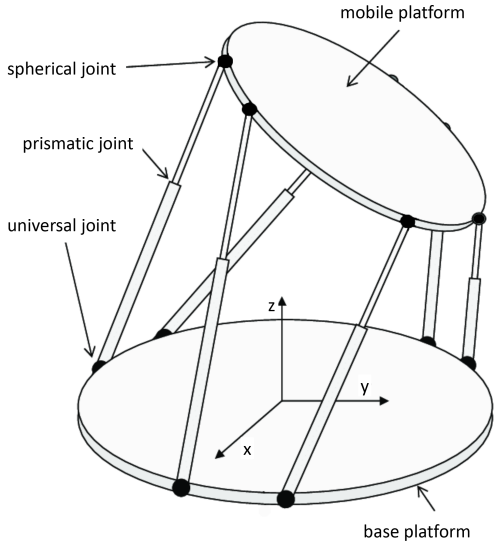

Figure 4.7. Schematic structure of a stewart platform consisting of six identical telescopic links, a mobile platform, and a base platform.

The initial comprehensive approach for robot-based destructive component testing takes the form of a hexapod, commonly called the Stewart platform. In Figure 4.7, the hexapod structure is depicted with links connecting the base and mobile platforms using universal and spherical joints. A prismatic joint controls the length of the links. The base platform remains fixed, while the mobile platform exhibits six DoF to the base platform: three translations along the x-, y-, and z-axis and three rotations around these axes. By coordinating the movements of the six legs, the platform can achieve precise positioning and orientation in three-dimensional space. The components to be tested are mounted between the fixed base platform and the mobile platform to apply multi-axial forces and torques. Several universities are actively researching this topic, including Hamburg University of Technology [126], the University of Cachan [103], the University of Paderborn [71] or the Delft University [40]. Furthermore, there are also some commercial hexapods, e.g., the multi-axial simulation table from MTS Systems [100]. This hexapod concept is especially suitable for determining the fatigue strength of components and large structures. Furthermore, it is possible to conduct measurements of static and dynamic stiffness and damping in addition to service life and

fatigue tests. A hexapod test rig, e.g., developed by the Delft University [40] (with x,y,z as shown in Figure 4.7) can achieve displacements in x,y,z direction up to $\pm$ 150 mm and rotation around x,y, z-axis up to $\pm$ 150°. This allows components with a volume of up to 1 m^3 to be tested. It can apply maximum forces up to $\pm$ 400 kN in x,y direction and up to $\pm$ 1000 kN in z-direction. The coordinate system will be presented in more detail in the evaluation. Moreover it can apply torques around the x,y axis up to $\pm$ 5 kN m and around the z-axis up to $\pm$ 1000 kN m. The presented hexapod test rigs are on a comparable scale [71, 100, 103, 126]. Even though the hexapod approach can handle high loads and offers six degrees of freedom (DoF), its construction imposes significant constraints, particularly regarding the test component's size and the limited range of motion. This sets it apart from the six-axis robots in the overview provided in subsection Section 4.2.1. The hexapod from Delft University, e.g., is specially designed and engineered for multi-axial fatigue testing of marine structural details.

Furthermore, it's worth mentioning that the imposition of combined loads using specialized testing equipment, such as biaxial systems [39, 139], the superposition of tensile and torsional loads [141], or testing machines designed for cruciform tests [140], is already a viable option. The biaxial test rig used by Delft University, e.g., has a maximum actuator stroke of $\pm$ 50 mm and $\pm$ 5° [39]. Thus these standard testing machines set-ups are usually not very flexible, and only a few selected load cases can be represented, or specific component sizes can be tested.

Summary. This chapter provides an overview of the fundamental aspects and structures involved in robot-based destructive component testing. For managing test complexity and ensuring test reproducibility a standardized test procedure was is described, which forms the basis for the subsequent chapters. Additionally an overarching architecture concept and a comprehensive data flow model gives a basic overview of the individual components and its interrelationships.

5

Concept of a robot-based test bench

The rising demand for personalized products with shorter lifecycles in the consumer market highlights the significance of flexible and small-volume production. To include effective mechanical testing at this scale, a paradigm shift is required in testing such components. In traditional mass production, testing is typically performed by test benches tailored explicitly to the specific product. However, this approach becomes less cost-effective for small batch sizes. There is a growing need for mechanisms that facilitate automatic mechanical testing, e.g., with robot cells, enabling swift product type changes in production.

To make the complexity of robot-based destructive component testing manageable and to ensure test reproducibility, a standardized test procedure is presented in Section 5.1. This procedure outlines the domain for a software-defined robot-based component test bench fundamentally and represents, therefore, the basis for the further chapters of this work. This Phase Model was first introduced in [55]. In order to manage and realize this procedure, an overarching architecture concept is described in the next Section (Section 5.2). In component testing, multiple devices and actors are involved in the testing process. The last Section (Section 5.2.2) presents a model of the data to be described and processed and their relationships to each other.

5.1 Phase Model for Standardized Test Procedures

The first phase is used for the test case **preparation**. This includes the analysis of the component, the determination of the test motions, and the resulting placement of the test component to the robot. In addition, the sensors for evaluation are determined, and, if necessary, a simulation is performed. In the second phase (**execution**), the actual component test is carried out. The recorded test data is processed and evaluated in the final phase, called **postprocessing**. The following sections explain the phases and their individual steps in more detail.

5.1.1 Preparation Phase

Component Analysis

The first phase, the preparation phase, consists of five steps and starts with the **component analysis**. This first step handles the definition of the component properties as these will later influence the further course of the test procedure since all further steps depend on the component to be tested. First, the dimensions determine whether a component can be tested at all. This, of course, depends on several factors, such as the acessibility by the robots or the size of the component. In this step, however, only an initial decision is made on whether the components fit on the clamping field or between the two robots. This can be decided with the help of the position of the robots and the dimensions of the clamping field presented in Section 4.2.2. If a component is, e.g., cube-shaped and has an edge length of more than $2.5\,\mathrm{m}$, it does not fit between the two robots. In contrast, rectangular components could be rotated, for example. When the component fits basically onto the clamping field, and between the two robots, the possible fastening points of the component must be identified in the next step in order to be able to decide how the component can be mounted. If it turns out that the component cannot be placed directly on the clamping field, suitable clamping devices must be designed in this sub-step. A tensile specimen, e.g., cannot be tested without a suitable fixture. For other components, however, fixing them with the help of the t-slot stones of the clamping field and clamping jaws is possible. The design of the clamping is also influenced by the material properties and the resulting loading points. Loading points specify where a force or torque will be applied directly to the component. In the case of the tensile test, the material can be PPH or steel, and only one load point can be applied at the end of the specimen. In this context, the design of the clamping device must ensure that the robot can initially reach these. This is also taken into account later in the component placement, and suggestions can be made to change the positioning. Finally, the appropriate end-effector must be mounted or manufactured, e.g., by 3D printing, in order to be able to test the component. The tensile tests, for example, require the appropriate clamping jaws mounted at the defector to be tested. The next step is the **test motion definition** in which the motions and their characteristics of the test actuators are defined. A distinction is made between three *motion types*: approach, testing, and departure motions for the robots and additional actuators, e.g., linear actuators. Approach motions are used to position the robot's end-effector on or before the component. Test motions are the executed test motions, and departure motions ensure a safe departure from the component. These three types

Test Motion Definition

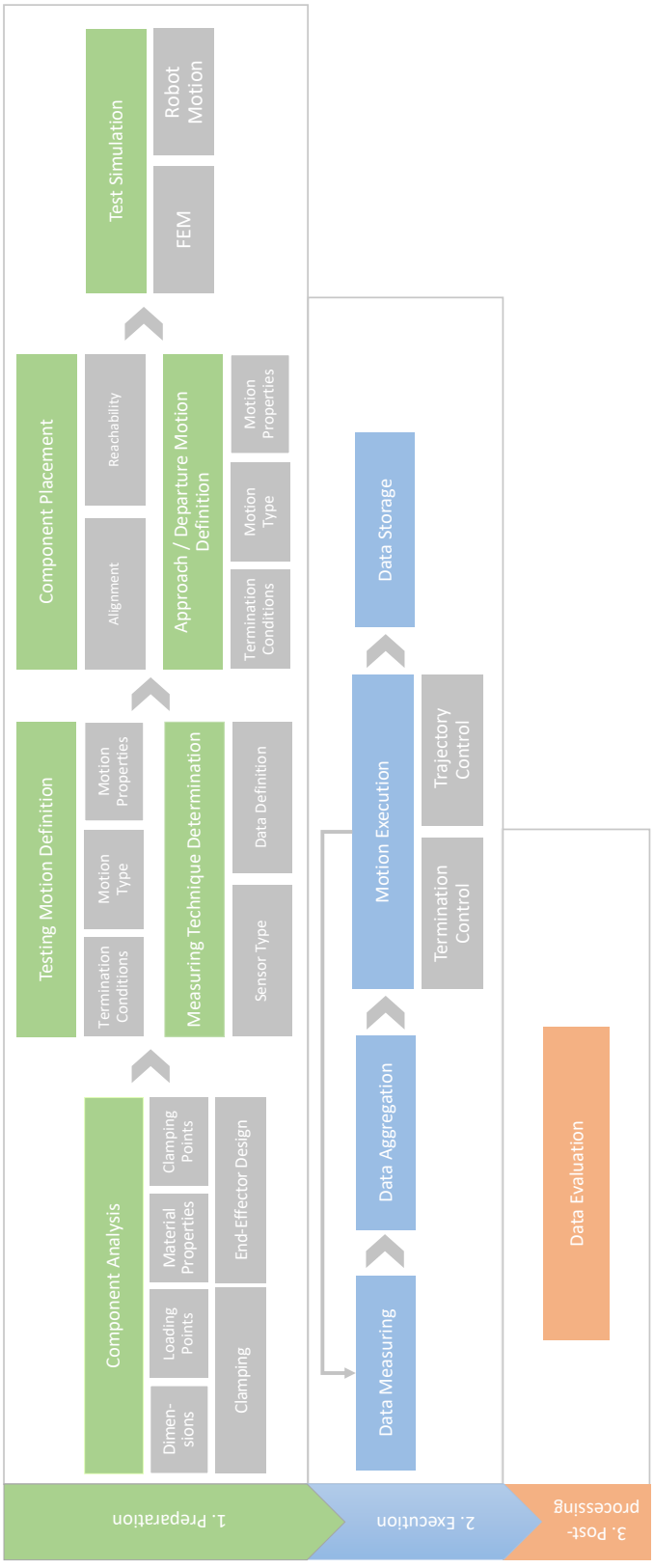

Figure 5.1. The standardized test procedure is comprised of three phases. The initial phase involves setting up the test case. The second phase, known as execution, details the actual execution of the component test. The concluding phase, referred to as post-processing, entails the evaluation of the recorded test data.

are explained and subdivided in more detail in Section 5.2.2. In this step, only the test motions should be defined since the approach and departure motions depend on the final placement of the component, and the test motion is only influenced by the end vector position in space. Test motions can be controlled in different ways. This control type is defined with the motion type at this point and will be explained in more detail in Section 6.1. In addition to the motion type, the properties of the motion must also be defined in this step. This includes the direction and velocities of the motion. The before-defined load points, in combination with the clamping devices, specify the motion direction. The velocities result, for example, from the material properties.

Lastly, the definition of abort criteria is imperative. These criteria are pivotal in determining whether a test motion is considered complete, concluding the entire test, or if the subsequent test motion can proceed. These criteria are also contingent on the material properties of the test component. Specifically, five criteria have been identified: maximum force, maximum torque, maximum time, maximum distance, and fracture. Further elaboration on these criteria can be found in Section 5.2.2. Additionally, the choice of the **measuring technique determination** must be established to gauge the material behavior of the loaded test component accurately. This entails measuring forces or displacements, which might necessitate the integration of additional sensors into the system. For instance, acoustic emission sensors can be employed to detect damage on both micro and macro scales, depending on the applied load, pinpoint its spatial location, and classify the type of damage. In this context, it is essential to specify the performance characteristics of the sensors in advance, including data volume and frequency, to seamlessly integrate them into the measuring and data aggregation framework. After conducting the component analysis, defining the test motions, and selecting the measuring technique, the optimal **component placement** can be determined. When determining the most suitable position for the component, numerous factors come into play, including geometric configurations, load directions, end-effector geometries, and testable component sizes for each robot. However, this geometric flexibility also presents an inherent optimization challenge since a specific test motion can be executed at various positions within the robot's workspace. To address this, a static force analysis model has been developed and combined with a constraint-based algorithm for automatic specimen placement, predicting the optimal position. This algorithm considers various factors, such as minimum height, often dictated by the clamping device and the end-effector. Further details on this algorithm can be found in Section 6.3. Simultaneously, the approach and departure paths must also be defined following determining the component's position. These paths are established in a manner analogous to the test motions. Finally, all these steps—component analysis, motion definitions, and component placement—lay the foundation for the subsequent simulation phase known as **test simulation**. With this approach, it becomes possible to simulate the entire process, commencing with the approach motion, progressing through the successive test motions, and concluding with the departure motions. The simulation of testing motions can also be integrated with a simulation of material properties, such as finite element analysis, to enable comparisons with the subsequent inspection phase.

Measuring Technique Determination

Component Placement

Test Simulation

Additionally, this integrated approach facilitates collision-free robot motion planning by incorporating the components as CAD models within the simulation environment.

5.1.2 Execution Phase

The second phase, the execution phase, encompasses five primary steps, commencing with the initial **data measurement** step. Here, data from the predefined sensors and actuators are collected. Given that these sensors and actuators provide data at varying frequencies, the subsequent step, referred to as **data aggregation**, is crucial to consolidate the data for the subsequent **motion execution** step. In this stage, the pre-established motions are carried out, with ongoing monitoring of termination criteria. Furthermore, due to the inherent influence of sensor measurements on the robot's motion, a cyclic execution is employed, allowing for potential adjustments. The phase concludes with the **data storage** of all recorded data.

5.1.3 Postprocessing Phase

In the third post-processing phase, the aggregated data is evaluated and visualized. This encompasses storing and associating the recorded test data with the corresponding test and component. Furthermore, the stored data can be a basis for optimizing load paths or test motions in subsequent tests. Any simulated data or previously simulated processes can also be archived for future reference.

5.2 Architecture

5.2.1 Main Components

In order to manage the execution of all phases of the standardized test procedure and to realize the previously specified requirements, an overarching architecture model was developed. It is depicted in Figure 5.2 and defines the following components:

Control Component
The control component is the main control component of the architecture for a robot-based test bench and is responsible for managing the execution stage of the standardized test procedure. While various internal classes manage numerous concrete operations, this class exposes all the essential interface options and delegates them to the appropriate subcomponents when necessary.

Planning Component
The planning component manages the preparation phase, user input, and output handling. This class exposes all the essential interface options to the user and delegates them to the appropriate subcomponents when necessary.

Sensor
The Sensor components handle all operations related to concrete sensor devices. This involves direct communication with the devices to send or receive sensor data.

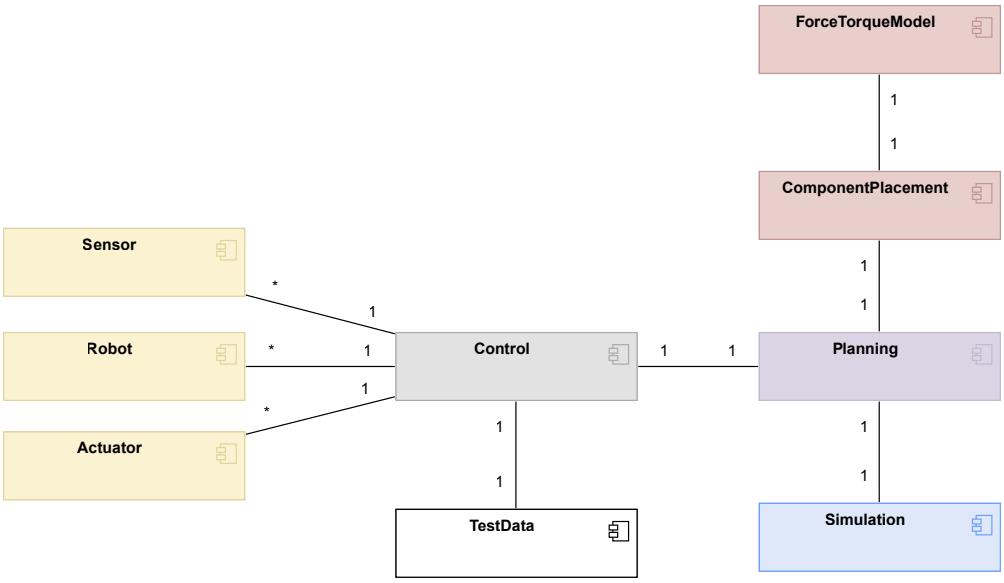

Figure 5.2. Overview of the main robot-based test bench components.

Robot

The robot components are in charge of handling all tasks associated with specific robot devices. This includes direct communication with the devices to obtain motion commands, retrieve settings, and transmit robot data. Since robots play an elementary role in the concept, they have explicitly not been represented as actuators.

Actuator

The actuator components are tasked with managing all aspects related to particular actuator devices. This entails direct communication with the devices to fetch motion commands and settings or transmit data.

TestDataStorage

The test data storage is responsible for storing all data collected during a component test.

Simulation

The simulation contains an digital representation of the entire test system and is responsible for the planning and simulation of the test process.

ComponentPlacement

The component-placement component is responsible for the automatic feasibility check to evaluate test motions depending on the required forces and torques, as well as for the constraint-based automatic component placement.

Force Torque Model Component
The force-torque model represents the stored values of the calculated force-torque model of the robot.

5.2.2 Global Data Flow Model

Figure 5.3 provides a visual representation of data flow and the interaction between different components, devices and the user involved in whole the testing process:

User
The user provides the test details to the planning process as an external entity. This includes the information about the component as well as the information about the motions.

Planning Process
The planning process receives the user test data from the user. It provides the component details and test motion details to the component placement process and receives information about the resulting component position from it. This information is forwarded together with the test motion descriptions to the simulation process. Afterwards, it receives from the simulation process the actual approach and departure motion points, which are then forwarded to the control process. Finally, it provides the calculated component position for actual clamping on the clamping field to the user.

Component Placement Process
The Component placement process receives the motion description and the component details from the planning component and calculates the component position, which is first provided to the planning component to be further processed by the simulation process.

Force Torque Model
The force-torque model data sink stores and provides the pre-calculated data for the robot's forces and torques depending on the infector orientation of the robot.

Control Process
The control process receives all the motion information from the planning component to control the test process. Therefore it sends motion descriptions for the position based motions to the robot and the actuators. Furthermore, it sends pose correction information to the robot for the actual sensor guided testing motions and receives the motion updates from all robots, sensors and actuators. This will be more explained in more Detail in Section 8.4.

TestDataStorage
The force-torque model data sink stores all the measured and aggregated test data from

the control process.

Sensor Entity
The sensor entity represents, for example, the ATOS 5 camera or the force-torque sensor and makes its sensor data available accordingly.

Robot Entity
The robot entity represents, for example, the KUKA Titan robot and provides its pose to the control process.

Actuator Entity
The actuator entity represents, for example, the Zwick EZ100 linear actuator and provides its position to the control process.

After this chapter has provided a basic overview of the test procedure, the architectural concepts, and the flow of information, the following chapters will go into more detail about the individual components and processes and their details.

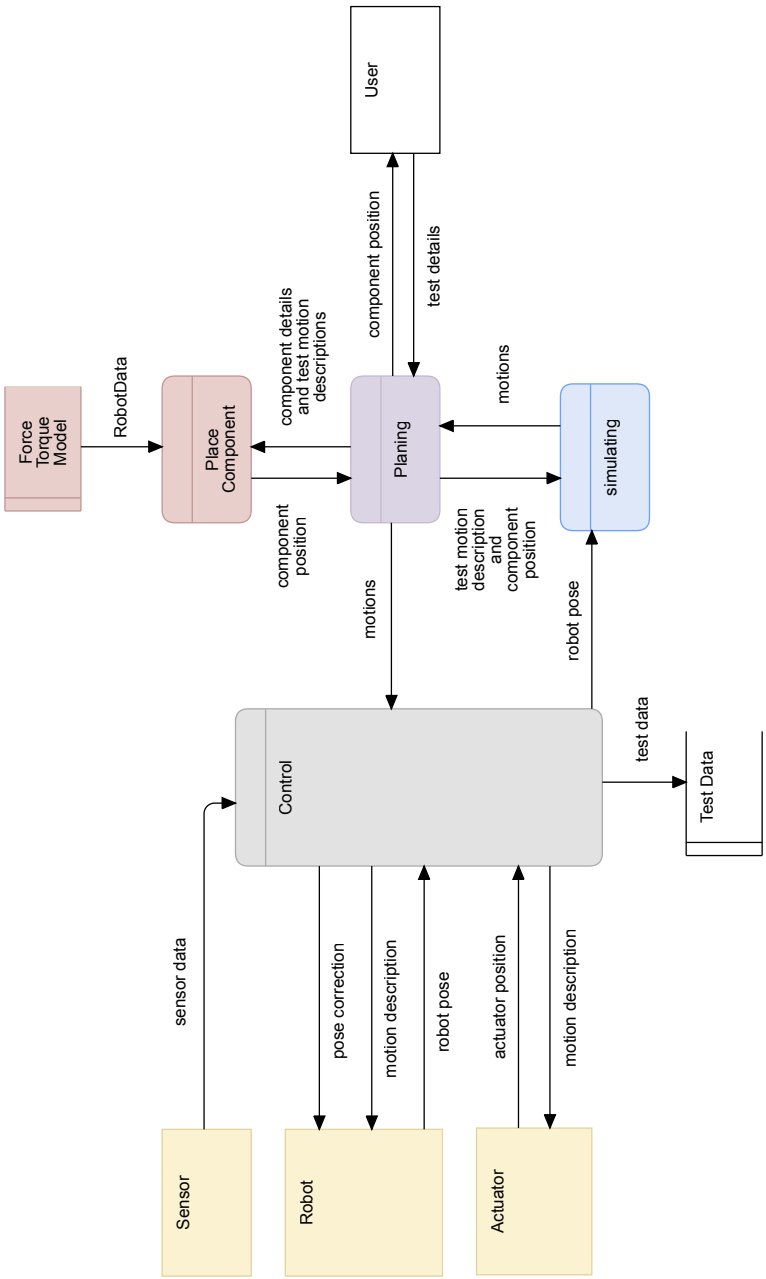

Figure 5.3. Representation of data flow and the interaction between different components, devices and the user involved in the testing process.

Summary. This chapter presents an modeling framework for robot-based component test motions. This framework encompasses the modeling of approach motions, which involve reaching the component, the testing motions themselves, and the departure motions that relocate the system away from the tested component. Furthermore, the modeling concept for orchestrating the sequence of these various types of motions is elucidated. The chapter concludes with an exploration of the existing state of the field and relevant research endeavors.

6

Robot-based Testing Motions

In the context of batch size one manufacturing, where products are tailored to individual customer preferences, the significance of component testing is heightened. Every constituent part necessitates comprehensive examination to ascertain its alignment with precise specifications, thus precluding defects and imperfections in the eventual product. Conventional test benches typically encompass rudimentary testing motions tailored to the examination needs of singular components. Hence, the demand arises for a pliable test platform accommodating various components featuring diverse testing motions. This adaptability can be achieved by leveraging software to transform a multi-capable robotic system into an adaptable testing apparatus.

The intricacy of testing scenarios, encompassing multiple motions and their precise sequences, necessitates a methodical approach. In this regard, Section 6.1 introduces a modeling framework for motions utilized in robot-based component testing. Expanding on this modeling paradigm, Section 6.2 delves into an approach for structuring the execution sequence of these motions. Lastly, Section 6.3 provides an overview of pre-existing or analogous concepts relating to motion depiction and the description of motion sequences in analogous contexts. These concept were partly published in [54, 55].

6.1 Modeling of Motions

6.1.1 Motion Overview

Essentially, three categories of motions are presented for robots or supplementary actuators such as linear actuators. An outline of these three types—approach, testing, and departure motions—and their further breakdown is illustrated in Figure 6.1.

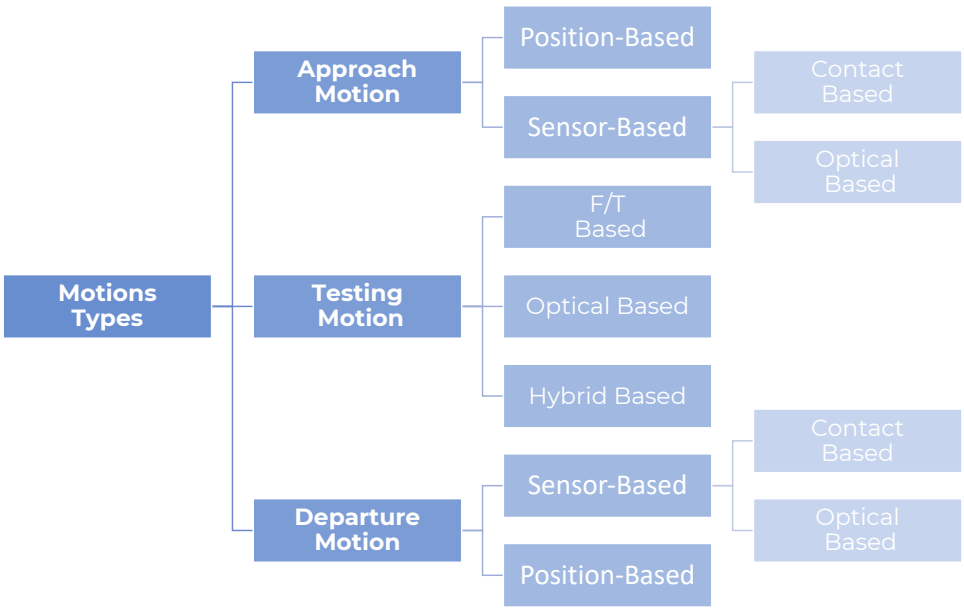

Figure 6.1. Three basic types of motions for robot-based component testing.

Approach Motions
Approach motions are responsible for the actual approach to the components. These can again be divided into position-based and sensor-based approach motions. Position-based approach motions are responsible for the collision-free approach of the robot end-effector to the components. This can be accomplished using the robot's internal positioning system. This is followed by a sensor-based approach to the components in two different ways. The end-effector is moved to the desired loading point with an external optical controller within the optical-based approach motion. In contrast, in a contact-based approach motion, the end-effector's position is controlled using force or torque feedback. Of course, the end-effector can also first be positioned based on its internal system , and then the approach can be continued based on the sensor-based method.

Testing Motions
Testing motions are responsible for conducting the actual testing motions and are classified into three distinct types, determined by the regulation mode used for the motion. F/T-based testing motions are regulated using a force-torque controller, while

optical-based testing motions are regulated based on position. The hybrid-based motions combine the first two types, incorporating force-torque and position regulation methods.

Departure Motions
Departure motions slowly unload the component, which was loaded by test motions performed before. Therefore, a precise (sensor-based) unload can be regulated using a force-torque or position-based controller. This is necessary, for example, if the components are still under tension. The position-based unload is responsible for the collision-free departure of the robot end-effector even farther away from the component if, for example, not so much accuracy is required or the components are no longer under tension. Additionally, this motion can automatically position the robot at a predefined point with the internal control system, such as the starting point. The following subsections will discuss the individual motions in more detail.

6.1.2 Approach Motions

Approach motions position the robot's end-effector toward the components. They can be further categorized into position-based and sensor-based approach motions. Position-based approach motions oversee the collision-free approach of the robot's end-effector to the components using the robots internal control system. Sensor-based approach motions are carried out in two distinct manners when approaching components and offer several possibilities to place and align the end-effector more precisely based on the component position. In the case of optical-based approach motions, the end-effector

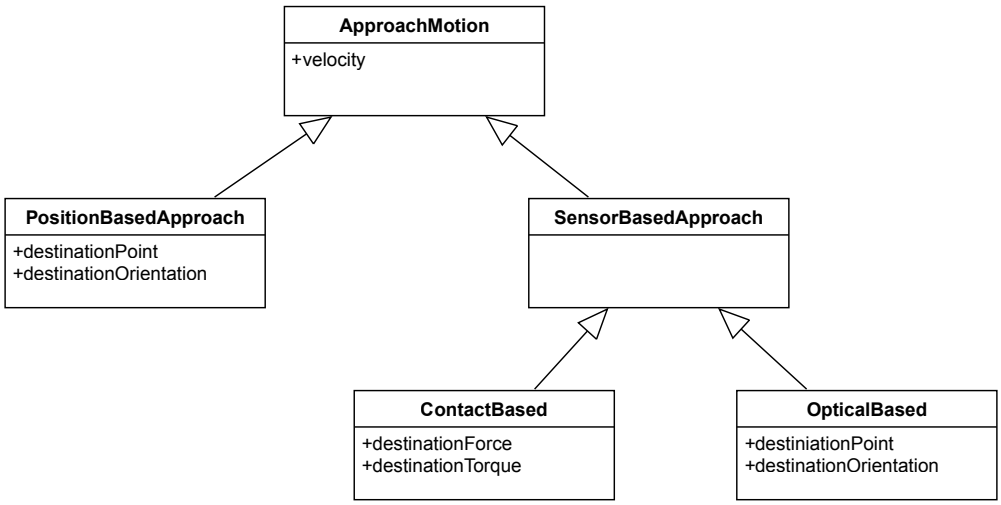

Figure 6.2. Approach motions in robot-based component testing are categorized into two fundamental types. The key differentiation between these subcategories is the control method applied to the approach motions. Position-based approach motions are regulated based on the internal robot position system, while sensor-based approach motions are regulated through sensor input.

is directed to the desired loading point using an external optical controller. An external position measuring systems, such as 3D cameras, can accomplish this. Conversely, contact-based approach motions involve positioning the end-effector through force or torque control. Alternatively, the end-effector's initial position can be determined based on location, and the subsequent approach can be executed using a sensor-based method.

6.1.3 Testing Motions

Testing motions define the actual test motions performed by the actuators, e.g., the robots. Their structure is shown in Figure 6.3. A testing motion consists of one or more *LoadPaths*. This enables the definition of superimposed load paths (e.g., force and torque simultaneous) and classic load paths (e.g., only a force). A linear testing motion example would involve testing a tensile specimen in a single direction using one load path, similar to the scenario described in case study one. On the other hand, case study three, which involves testing a snowboard, requires two load paths combined in a superimposed manner, involving both torsion and bending load paths. A load path can either be a *PrimitiveLoadPath* or an ordered composition of primitive load paths named *ComplexLoadPath*. A load path is defined by its velocity and its rotational speed if it is a circular motion. In addition, the optional starting point must be specified for the first load path of a test motion. Each testing motion starts at a specific starting point for the robot or actuator. Components or specimens are usually installed in clamping fixtures for testing. These clamping devices usually specify the height z of the starting point for the load path and the robot's orientation with z as the robot's impact direction. The robot starting point's missing cartesian position x, y must be calculated. Since the forces a robot can apply are highly dependent on its pose, an appropriate choice of x, y can be critical for the feasibility of a testing motion. This will be further discussed in the next chapter. Furthermore, the type of the load path must be defined (force/torque, optical or hybrid based). The direction of the load path is given by an *Orientation* a, b, c in a known coordinate system, e.g., in the case of f/t-based motion, in the base coordinate system of the f/t-sensor mounted on the robots flange. Of course, any coordinate system can be selected by a coordinate system transformation. In addition, a load path is also defined by its respective *TerminationCriteria*. These criteria are crucial for determining whether a test motion is considered complete and if the entire test can conclude or if the following test motion can proceed. Each load path includes one or more *TerminationCriteriaSet* to enable flexibility in terminating the load paths. These sets include one or more termination criteria. In this way, different termination criteria can be combined arbitrarily. All termination conditions within a set must be fulfilled simultaneously (conjunctive operator) for the set to be fulfilled. Termination criteria sets are linked disjunctive, meaning that the load path terminates once one of its termination criteria sets is fulfilled. A force criterion, e.g., can be combined within a set with a time criterion to specify how long the force should be applied. These five criteria have been identified: maxForce, maxTorque, maxTime, maxDistance, and Fracture. The first four are simple abort criteria represented by only a value or vector, i.e., the maximum force in kN in a specific direction. The lengths of the load paths can be defined in the

Loadpath

Primitive Loadpath

Complex Loadpath

Orientation

Termination Criteria

Termination CriteriaSet

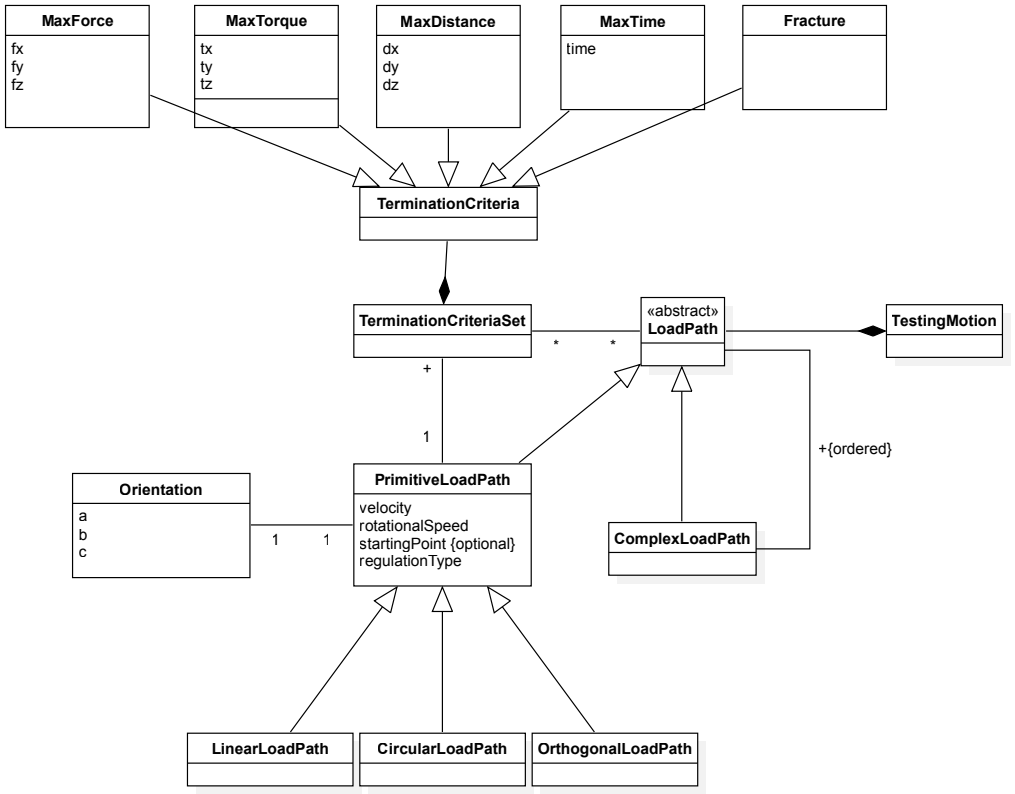

Figure 6.3. Representation of testing motions. Each testing motion is a composition of one or more load paths that include one or more termination criteria, which define, e.g., the range of motion or the maximum forces and torques to be applied to the component. Each test motion starts at a particular starting point for the robot with a predefined orientation a, b, c and a velocity or rotational speed. Furthermore, each load path has its regulationType which defines the type of the sensor-based motion. In the lower part a subset of common load paths is given.

respective direction. These can be determined in advance with the help of an FEM simulation. Moreover, it is critical to detect component failure, such as breakage. In the event of a failure, the robot may continue to move rapidly in the specified test direction, posing a safety risk due to its high energy potential. A significant load drop concerning the preceding maximum load defines the Fracture. A break is suspected at a drop of a defined percentage, usually 20%, and the criterion is met. The lower part of Figure 6.3 displays a subset of pre-configured motions commonly utilized in robot-based material testing. This obviates the need to assemble a new motion each time; instead, only the designated variables need assignment. A *LinearLoadPath* denotes a unidirectional linear motion, such as simple tensile testing. A *CircularLoadPath* signifies circular motion with an added rotational velocity accompanying linear motion. An *OrthogonalLoadPath* corresponds to scenarios like case study 3 (snowboard), where the testing motion on a deforming component should always maintain orthogonality.

6.1.4 Departure Motions

Once all test motions are concluded, the departure motions are initiated. These motions gradually unload the component, which was subjected to loading during preceding test motions. The primary differentiation between the two subcategories, position-based and sensor-based, pertains to the control method applied for the departure motion (see Figure 6.4). A target point and orientation mark the position-controlled departure motion. It is executed using the robot's internal positioning system, maintaining collision-free motion through simulation—an aspect detailed in the implementation section. The component can be gradually relieved in a designated force or torque direction in contact-based departure motions. This approach prevents further forces or torques from acting on the component during unloading. Similarly, optical departure motions can be employed to avoid unwanted movements in a particular direction. In many instances, a sensor-guided departure initiates to disengage or unload the component initially, followed by a position-based motion to further distance from the component.

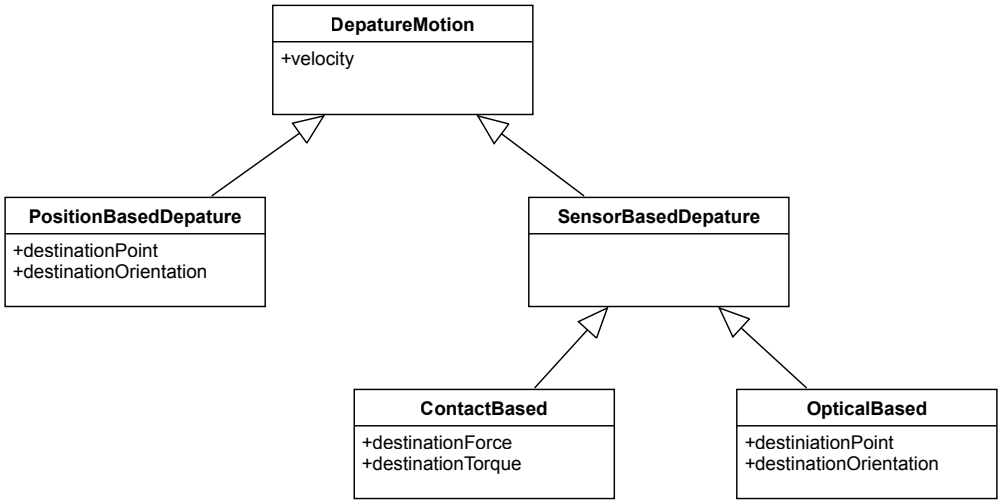

Figure 6.4. Departure motions in robot-based component testing encompass two fundamental types. The critical distinction between these subcategories lies in the control approach adopted for the departure motions. Position-based departure motions are governed by position-based regulation controlled based on the internal robot position system, while sensor-based departure motions operate under sensor regulation.

6.2 Modeling of Motion Sequences

To determine the order and execution of test motions, it's crucial to establish a modeling approach, which was developed using the syntax of UML state machines. This modeling technique represents individual motions as sequential states, where regions can be employed to differentiate between multiple devices and depict concurrent motions. The actual motion execution is then implemented as a do action of the respective

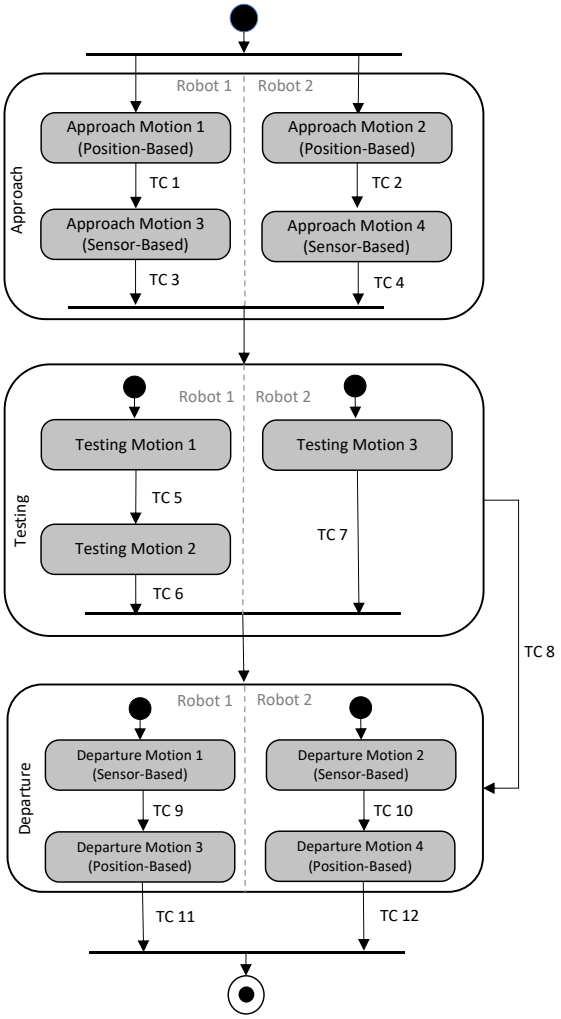

Figure 6.5. The state machine for the description of an exemplary motion execution sequence. The sequence for both robots starts with two approach motions, followed by the test motions, and ends with the departure motions.

state. Termination criteria based on interruptions can be modeled as triggers within this framework. For illustrative purposes, consider the example depicted in Figure 6.5, which involves two robots, one in the left swim lane (robot 1) and the other in the right (robot 2). The process includes three different testing motions, as well as two approach and two departure motions for each robot. Initially, both robots perform their approach motions with respective termination criteria (TC). The first and second approach motions manage imprecise approaches for both robots in a position-controlled manner, typically using the robot's internal control system. Here, the termination criteria 1 and 2 correspond to the desired destination position and orientation. Next, a more precise, sensor-based approach to the component takes place, which can be

force/torque (f/t)-controlled. The subsequent abort criteria (3, 4) relate to the forces to be achieved during this phase. The approach of the two robots can be parallelized by introducing an additional synchronization point before approach motions 3 and 4, as shown during the transition to the testing motions. The subsequent test motions begin as soon as both robots complete their approach motions. Robot 1 performs two test motions, while robot 2 executes only one. Similar to the approach motions, the transition between individual states is controlled by termination criteria, acting as interrupt-based triggers. For instance, termination criterion 5 could signify the attainment of a specific force during testing. Additionally, an overarching abort criterion can be introduced for testing motions to initiate the departure motion immediately (TC 8), for instance, in the event of an early component failure. Following the completion of their testing motions, both robots commence their first departure motion. If no failure occurs, this departure could be a sensor-based process, allowing for the gradual unloading of the component. The sequence concludes once both position-based departure motion termination criteria (TC 11, TC 12) are met.

6.3 Related Work

Various stakeholders have developed various software platforms, including non-robot manufacturers, academic researchers, and even robot manufacturers. These platforms aim to facilitate the programming of complex robot tasks or motions [108]. This methodology, known as Offline Programming (OLP), hinges on utilizing 3D virtual representations encompassing the entire robot work cell, the robot's end-effector, and the objects intended for manipulation or processing. Diverse categories of CAD-based offline programming methods have been proposed to address various tasks. One approach involves adopting existing commercial offline programming software or platforms from industrial robotics manufacturers (e.g., ABB RobotStudio [12] and KUKA.Sim [83]) and industrial software companies (e.g., DELMIA Robotics [37]). By importing the CAD model of the workpiece into these tools, robot programs can be manually generated using standard robot motions. Another type of CAD-based offline programming relies on utilizing available commercial CAD packages [102] or developing dedicated offline programming platforms to extract geometric data from the workpiece's CAD model and subsequently converting it into robot motion commands automatically [131]. This method finds application in fields such as non-destructive testing (NDT) with industrial robots, as demonstrated by the work of Mineo et al. [98], who created a MATLAB-based path-planning application for NDT of composite aerospace parts. The application, called RoboNDT, automatically generates tool paths for the robot based on the CAD model of the tested component. The RoboNDT application establishes a two-way connection with the robot, enabling the transmission of command coordinates for controlling the robot's tool path and the reception of positional feedback from the robot. This facilitates the incorporation of sensor data for real-time monitoring of position errors and potential adjustments to the path. However, this functionality has not yet been implemented and is not integrated into the description language of automatically generated robot motions. In addition to CAD-based approaches, vision-based methods are also employed. Vision-based offline programming employs various vision sensors to capture

geometric attributes of workpieces and create programming instructions [18]. Some approaches combine CAD-based and vision-based methodologies, known as hybrid approaches [137].

In present-day industrial robotics applications, the prevailing norm involves the adoption of proprietary robot controllers, each characterized by its unique methodology for delineating robot movements and integrating external sensors. The quintessential feature of such closed system architectures is their limited capacity and adaptability. As a result, this approach has become standard practice in scenarios marked by high-volume production, where the application is meticulously defined and anticipated to remain static over prolonged durations. To augment the flexibility of these systems, numerous manufacturers presently provide supplementary modules that empower industrial robots to respond sensitively to forces and torques exerted on the robot tool. One example is the force torque technology package from the manufacturer KUKA [81]. The provided technology package offers dual functional capabilities. Firstly, there is the sensor-guided motion: In this mode, the robot does not follow a predefined endpoint; instead, it initiates movement from a specified starting point determined by the acquired sensor data. The robot continues its motion until a predetermined termination condition is satisfied. The second capability is superposed force/torque control: The robot adheres to a predetermined trajectory while applying the specified force and torque set points during traversal of this trajectory. Similar functionality extensions are also available from manufacturers like Mitsubishi or ABB [11, 99]. Nonetheless, the aforementioned motion description and force torque extension control systems exhibit the limitation of being unable to integrate with another measuring method and are solely compatible with the respective robot manufacturer. Furthermore, the integration of additional sensors into a robotic system necessitates the expertise of robotics specialists and is frequently customized for specific applications. Consequently, various research approaches aim to provide a generalized sensor integration into robot motion control by extending built-in robot commands with specific sensor-based commands [13, 84]. For instance, Kus et al. [84], within the EU Project ARFLEX (Adaptive Robots for Flexible Manufacturing Systems), devised a comprehensive standard design for sensor integration. This concept allows real-time external control over the robot's trajectory using sensor-specific commands. They established a standard sensor interface enabling the incorporation of diverse sensors to influence standard robot motions. However, this interface does not integrate with all robot manufacturers and only robots and no other actuators, e.g. linear actuators, can be integrated.

In summary, the concepts that have existed for representing motion and describing motion sequences are not sufficient for robot-based component testing.

Summary. This chapter provides an overview of the developed computer aided specimen placement (CASP) approach for robot-based component testing. This includes a mapping data format for applicable forces and torques of different poses for industrial robots, an automatic feasibility check to evaluate testing motions depending on the required forces and torques, and a constraint-based automatic specimen placement algorithm. Finally, the last section gives an overview of the current state of the art.

7

Computer aided specimen placement

The manufacturing industry is undergoing a significant transformation in the context of Industry 4.0, and production is shifting from mass products to individual products of batch size one. Moreover, the increasing complexity of components, e.g., due to individual products, makes the testing setups of components even more complex. Due to the low quantities of the components, it is not profitable to build test benches for each component to test many different forces and torsions to ensure the needed product quality. In order to be able to test various components flexibly through different motions, an overall concept to perform robot-based destructive component testing was described in Section 5.1. This concept includes placing the component to be tested so that a six-axis industrial robot can apply forces and torques to it by performing complex test motions. On the one hand, the flexibility of the robots enables the execution of such test scenarios. On the other hand, it also creates new challenges.

Since industrial robots cannot apply the same forces and torques in all axis positions, a position must be calculated where the specimen can be tested. Therefore this chapter presents the approach for an automatic computer aided specimen placement (CASP) [56]. The first section explains the calculation model as the basis for the following sections. Section 7.2 introduces a mapping data format for applicable forces and torques of different poses for industrial robots. The automatic feasibility check to evaluate test motions depending on the required forces and torques and the constraint-based automatic specimen placement approach will be outlined in Section 7.3. Finally, Section 7.4 gives an overview of existing concepts for component placement in similar domains.

7.1 Calculation of Static Force Analysis Model

The utilization of industrial robots in component testing introduces complexities in the process of positioning the test object. Careful consideration of the object's reachability is crucial when placing it for testing purposes. While robots offer more flexibility compared to linear actuators, not every position on the clamping surface may be reachable. Additionally, even if a position is within reach, it may not be optimal for achieving the maximum force, especially when the robot arm is fully extended.

To determine the optimal starting pose for the robot, a suitable model was developed. This model analyzes the static force using the robot's Jacobian matrix to estimate the maximum forces that can be applied. The static calculations establish a relationship between the forces generated by the end effector and the torques applied to the joints. This assumes that the robot is in an equilibrium configuration suitable for component testing. Let γ_e represent the vector of generalized end-effector forces, with $\gamma_e = \left[f_e^T, \quad \mu_e^T\right]^T$. Here, f_e denotes the 3-dimensional force components, and μ_e represents the 3-dimensional torque components. According to [120], the relationship between the end-effector forces γ_e and the vector τ of joint torques is determined by the transpose of the geometric Jacobian J, which depends on the manipulator's joint configuration q.

$$\tau = J^T(q)\gamma_e \tag{7.1}$$

As a result, the maximum force for component testing at the end-effector, denoted as γ_e^{max}, can be determined by leveraging the inverse transpose of the geometric Jacobian J in combination with the existing joint torques. To obtain the available joint torques, reference is made to the joint space dynamic model of the end-effector as described in [120]:

$$B(q)\ddot{q} + C(q,\dot{q})\dot{q} + g(q) = \tau - J^T(q)\gamma_e \tag{7.2}$$

The matrix $B(q)$ is a symmetric and positive-definite 6×6 matrix that represents the joint space inertia. $C(q,\dot{q})$ is a 6×6 matrix such that the product $C(q,\dot{q})\dot{q}$ accounts for the Coriolis and centrifugal terms. The vector $g(q)$ corresponds to the terms related to gravity. Since component testing is carried out with extremely low velocities and accelerations (e.g., 10 mm/min for the chosen aluminum specimen in the scenario defined in Section 3.1.2), it is reasonable to assume that both $\dot{q}$ and $\ddot{q}$ are equal to 0. Consequently, the joint space dynamic model can be simplified, leading to a revised form of the equation 7.2:

$$J^T(q)\gamma_e = \tau - g(q) \tag{7.3}$$

To calculate the highest possible end-effector forces denoted by γ_e^{max}, with a specified joint configuration q and a maximum joint torque τ^{max}, the following formula is used:

$$\gamma_e^{max} = \left(J(q)^T\right)^{-1}\left(\tau^{max} - g(q)\right) \tag{7.4}$$

In order to exclude singularity positions, a check of $det(J(q)) \neq 0$ was added to the model calculation. If a singularity were to occur, it would lead to ambiguous

solutions and incorrect values. Additionally, the influence of the gravity term on the maximum end-effector forces varies based on the specific robot pose; for instance, when exerting a downward force, the robot's weight adds to the end-effector forces. Equation (7.4) estimates the upper limit of attainable end-effector forces and torques. For actual dynamic calculations, such as in the case of the test bench in this study, the manufacturer's machine data can be employed. Specifically, the dynamics were computed using a built-in function from the KUKA.Load software [78].

7.2 Representation of the Force Torque Model

When searching for an appropriate position for the specimen, it's essential to determine the maximum forces and torques the robot can apply in that pose. Performing these calculations online for every potential position is computationally demanding and time-consuming, making it impractical. To address this challenge and reduce the computational burden, these values are precomputed offline for a set of uniformly distributed samples across the workspace, and the outcomes are stored in a database. During online operations, this database is utilized to approximate the values, significantly improving efficiency.

The force-torque model captures sampled end-effector poses and their corresponding maximum forces and torques attainable by the robot. Due to the non-unique nature of reaching the same Cartesian position through different joint configurations, the mapping from Cartesian poses to potential forces and torques relies on the specifics of the inverse kinematics solver used. As a result, the chosen joint positions required to achieve each end-effector pose are also logged. This implies that, for the majority of poses, multiple entries are stored, each representing a potential joint configuration along with its applicable forces/torques. Typically, a standard six-axis industrial manipulator has up to eight different solutions for inverse kinematics. However, storing all eight solutions per sample is impractical due to the limitations on data storage and efficient retrieval. It's essential to address the issue of multiple inverse kinematics solutions by carefully selecting and limiting the considered Cartesian poses and joint positions based on the specific application. In the case of the presented test bench in Section 4.2, the Cartesian poses are constrained to the space above the clamping area and joint positions are restricted to exclude *overhead* and *elbow-down* positions in most instances. This approach significantly reduces the number of joint positions to be stored. The precise bounds for selection depend on the particular application and the characteristics of the robot being used. In the context of the showcased testing facility, the Cartesian workspace has dimensions of $7 \times 3 \times 3\ m$. For joint axis 1, bounds were set at (200°), encompassing only the clamping area's side. No specific bounds were applied to the other joint axes.

Mathematically, the force-torque model is described by two functions. The set of all stored joint positions is referred as Q, and the set of all stored cartesian end-effectors poses as E. The function p maps a cartesian pose e to the set of joint positions that are stored in Q and bring the end-effector closest to e:

$$p(e) = \{q \in Q | \text{NN(e, E)} = \text{FK(q)}\} \tag{7.5}$$

In this context, NN(e, E) denotes the nearest neighbor to the Cartesian pose e found within the set E. The forward kinematics function, denoted as FK, computes the end effector pose for each of the provided joint positions q. As the function p relies on a nearest neighbor search, the result of $p(e)$ is never an empty set (under the assumption that both the poses in E and the joint positions in Q are non-empty and correspond to each other). However, it's important to note that $p(e)$ can indeed contain multiple joint positions.

The second function, $m(q)$, maps joint positions to the maximum forces and torques:

$$\begin{aligned} m(q) &= \left(f^+(q), f^-(q), t^+(q), t^-(q)\right) \\ f^+ &= (f_x^+, f_y^+, f_z^+), \quad f^- = (f_x^-, f_y^-, f_z^-) \\ t^+ &= (t_a^+, t_b^+, t_c^+), \qquad t^- = (t_a^-, t_b^-, t_c^-) \end{aligned} \tag{7.6}$$

The consideration of positive and negative forces (f^+ and f^-) and torques (t^+ and t^-) is done separately due to their potentially unequal magnitudes. For instance, the ability to push and pull may not be achievable with the same force magnitude. The indices x, y, z, a, b, c specify the corresponding direction of the force or torque in relation to the global base coordinate system.

In practice, the force-torque model data is stored in a relational database, facilitating efficient storage and retrieval (refer to Figure 7.1). As such, the function $m(q)$ can be effortlessly computed through a straightforward lookup operation, as the values of q are a direct outcome of the computation of $p(e)$, which is contained within the database. The calculation of $p(e)$ is somewhat more intricate due to the necessity for a nearest neighbor search. Nevertheless, this still corresponds to a relatively simple database query. The forward kinematics FK(q) are not directly computed but rather provided by the association of poses and joint positions within the database.

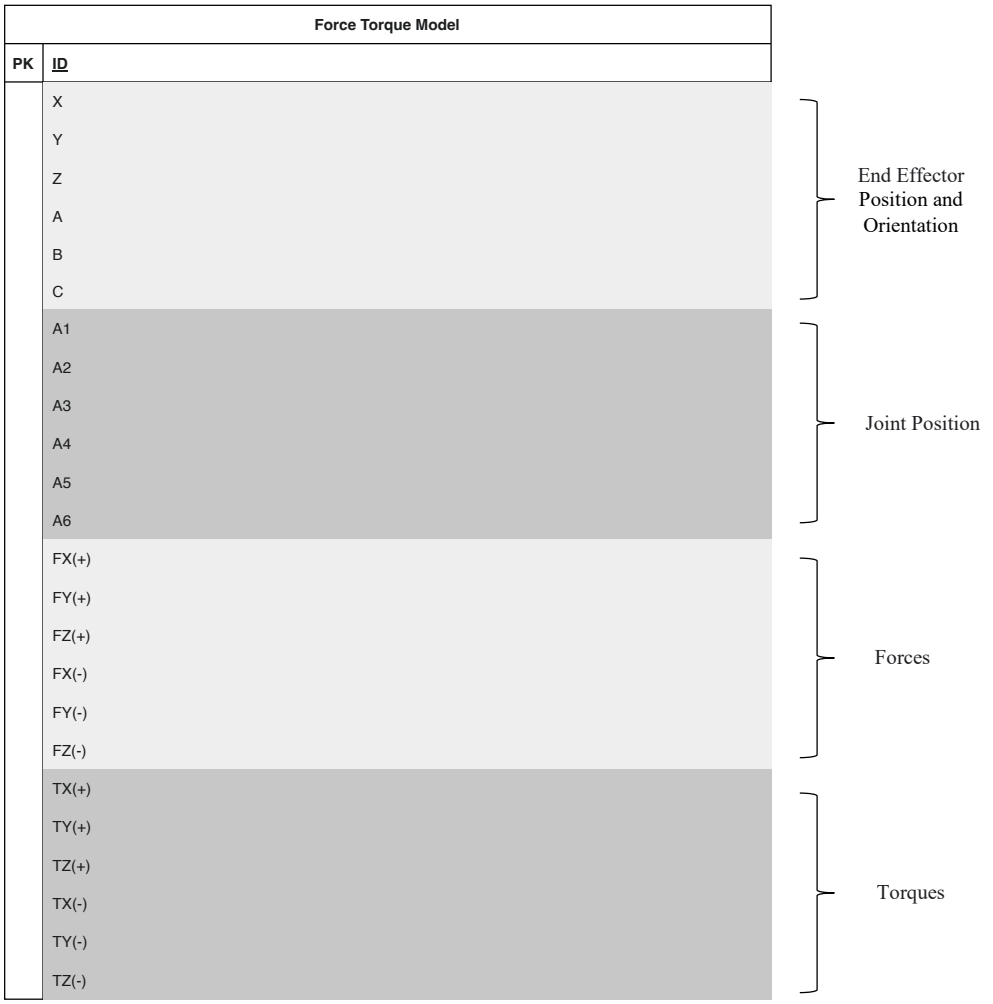

Figure 7.1. Representation of the Force Torque Model. The indices x, y, z, a, b, c indicate the respective direction of the force or torque relative to the global base coordinate system. $A1, to A6$ give the joint positions to the stored cartesian end-effectors poses. f^+, f^- and t^+, t^- represent the positive and negative forces and torques.

7.3 Specimen Placement and Feasibility Check

The primary objective of specimen placement is to identify a suitable position for the specimen under consideration for testing, guided by the specific testing motion and the robot's force-torque model. The orientation of the specimen, represented by (a, b, c), is determined by the testing motion's specifications. Additionally, the vertical position z is constrained by the physical limitations imposed by the clamping mechanism, leading to a single permissible value. Consequently, the procedure for specimen placement must determine both the robot's initial position (x, y, z) (with the z given above) and the ultimate placement point for the component.

In addition to determining the placement of the specimen, including the end-effector pose, it's crucial to identify the appropriate joint positions needed to reach this specific end-effector pose. This is essential because not all inverse kinematic solutions may be capable of generating the required forces and torques for the given task. Thus, the resulting joint positions vector, denoted as q, is an additional outcome of the algorithm.

The following pseudocode provides a fundamental outline of the procedure for identifying feasible pose to execute the predetermined testing motion.

$F \leftarrow feasibleStartingPoints(E, Q)$
for $(e, q) \in F$ **do**
  if $feasibilityCheck(e, q)$ **then**
    return (e, q)
  end if
end for

The procedure $feasibleStartingPoints(E, Q)$ returns all poses and the associated joint positions from the stored poses E and joint positions Q, where the robot can produce the forces and torques $(f_x,\ f_y,\ f_z,\ t_a,\ t_b,\ t_c)$ specified at the start of the testing motion:

$$\begin{aligned} f_x &\in [f_x^-, f_x^+], \quad f_y \in [f_y^-, f_y^+], \quad f_z \in [f_z^-, f_z^+] \\ t_a &\in [t_a^-, t_a^+], \quad t_b \in [t_b^-, t_b^+], \quad t_c \in [t_c^-, t_c^+] \end{aligned} \tag{7.7}$$

The values of f^+, f^-, t^+, and t^- are determined using the force-torque model as detailed in Section 7.2. The search for potential starting poses involves querying the force-torque model database with the desired orientation and height parameters (z, a, b, c). When the specification includes a range for z, an efficient range query can be utilized to retrieve all relevant entries within the specified range.

Through this approach, suitable specimen poses and corresponding joint positions for the initial phase of the testing motion are identified. However, ensuring that the robot can maintain sufficient force at the motion's outset is insufficient. This is because both the robot's position and the load path requirements can change as the testing motion progresses. Therefore, a feasibility check, referred to as $feasibilityCheck(e, q)$ in the above algorithm, is utilized throughout the entire testing motion to identify a feasible position. The $feasibilityCheck$ procedure incrementally evaluates the specified testing motion, examining the requirements at each step with a given step size. For a predicted pose along the testing motion, denoted as e_i, all joint positions from $p(e_i)$ are selected if they are in close proximity to the joint position of the preceding pose in the motion. The remaining joint positions are then examined using $m(q)$ to determine whether they meet the force and torque requirements of the testing motion.

If a starting pair (e, q) successfully passes the feasibility check for each testing motion, it is considered valid, and the procedure concludes. If, however, a feasible solution cannot be found, three fallback strategies are proposed to the user. These strategies, based on practical experience, often prove effective in locating a suitable solution. They typically

involve manual adjustments to specific aspects of the physical setup, usually focusing on modifying the clamping mechanism for the specimen. After making these adjustments, the specimen placement procedure is rerun with the updated parameters.

The three fallback strategies are as follows:

1. **Adjust height requirements:** Diverse methods of mounting the specimen can result in varying specifications for the parameter z, which denotes the necessary height of the specimen. Modifying this value generates new possibilities for positioning the specimen.
2. **Change orientation by right angles:** In real-world scenarios, owing to the design of common clamping mechanisms, adjusting the orientation of the specimen in multiples of 90 degrees is straightforward. This approach can offer a relatively uncomplicated method to identify a suitable set of parameters.
3. **Manual parameter adjustment:** The ultimate fallback strategy involves manually selecting a completely different orientation, such as opting for an alternative clamping fixture for the specimen.

In even the simplest component tests, there is often a need for extremely high forces or torques, which industrial robots cannot apply in every position. To assist users in identifying an appropriate orientation for the third fallback strategy, a visual aid is provided. This takes the form of a two-dimensional heatmap representing the force-torque model stored in the database, depicted for a selected orientation (a, b, c) and height (z) (see Figure 7.2). The heatmap is accompanied by a legend on the right side of the graphic, indicating the forces that the robot is capable of applying, measured in kN. The color scale ranges from 0 (dark purple) up to 35 kN (bright yellow). The force distribution generally forms a circular pattern centered around the robot, with greater force potential when the robot is less stretched. This indicates that axis 1 is not the limiting factor for this testing motion. The reduction in force along the longitudinal axis indicates the impact of axes 2 and 3. At the outermost circle, the force drops off sharply as the robot cannot reach those points, resulting in a force value of zero.

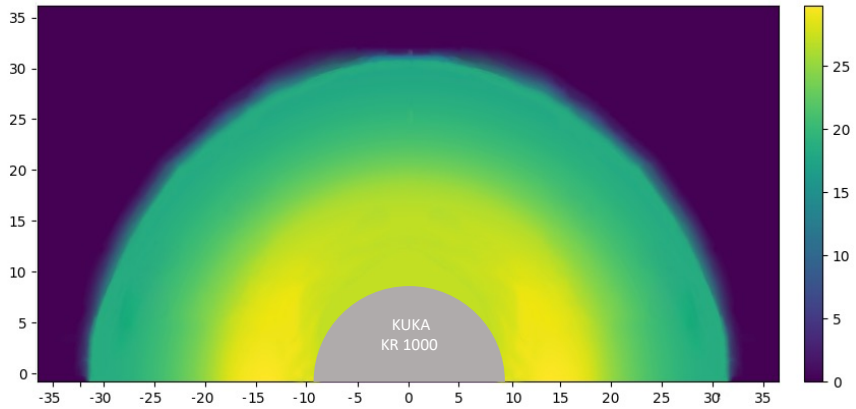

Figure 7.2. Visualization of a plane with the selected height $z = 130\ cm$ of applicable pulling forces in z-direction for the orientation of $a = -90°, b = 0°, c = 180°$ in robot world coordinates. The forces are given in kN, and the reach of the robot in the middle is given in dm.

7.4 Related Work

Different approaches have been investigated to increase the performance of industrial robots by finding the optimal workpiece placement for robot manipulation tasks or for material removal operations. The first solution for the object placement planning and optimization for robot manipulation task was proposed by Lozano-Perez et al. [94] in early times, and following, this problem has been extensively researched. Contributions in this area address three challenges according to Haustein et al. [58] or Harada et al. [57]:

1. To place a component, the object's physical properties and the environment must be considered.
2. The robot must be able to reach the component.
3. Human preferences, stability, and clearance from other obstacles must be determined.

These challenges are transferable to robot-based component testing, especially challenges 1 and 2, which play an essential role in automated component placement. Physical properties are given by the component itself or by the clamping fixture for the component. The environment is defined, e.g., by the clamping area where the component will be mounted. Moreover, the robot must not only reach the component but also apply the required forces and torques at this position, which is a further challenge to the above-mentioned challenges for robot manipulation tasks. Human preferences, stability, and clearance from other obstacles need to be considered, but in the domain of robot-based component testing, they play a subordinate role.

In the domain of material removal operations, a lot of research focuses on robot stiffness since it is the main cause of issues in robotic material removal operations and, thus, crucial to determine optimal workpiece placement. Lin et al. [92] defined an operational area within the robot's workspace using a kinematic performance index based on manipulability and considering the robot's stiffness properties. They validated this approach through a hole-drilling test, demonstrating that workpieces situated in the feasible region exhibit fewer deflections compared to those in non-feasible regions. Janez et al. [51], on the other hand, extended the optimization of robot configuration beyond stiffness to include manipulability, structural inertia, damping ratios, and natural frequencies. Liao et al. [90] introduced a methodology aimed at enhancing stiffness in 5-axis milling tasks by addressing an optimization problem that takes into account workpiece and end-effector orientation. They extended this approach to intricate workpieces that require significant adjustments in robot configuration during trajectory execution. To achieve this, they proposed a surface segmentation algorithm, ensuring that each segment adheres to a minimum stiffness threshold. In contrast, Gotlih et al. [6] employed a combination of a genetic algorithm and non-linear optimization to identify optimal deburring paths. Their approach utilized the genetic algorithm to determine the optimal object pose, maximizing robot stiffness throughout the deburring path, while the non-linear optimization guaranteed that the tool paths remained feasible and continuous. Caro et al. [29] presented a method to identify the optimal placement of a workpiece by formulating it as an optimization problem with the goal of minimizing end-effector deflections from the desired task-space poses. They computed these deflections using the Cartesian stiffness values of a KUKA robot. In addition, researchers have showcased alternative approaches that rely on factors beyond stiffness, including velocities, reachability, manipulability, and the limitations of robot joints. Malhan et al. [95] introduced an algorithm for workpiece placement, which guarantees the fulfillment of various constraints essential for the robotic operation. Following an assessment of the robot's workspace concerning reach and manipulability, a non-linear optimization technique was employed to determine a workpiece orientation with minimal violation cost. This metric relies on the pose errors resulting from specified tolerances for the TCP axes. In their work, Weingartshofer et al. [133] presented a specialized index for optimizing the placement of the robot base. This index comprises four components: the count of inverse kinematics solutions, the number of solutions that lead to continuous paths, the minimization of joint motion, and the distance from the joint limits. Xia et al. [136] produced a kinematic performance map utilizing a kinetostatic condition index, which served as a basis for optimizing robot configurations. The study also explored the correlation between the kinetostatic condition index along a tool path and the orientation of the object in the yaw axis. While the use of these alternative approaches has been shown to be viable in the literature, the problem remains that these approaches don't need to take into account that the robot should be able to execute the different partly aligned forces or torques over its whole movement radius. Since, in these approaches, the maximum forces and torques of the robots are not exceeded, this is also not taken into account in these approaches.

Filipenko et al. [47] introduced an initial solution to address the challenge of placing specimens for robot-based component testing. Their approach utilizes mixed reality, where a worker manually positions the component with the aid of an optical see-through head-mounted display, such as the Microsoft HoloLens. This system aims to simplify the setup process for new component tests by providing visual information about the robot, including a heat map indicating the maximum achievable force in selected positions. The utilization of Virtual Reality (VR)-based tools have been proposed for the setup of robotic assembly applications. These tools provide valuable support in various stages of work cell development, including layout planning, component positioning, and testing, as highlighted by Perez et al. [110]. However, these systems, on their own, do not fully address the fundamental challenges of precise component placement. To achieve dependable operation, they must be integrated with autonomous online trajectory and sequence planning. A primary factor contributing to this need is the inherent accuracy limitations of such devices.

Summary. A standardized testing procedure has been introduced to simplify the intricacies of robot-based destructive component testing and guarantee test reproducibility. This chapter presents the concepts for implementing the second phase of this procedure, the execution phase. This includes a flexible, control architecture for integrating all components and the implementation concepts for the actual motion execution.

8

Implementation of a software defined robot-based test bench

Conventional testing apparatus typically encompass rudimentary test procedures and test motions tailored to the examination needs of singular components. Hence, the demand arises for a pliable test platform accommodating various components, featuring diverse testing motions and a standardized test procedure. This adaptability can be achieved by leveraging software to transform a multi-capable robotic system into an adaptable testing apparatus. In order to simplify the complexity of robot-based destructive component testing and ensure test reproducibility, a standardized testing procedure was introduced in Section 5.1. This procedure defines the domain for a software-defined robot-based component test bench fundamentally and consists of three phases. The first phase, the preparation phase, defines the preparation of the test case. This includes the component analysis, the motion definitions, and measuring technique determination. It also includes the component placement and the test simulation. These preparations now serve as the basis for the next phase, the execution phase, where the actual component test is carried out. This chapter presents the concepts for the actual implementation of this execution phase.

First, the fundamentals necessary for this chapter are discussed in Section 8.1. In order to manage the second phase, a flexible and extensible control architecture concept was developed and is described in Section 8.2. This concept was first published in [55]. The

following sections (Section 8.3 and Section 8.4) delves deeper into this architecture, explaining the data aggregation and execution of the actual motions in more detail.

8.1 Fundamentals

8.1.1 Open Platform Communications Unified Architecture

A pivotal component within the devised architecture to manage the second phase is the adoption of the OPC UA (**O**pen **P**latform **C**ommuniations **U**nified **A**rchitecture) standard [60], recognized as a fundamental Industry 4.0 technology for facilitating connected manufacturing [41]. OPC UA is an interoperability standard independent of platforms and vendors, designed to facilitate data exchange within industrial automation systems. This standard encompasses numerous specifications collaboratively developed with contributions from industry and research entities. OPC UA transcends the realm of a mere data exchange standard; it comprises an extensive information model and services aimed at accessing and exchanging data among various information models, which might be locally accessible or distributed across different devices. The information model encompasses the core data, associated metadata and object-oriented links between the data elements.

OPC Unified Architecture

Figure 8.1 depicts the **system architecture** of OPC UA, released in 2008, which is grounded in two fundamental mechanisms for information exchange from the bottom to the upper section. The first is client-server communication, while the second involves publish-subscribe (Pub-Sub) communication. In terms of network transmission, multiple protocols can be selected based on the specific use case. Communication interfaces gain access to the data within the information model through an abstraction layer

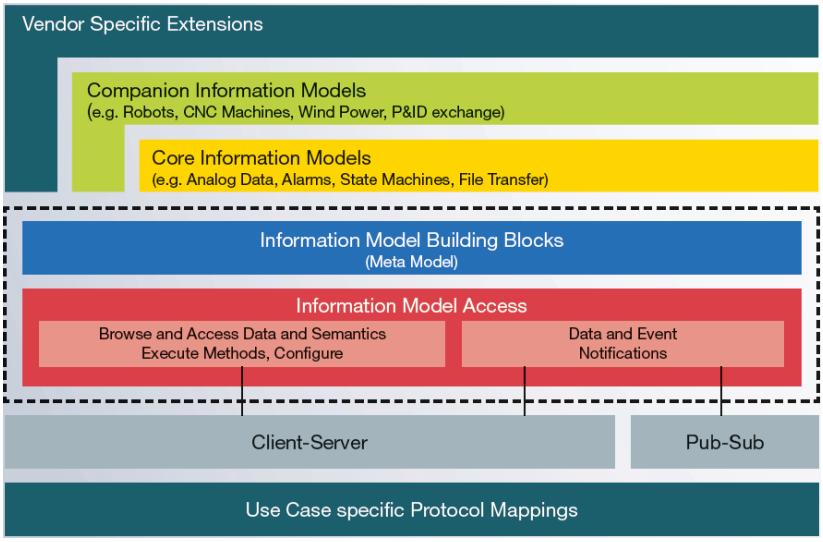

Figure 8.1. The OPC Unified Architecture is a platform-independent, service-oriented, and multi-layered architecture [106].

known as Information Model Access. In streamlining standardization efforts, predefined information model blocks are available, referred to as Information Model Building Blocks (Meta Model). Using this meta-model as a foundation, information can be stored within the model itself (Core Information Models). To ensure consistency of information models across various manufacturers and developers, companion specifications are introduced. These specifications standardize the structure of information models within specific domains, known as Companion Information Models. For instance, within the realm of robotics, a companion specification outlines the required information for a robot and prescribes the data structure in which it should be organized. Building upon these foundational information models, further vendor-specific data becomes feasible. [106]

OPC UA Information Model

The **OPC UA Information Model** employs the principles of Object-Oriented Programming (OOP) to represent information. Within this framework, OPC UA Nodes serve as the foundational representation for information and behaviors in the model. Nodes can embody various forms of information, such as variables, data types, methods, or events. These nodes can be interconnected through relationships, enabling the construction of complex information structures. Furthermore, OOP concepts such as inheritance, polymorphism, abstraction, and encapsulation can be harnessed. Each data element accessible in the information model is delineated as an OPC UA Object, inheriting from the OPC UA Node structure. These OPC UA Objects can encompass variables, methods, and events, accompanied by pertinent metadata such as data types or method parameters. This architecture permits the amalgamation of all automation system information within linked OPC UA Objects, which not only hold information but also offer executable methods. The communication interfaces enable access to objects within the information model and facilitate information synchronization across various distributed information models. [63].

OPC UA Client-Server

An OPC UA system utilizing the **client-server** communication method consists of OPC UA Servers and OPC UA Clients that engage in interaction. Multiple clients and servers can coexist within a system, and each server can connect with one or more clients. This bidirectional interaction applies to both clients and servers. When communication spans multiple servers, a component must function as a server and a client. Communication is enacted through exchanging service requests from the client to the server. The server processes the request and identifies the relevant service to be executed, ranging from essential data reading and writing to method invocations and even server reconfiguration. [62] These services access OPC UA objects within the information model and engage with them. Upon successful execution, the server sends an appropriate response to the client. However, client-server communication is not well-suited for dynamic data and many-to-many data exchange due to its request-based nature. Additionally, decoding requests and services introduce latency, which can be problematic for sensor-guided motion communication [30].

OPC UA Publish-Subscribe

The second communication method, the OPC UA **Publish-Subscribe** (PubSub) mechanism, offers a many-to-many communication approach and holds the advantage of not relying on request-based interactions. This feature is well-suited for scenarios with continuously changing data, such as sensor-guided motion. OPC UA PubSub leverages message-oriented middleware for communication. Various message-based middlewares

can be employed depending on the application's needs, including broker-based communication protocols like MQTT (Message Queueing Telemetry Transport) [105] or broker-less communications that use the transport medium as middleware, such as UDP multicast. After choosing the middleware, the process of PubSub involves two participants: OPC UA Publishers and OPC UA Subscribers, both of which are implemented as OPC UA Servers and possess distinct information models. OPC UA Publishers access their respective information models, package designated OPC UA Objects into messages, and then transmit these messages to the message-oriented middleware without the need to identify the recipients of these messages. An OPC UA Subscriber expresses interest in specific information, establishes a connection to the message-oriented middleware, retrieves the required data, unpacks the OPC UA Objects from the received messages, and then integrates these Objects into its information model. It is important, that the subscriber does not require knowledge about the publishers' identity. This characteristic of PubSub communication delivers scalability, allowing the easy addition of new publishers or subscribers to the system. Additionally, the cycle times for data transmissions can be adjusted to very high frequencies due to the asynchronous communication approach. [61]

OPC UA provides standardized interfaces and data models for various devices, sensors, and controllers. When implementing a control architecture, e.g., subsumption architecture, within an industrial system, having these standardized interfaces can simplify integration, making it easier to connect and manage different architecture components, including robots, sensors, and actuators. Therefore, the following section introduces the basics of a subsumption architecture.

8.1.2 Subsumption Architecture

The subsumption architecture is a reactive approach in robotics closely associated with behavior-based principles. Coined by Rodney Brooks and colleagues in 1986, this architectural framework has significantly impacted both autonomous robotics and real-time AI applications. Unlike the traditional approach, the subsumption approach to robot control opts for a hierarchy of layers, conceiving control as a set of competencies or behaviors, see e.g. Figure 8.2. In Figure 8.2, a basic illustration showcases a subsumption architecture applied to a robot collecting packets and transporting them to a designated destination. During its journey, the robot needs to navigate around obstacles in its surroundings. [128, 134]

The subsumption architecture consists of multiple subsumption layers, each containing progressively more intricate behaviors than the lower ones. Higher-layer behaviors can override or suppress lower-layer behaviors when necessary. The example consists of four layers, with the explore layer as the lowest and the avoid collisions layer as the highest. Constructed modularly, the architecture relies on individual modules representing distinct behaviors or tasks, e.g., the explore module. These modules are organized into layers, each representing a competency level. Operating asynchronously, modules can function concurrently, promoting swift responses to environmental shifts, e.g., if a collision occurs, the avoid collisions module can suppress the explore module.

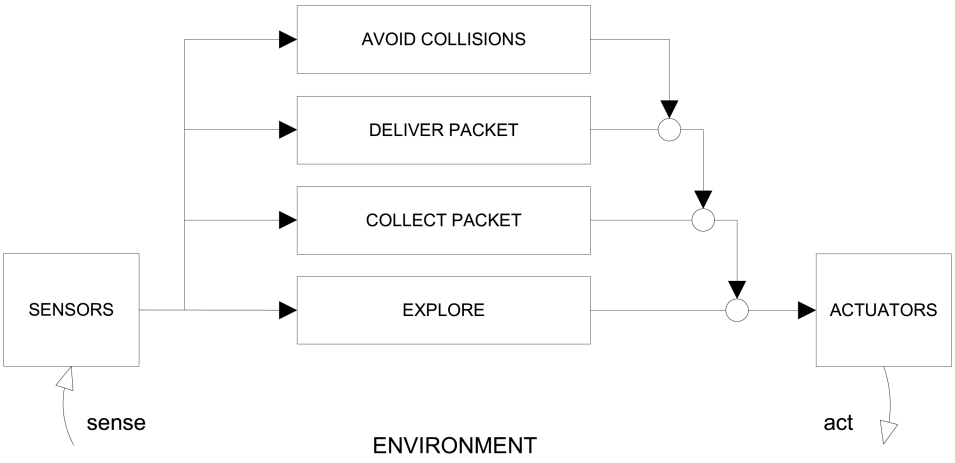

Figure 8.2. Subsumption architecture for a simple robot [134].

Communication between layers is facilitated by message-passing, allowing behavior coordination and information exchange. [128] This architectural approach has demonstrated its effectiveness through successful applications in numerous practical robotic systems [134].

Notably, the architecture prioritizes immediate responses to sensory input, enabling behaviors to react rapidly to environmental changes. The subsumption architecture's objective is to equip robots with the ability to exhibit sophisticated behaviors and adapt to various scenarios through layered control. [128]

In industrial robotics, where the operating environment is often more controlled than experimental mobile robots, this architecture can simplify the control problem due to the controlled environment and the careful design of robot interactions. Given the inherent flexibility and uncertainties in robotic environments, subsumption control can also be useful within industrial robotics. [128]

8.2 Architecture of the Execution Phase

To manage the execution phase, a higher-level architecture concept was devised, illustrated in Figure 8.3. This approach leverages the benefits of a client/server architecture, utilizing the PubSub mechanism for communication to fulfill specific requirements. This enables the addition of diverse devices to the existing infrastructure regardless of their manufacturers (RE 1 and RE 2). These devices only need integration into the main control component. This control component, responsible for overseeing the execution phase of the standardized test procedure, handles actuator control, data aggregation, and storage. It exists as its own OPC UA Client, connected to other components via Ethernet. Similarly, each sensor and actuator operates within its dedicated OPC UA Server, each with its information model. The control component aggregates these interfaces, per-

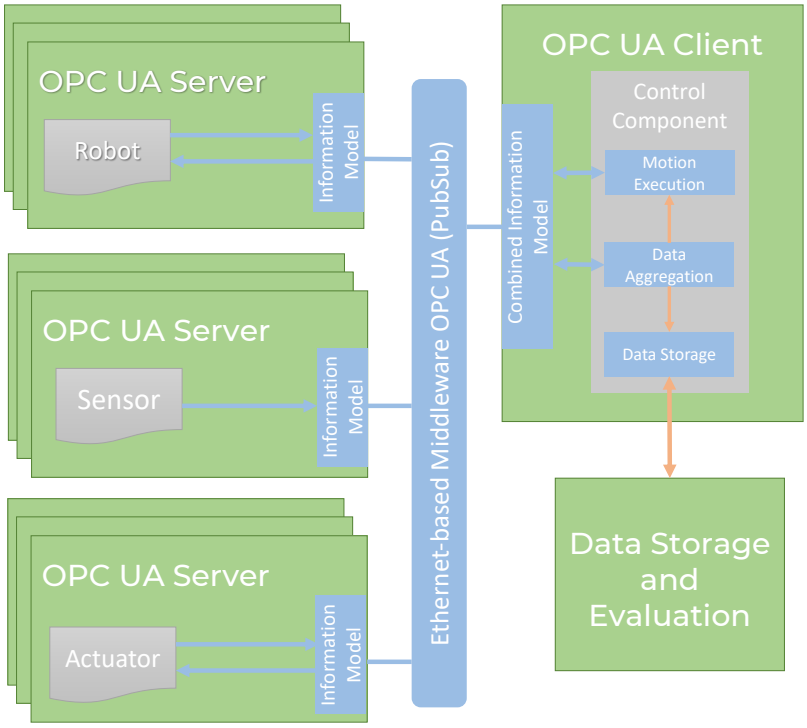

Figure 8.3. The architectural concept for the execution phase encompasses the main control component along with supplementary actuators, sensors, and data storage. Notably, robots are distinct from actuators within this framework. All these components are encapsulated as OPC UA Servers and communicate through an Ethernet-based middleware.

mitting easy expansion of the system with standardized mechanisms. Communication employs the Ethernet-based PubSub mechanism provided by OPC UA. This middleware allows the control component to subscribe to and process sensor and actuator data. It also permits publishing control commands subscribed to by robots or other actuators. Clock synchronization across distributed components is imperative for scheduled data transmission and aggregation. The Precision-Time-Protocol (PTP), defined by IEEE standard 1588 [8], is employed for this purpose. PTP designates one device as the master clock and others as slave devices, achieving synchronization through timing messages with timestamps exchanged via UDP multicast. The transmission time is determined by roundtrip time measurement, with slave clocks adjusted to master timestamps by accounting for transmission time. PTP accomplishes sub-microsecond synchronization between clocks. The control component assumes the role of the PTP master in this setup. Lastly, the control component interfaces with the data storage and evaluation component. This interface allows for the use of various storage and evaluation tools as needed.

8.3 Data Aggregation and Annotation

Within this architectural framework, a central control component takes the lead in overseeing the execution phase of the standardized test procedure, managing actuator control, and overseeing data collection and storage. The data aggregation component gathers and consolidates data from predefined sensors and actuators. Given that these sensors and actuators supply data at varying intervals, it is imperative to unify the data for subsequent processing by the motion execution component. Refer to 8.4 for a visual representation of the data aggregation process, using data from three distinct sources as an example. On the left side are the servers for the sensors and robots depicted. These servers publish their data to the middleware. On the right side is the client responsible for the data aggregation process, which subscribes to this data. All servers and clients employ the PTP-Time Protocol to synchronize their clocks with a designated master clock. Each server supplies different data with varying frequencies for data aggregation. The data from all these devices is consolidated through downsampling or linear interpolation using timestamps. Eventually, this aggregated data is transmitted to either the motion control component or the data storage converter. This data, once explained, will be employed for motion control in the subsequent phase.

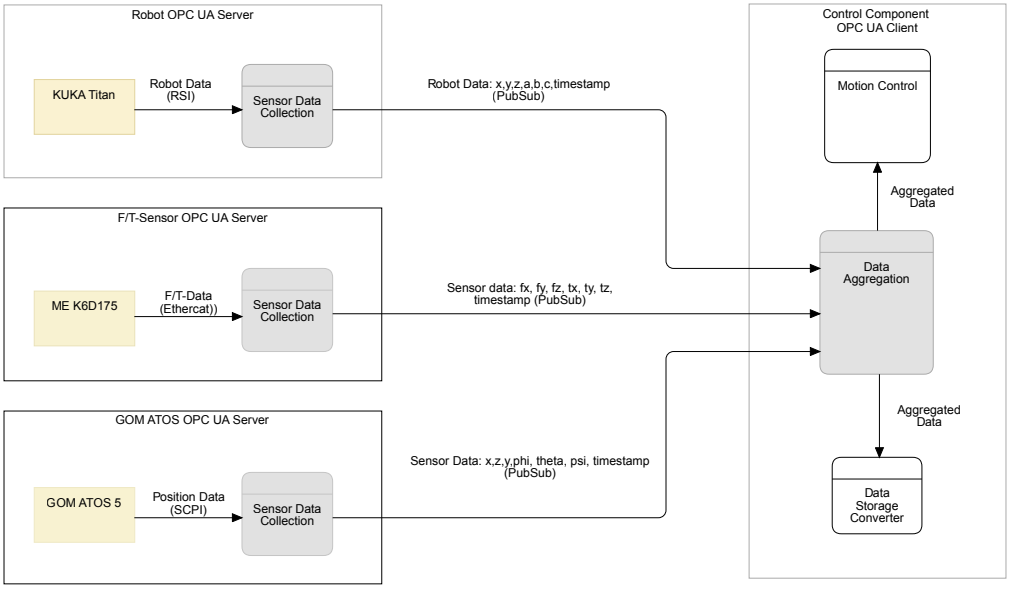

Figure 8.4. Overview of the existing sensor and actuator data and their data flow into the aggregation component using the example of two sensors and one actuator.

KUKA Titan Robot

The following data is obtained from the KUKA Titan robot:

- x, y and z: These values indicate the position of the robot.
  item a, b and c: These values indicate the rotation of the robots end-effector around its three coordinate axes.

- s, t value: The values of the position (x, y, z) and orientation (a, b, c) of the TCP are not sufficient to define the position of a robot unambiguously as mentioned in Section 2. Status and Turn are used to determine a unique pose.
- The data is sampled at a frequency of approximately 250 Hertz.

GOM ATOS 5 Stereoscopic Camera
The following data is obtained from the GOM ATOS 5:

- x, y and z: These values indicate the three-dimensional position of the target in space in coordinate system of the camera.
- phi, theta and psi value: These values are angular values that describe the orientation of the target in space in coordinate system of the camera. Phi stands for the rotation around the x-axis, theta for the rotation around the y-axis and psi for the rotation around the z-axis
- The data is sampled at a frequency of approximately 10-12 Hertz.

ME K6D175 F/T-Sensor
The following data is obtained from the ME K6D175:

- fx, fy and fz: These values indicate the three-dimensional force acting on the sensor.
- tx, tz and tz: These values indicate the three-dimensional torque that acts on the sensor.
- The data is sampled at a frequency of approximately 250 hertz.

8.4 Motion Control

Embedded in the control component is the motion execution component, which is also responsible for carrying out the various motions for component testing. It receives all motion information from the planning component (see Figure 5.3). Afterward, it transmits, depending on the motion type (approach motion, testing motion, departure motion), the motion data via the ethernet-based middleware, which is received from the OPCA UA server of the robot or the actuator. The OPC UA Server of the robot processes the motion information and sends it to the robot. Here it depends on the manufacturer of the robot and which interfaces of the robot are used. Both employed robots are KUKA industrial robots of the KR series and are equipped with the KRC4 (see Section 4.2.1), which maintains consistent interfaces for robot interaction. Traditionally, KUKA robots are programmed using a proprietary language called KUKA Robot Language (KRL) [77]. This language allows for executing motion commands, conducting calculations, querying integrated sensors, and controlling additional components like end effectors or linear axes. However, KRL is not well-suited for implementing intricate motion execution concepts. Consequently, efforts were directed toward using external interfaces provided by the robot controller.

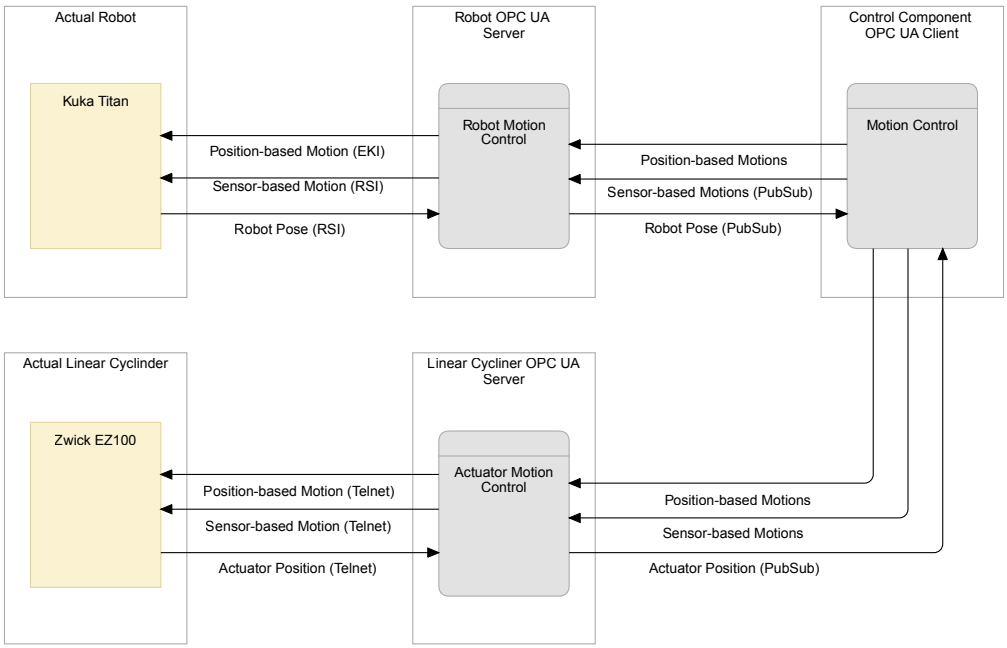

Figure 8.5. Overview of the execution of the motions and their different interfaces (given in brackets) between the control component, the robots and the linear cylinder.

KUKA offers two ethernet-based external interfaces for this purpose. The first interface is the Ethernet KRL Interface (EKI) [80], designed as an add-on technology to facilitate XML data exchange between the robot controller and external systems via the TCP/IP protocol. EKI is suited for transmitting lengthy, non-cyclical actions, such as sending motion commands or configuring reference coordinate systems. The second interface is the Robot Sensor Interface (RSI) [82], allowing real-time data transmission between the robot and external systems. RSI operates on a real-time processing cycle and can directly influence the robot's path using external system values within the same cycle. This interface also enables direct modification of the robot's path using values from an external system, all within a 4 ms cycle. The primary application of this interface is, for example, a force-controlled motion by an external force torque sensor. Figure 8.5 provides an overview of motion control. Here the control component uses different communication channels provided by the ethernet based middleware.

8.4.1 Position-based Motions

As described in Section 5.2.2, two types of position-based motions are used for robot-based component testing. Position-based approach and position-based departure motions. The control component communicates with the robot motion control component via the ethernet-based middleware. Since no cyclic data communication is needed for this motion type, it is done via client-server communication, not PubSub. There are two ways to reach a position with the end-effector. A robot pose (x,y,z,a,b,c,s,t) or

the axis position (a1,..., a6) can be transmitted. The motion controller of the control component uses both options. It transfers a robot pose to the robot motion controller if the end-effector pose is irrelevant. This can be used, for example, for a departure motion that is intended to move the end-effector further away from the components after a sensor-guided departure motion. The second option, the axis position transfer, is used if the end-effector pose is necessary. As mentioned in Section 6.3, identifying the appropriate joint positions needed to reach a specific end-effector pose is crucial. This is essential, because not all inverse kinematic solutions may generate the required forces and torques for the given task. For the execution of the position-based motions, the motion controller from the control component transmits via client-server communication the axis position or the pose. The robot motion controller accesses the robot in the next step via the EKI. The response if the motion was carried out has been omitted here for reasons of clarity. The motion execution process or the additional Zwick actuator is similar. The actuator motion control receives the actuator position also client-server-based via the ethernet-based middleware. The telnet interface is used to transmit the motion from the actuator motion controller to the Zwick EZ100. However, the motion information here consists only of a length indication of how far the actuator is to be extended. The response as to whether the motion was carried out is omitted for reasons of clarity here.

8.4.2 Sensor-based Motions

Sensor-based motions are used for all three motion types (approach motions, test motions, departure motions), where additional sensors are used to, e.g., increase the accuracy or achieve a particular force for the robot. Since cyclic data communication is needed for this motion type, it is done via the PubSub mechanism provided by the ethernet-based middleware for the robot. The robot is accessed via the RSI, the second interface described above. It enables cyclic real-time data transmission between the robot and the robot motion control. The robot's motion control can modify the robot's cyclic path. An overview of the control implementation of the motion execution, including the deviation correction, is given in Figure 8.6.

In order to perform the actual motion and to take into account the termination criteria at the same time, a subsumption architecture was used. The Data Aggregation Component provides the Sensor data to all needed layers. Within this architecture it is possible to add several layers, for example, to enable weighted motions or weight abort criteria differently (RE 1 and RE 2). In this example, three layers were chosen. The base layer represents the planned test motion, e.g., the linear motion upwards for a tensile test with a given velocity.

To execute a test motion in one or more specified directions at a given speed, a constant correction value in the respective direction is provided to the robot. This linear motion can be corrected by superimposed layers. In the test motion correction layer, a position correction (based on camera input) or force/torque correction (based on force/-torque sensor data) is implemented using a PID controller to minimize any deviations. Moreover, to reduce sensor measurement noise, various filtering mechanisms can be

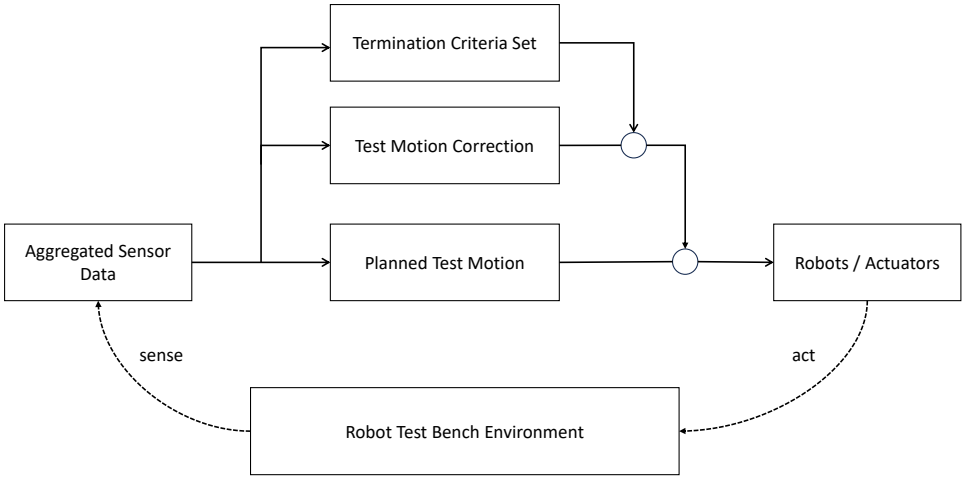

Figure 8.6. Three layer example of the control structure for the position controlled robot and the computation of the desired path or direction from measured values of the additional sensors.

integrated here. For the chosen case studies, a sliding average filter was applied to the last ten camera measurements. This architecture can easily accommodate other types of correction mechanisms as well. The motion and the correction are transmitted to the robot incrementally as a position correction through the RSI interface at a $4\,\mathrm{ms}$ cycle rate. Deviations are determined in each cycle using sensors (either a camera or force sensor) and are factored into the calculation for the next cycle. The environment includes factors like component deformation or robot deformation, which must be compensated for depending on the motion characteristics. Deviations are measured and corrected in the robot's base coordinate system for absolute position correction within optical-based motion types. This involves calculating the transformation from the camera system to the robot's coordinate system. For example, the GOM ATOS 5 camera uses the rotation convention $zx'y''$ specified in current frame. This allows the robot to operate in the camera's coordinate system and simultaneously provides calculations for translational and rotational deviations. Force-torque correction is measured and corrected in the robot's tool coordinate system. Transverse forces are converted into position corrections using a PID controller. For example, in case study one, transverse forces in the x/y-directions were minimized since the pulling motion was in the z-direction. Finally, if any of the termination criteria are met, this correction layer is overwritten as the motion ends, and the next motion can be initiated. An example of such a termination criterion would be a fracture occurring in the case of tensile specimens.

The linear cylinder from Zwick behaves differently from the two robots when executing the motions. It does not support cyclic connections but only motion commands mapped into a sensor-guided motion by the internal control system. Therefore it is not addressed via PubSub but via client-server from the motion control component to the actuator

control component. The actuator motion control process controls the movements via Telnet. Nevertheless, the introduced modeling format of the motions remains the same but is reduced to only one degree of freedom. This can also be either force-controlled or path controlled. The linear cylinder supports only three abort criteria: Break, maximum force, and maximum distance. The position data can be queried cyclically from the cylinder, accessed via Telnet and then forwarded via PubSub.

Summary. This chapter evaluates the approach outlined in this thesis by conducting four case studies to assess its technical feasibility and the advantages of software-defined test benches. To achieve this, the approach is applied to a conventional tensile specimen and three diverse components: a bicycle frame, a snowboard, and an automotive component. These components are subjected to testing on the robot-based component testing facility that has been implemented. This chapter meticulously records and analyzes the outcomes obtained from these tests.

9 Evaluation

In order to evaluate the results and application areas of the developed concepts for robot-based component testing, four case studies were selected and introduced in Chapter 3. Based on the presented challenges of the selected case studies, the hardware and software requirements for robot-based component testing were derived and summarized in Section 4.1. The developed concepts for a robot-based test bench to solve these requirements are described in the following chapters of this thesis. This concepts will now be evaluated in this chapter. The first section describes the evaluation of a classical tensile test. The following section (9.2) describes the testing of the chosen bicycle frame at different loading points, followed by the third case study in Section 9.3 for g the evaluation of complex testing motions on a snowboard. Subsequently, Section 9.4 presents the evaluation of the test of an automotive component to explain the need of multi-robot testing.

9.1 Case Study 1: Tensile Test

As outlined in Section 2.1, material testing encompasses a variety of methods utilized to evaluate the behavior and properties of standardized material samples (material analysis) or finished components (component testing) when subjected to mechanical, thermal, or chemical stress. This process involves examining factors such as material purity, absence of defects, and load-bearing capacity to assess the material's performance and suitability for specific applications. One standard method within destructive mechanical material testing is the tensile test, which provides information about material characteristics like ultimate tensile strength, breaking strength, maximum elongation, and reduction in area. Tensile tests are widely employed in mechanical materials testing and are the basis for comparing a traditional testing machine and a robot-based test bench. The upcoming section will delve deeper into the evaluation by describing both test setups: The tensile test setup on a conventional testing machine and the setup of the robot-based test bench. Following this, the standardized test procedure for the robot-based component testing will be applied, and the tensile tests using the robot-based approach will be performed. For each material (steel, aluminum, polypropylene), three tensile specimens will be taken, both robot-based and on the standard testing machine. Finally, the results obtained from both experiments will be presented and compared to check if the requirements for reproducibility (RE 3), slow velocities (RE 4), high loads (RE 5), and high accuracy (RE 6) can be fulfilled.

9.1.1 Standard Tensile Test Experimental Setup

An overview of the overall experimental setup, including the actuator and all sensors, is given in Figure 9.1. The DIC system GOM ATOS 5 is mounted on a tripod and a classical testing machine equipped with a force sensor. The reference tests were carried out on a Zmart.Pro Z1464 from the manufacturer ZwickRoell. The bone-shaped specimens were clamped with serrated grips (see Figure 9.2). A speckle pattern was applied to the specimen surface to make the specimen evaluable for digital image correlation. In the context of digital image correlation, a speckle pattern refers to a random distribution of small, contrasting, and irregularly shaped features on the surface of an object. These features, known as "speckles," are unique visual markers that can be tracked and analyzed to quantify deformations, displacements, and strains in the material or object under study [114]. The stick-on dots are for the ATOS 5 system and serve as markers that can be tracked. They can also be used to measure the displacements of the clamping jaws. The GOM ATOS 5 system was also used in this test setup to measure these displacements. It was equipped with an MV 1000 objective to ensure the largest possible image section. The occurring forces were measured with the integrated force sensor of the Zmart.Pro Z1464.

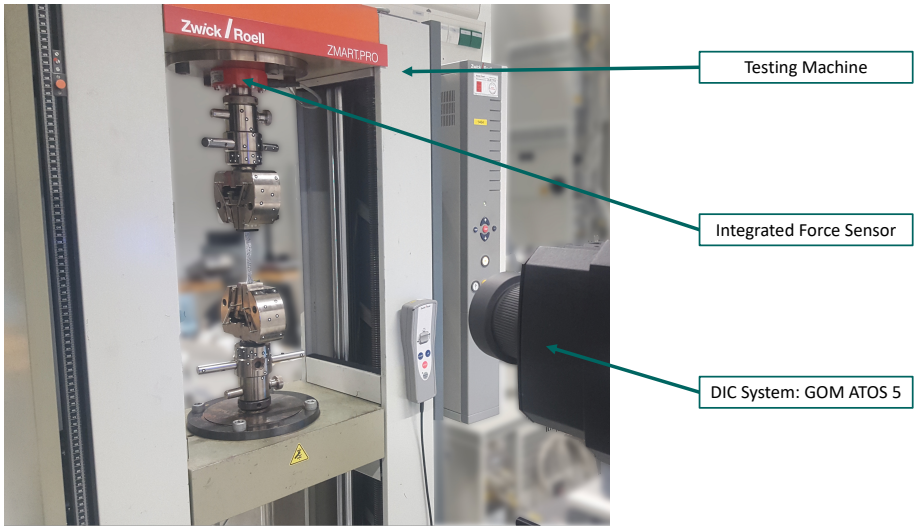

Figure 9.1. Overview of the experimental test setup. It consists of a Zmart.Pro Z1464 testing machine from ZwickRoell with an integrated force sensor and the GOM ATOS 5 DIC system.

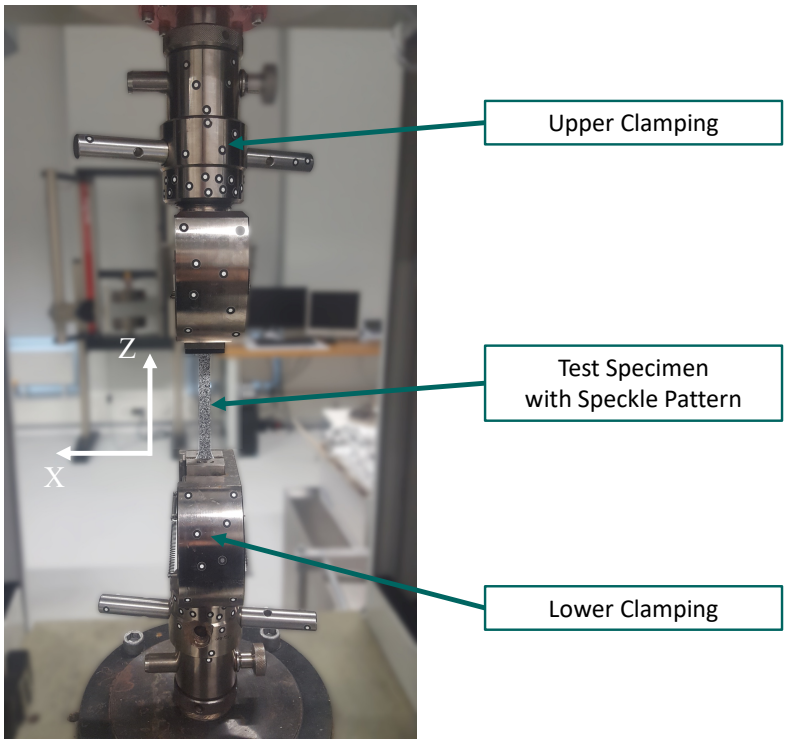

Figure 9.2. Clamped Specimen on a classical testing machine with a black and white speckle pattern applied to it. The forces are measured in the given coordinate system.

9.1.2 Robot-based Testing Facility Experimental Setup

The standardized testing procedure was used to specify the robot-based testing facility setup. This procedure starts with the preparation phase. In the first step of the preparation phase, the component to be tested is analyzed. Here, three different materials for the tensile specimen were chosen, as already described in Section 3.1.2, representing steel, aluminum, and polypropylene components. For the later placement of the specimen, the length of the specimen is the most crucial factor since the clamping works independently of the thickness and width. The Steel and Aluminium specimens have an identical overall length of $180\,\mathrm{mm}$. The polypropylene specimen is smaller with $170\,\mathrm{mm}$ overall length. Table 9.1 summarizes the selected velocities in z-direction and maximum force, which were selected based on the standards testing methods for the three chosen materials.

Material	Ultimate Strength	Testing Velocity
Steel	$19\,500\,\mathrm{N}$	$1\,\mathrm{mm/min}$ until Y-Modul at $6000\,\mathrm{N}$, continuing with $10\,\mathrm{mm/min}$
Aluminium	$7700\,\mathrm{N}$	$5\,\mathrm{mm/min}$
Polypropylene	$750\,\mathrm{N}$	$5\,\mathrm{mm/min}$ until Y-Modul at $200\,\mathrm{N}$, continuing with $50\,\mathrm{mm/min}$

Table 9.1. Load case overview with corresponding forces and velocities for each specimen.

The clamping points are specified by jaws used for the tensile specimens in the same way as for the standard testing machine. After analyzing the dimension, the loading points, the material properties, and the clamping points, the clamping must be selected, as well as the robot end-effector.

Figure 9.3 shows the end-effector mounted directly to the f/t-sensor and the clamping device for the tensile specimen. With all this information, the first step of the standardized test procedure is finished. The next step is the definition of the measuring technique. Both available sensor systems are to be used for these tests. This means that all forces (FX, FY, FZ) and all moments (TX, TY, TZ) are to be measured by the f/t-sensor mounted on the robot flange, and all shifts (DX, DY, DZ) and twists that occur (DA, DB, DC) are to be measured by the camera system. The f/t-sensor was chosen to detect the specimen's fracture and record the forces and torques acting on the component. The ATOS 5 was used as a second sensor to measure the specimen displacements and the robot deviations. It was also equipped with an MV 1000 objective to ensure the largest possible image section. A speckle pattern was applied to the specimen surface to make the specimen evaluable for digital image correlation. After completing the definition of the measuring technique, the next step is to define the motions. Three different types of test motions were chosen to compare the result. One for each regulation type (optical-based, f/t-based and internal). The first two represent the sensor-guided motions and the third is controlled by the internal KUKA control system. For the steel specimen and

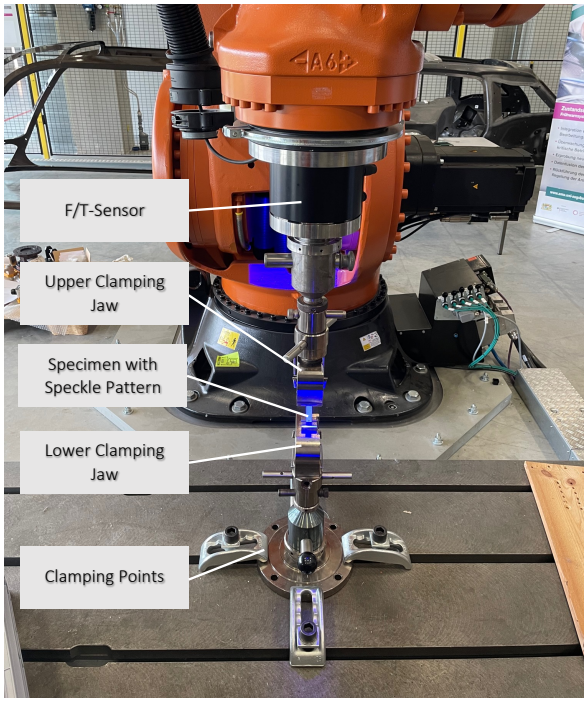

Figure 9.3. Tensile test setup: Attachment of the clamping jaws with clamped tensile specimen between the clamping field (bottom clamping point) and the robot end-effector (top), consisting of the f/t-sensor and the upper clamping jaw.

for the PPH specimen, two motions per regulation type were selected, one slower and one until fracture. For aluminum, only one continuous test motion at the same velocity was performed per regulation type. The motions are summarized in Table 9.2. The given velocities in z-direction and termination criteria can be taken from the previous table (Table 3.1) and are derived from the standard test procedures for tensile tests mentioned in Section 3.1.2. For the force-based motions, it was also specified for the control that all transverse forces (FX and FY) should be controlled to zero. The same applies to the optical-based control, except the absolute deviation in (LX, LY, A, B, C) is controlled to zero. The clamping device and the chosen robot end-effector give the orientation of the test motion. Since the clamping places the specimen perpendicular to the clamping field and the resulting test motion acts in the direction of the clamped specimen, the end-effector orientation in the robots base coordinate system $a = -90°, b = 0°, c = 180°$ can be obtained for the test motion. The direction of the linear test motion is in the z-direction.

Regulation	Material	Termination Crit.	Velocity	Orientation
Optical	Steel	6000 N	1 mm/min	a=−90°, b=0°, c=180°
Optical	Steel	break	10 mm/min	a=−90°, b=0°, c=180°
Optical	Aluminium	break	5 mm/min	a=−90°, b=0°, c=180°
Optical	PPH	200 N	5 mm/min	a=−90°, b=0°, c=180°
Optical	PPH	break	50 mm/min	a=−90°, b=0°, c=180°
F/T-Based	Steel	6000 N	1 mm/min	a=−90°, b=0°, c=180°
F/T-Based	Steel	break	10 mm/min	a=−90°, b=0°, c=180°
F/T-Based	Aluminium	break	5 mm/min	a=−90°, b=0°, c=180°
F/T-Based	PPH	200 N	5 mm/min	a=−90°, b=0°, c=180°
F/T-Based	PPH	break	50 mm/min	a=−90°, b=0°, c=180°
Internal	Steel	6000 N	1 mm/min	a=−90°, b=0°, c=180°
Internal	Steel	break	10 mm/min	a=−90°, b=0°, c=180°
Internal	Aluminium	break	5 mm/min	a=−90°, b=0°, c=180°
Internal	PPH	200 N	5 mm/min	a=−90°, b=0°, c=180°
Internal	PPH	break	50 mm/min	a=−90°, b=0°, c=180°

Table 9.2. Three different types of test motions were chosen. One for each regulation mode of the sensor-guided motions (optical and f/t-based) and two test motion with the internal KUKA control system. For steel and pph, different velocities were then selected for each regulation type.

After defining the test motions, the corresponding test motion sequence must be defined. The motion sequence is the same for all motions. First, the slow motion is started until the Y-Modul is reached and then pulled until the break occurs. After the motion defining the step, the component placement was carried out with the help of the CASP algorithm. First of all, parameters for querying must be collected by the planning component. The forces are given by the tensile specimen's load limits and are at a given maximum of 25 kN for the steel specimen. The clamping height and end-effector give the desired orientation and height parameters (z, a, b, c). To determine the starting height $z = 130\ cm$ for the component test, the height of the end-effector can be measured as a sum of the lower clamping jaw plus the length of the specimen plus the length of the end-effector with the f/t-sensor mounted combined with the upper clamping jaw. The last step is determining the distance the robot needs to travel to ensure it can build up the force of $25\,\mathrm{kN}$ over the entire distance. This can be done, for example, with the help of a FEM simulation. In this example, the maximum distance is circa $20\,\mathrm{cm}$. In this

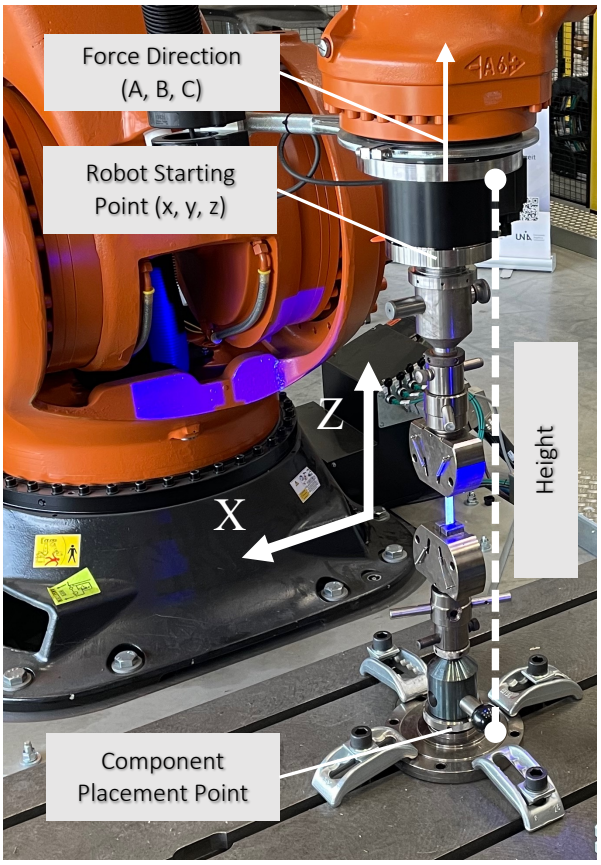

Figure 9.4. Applied CASP approach: The given force direction indicates in which direction the force is to be applied to the specimen by the robot. The height can be measured and the resulting starting point and the component placement point is calculated.

example, the CASP algorithm has selected the position $x = 50\ cm$, $y = 156\ cm$, and $z = 130\ cm$ for the robot starting point, corresponding to the position shown in 9.4. This also denotes that the robot can apply the required forces for this chosen use case. In the next step, the approach and departure motion must be defined. Since the focus is on the test motion, only one optical approach motion was selected, and the departure motion was also omitted. In this use case, a pause was made between the approach and test motion to allow the insertion of the test object between the two clamping devices. In addition to the sensor-based motions, the same motions were also performed without any correction relying on the internal position system of the robot. In this case, the f/t-sensor was only used to detect the termination criteria and, therefore, to inform the internal control system when the velocity, i.e., for the second test motion, should be increased. In the next phase, the motions were executed until the specimens broke, and the data from the f/t-sensor and the ATOS 5 were aggregated and recorded. This will be discussed in the next section.

The final test setup in the robot-assisted test facility is illustrated in Figure 9.5 and consists of a robot with clamping jaws as the end-effector and a corresponding counterpart on the clamping field. In this case, the ATOS 5 is mounted on the second robot. The coordinate system's orientation in which the robot is controlled and all deviations are measured is also shown in this figure. Finally, the post-processing phase was started with the data evaluation, and the results will be discussed in the next section.

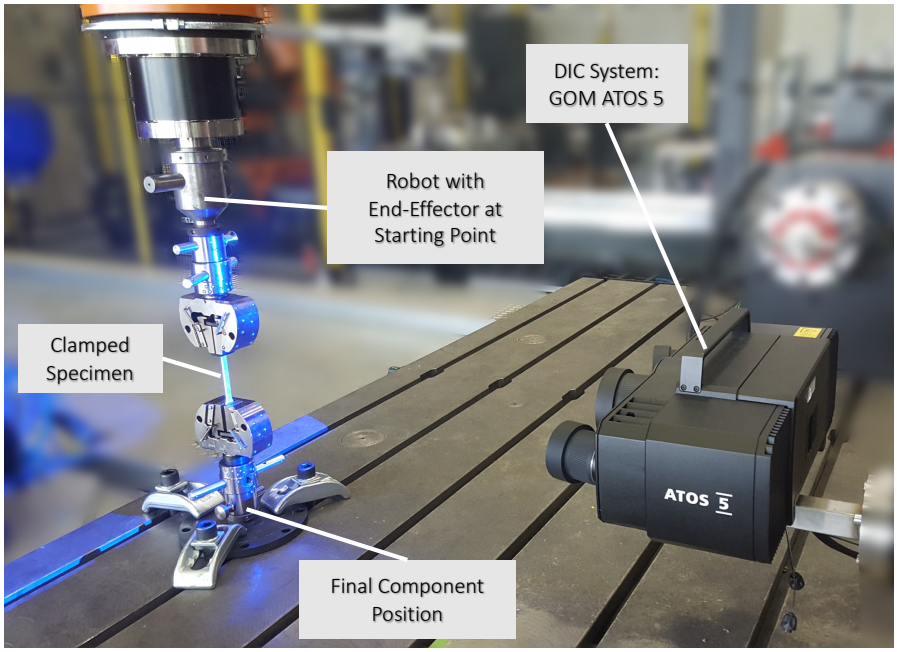

Figure 9.5. Overview of the final tensile test setup with the specimen setup mounted on clamping field on the left side and the camera on the right side.

9.1.3 Analysis of the Results

To include variations of individual specimens, three tensile tests were carried out for each material for each type of regulation and also three per type of material on the tensile machine. First, the material properties are compared with each other. For this purpose, each tensile specimen is depicted in a stress-strain diagram (see Figure 9.6). Each diagram consists of respective averaged tests, three per diagram. Furthermore, it includes the four regulation types. The curve of the universal testing machine is orange, the optical-based control curve is blue, the force-based is black, and the internal KUKA-based is green. The universal testing machine curve for steel (orange) has a slightly higher stress and strain value at the end of the test than the curves of the robot-based test. These hardly differ in recorded stress and strain. The material properties also reflect these results (see Table 9.3). In this context, the elastic modulus, strength, and strain are average values for both robot-based and machine-based tests. Furthermore, the standard deviation is presented for the mean values derived from three distinct robot-based tests and the tests conducted on the machine. Notably, the strength and strain observed in the robot-based tests are comparatively lower than those in the machine-based tests for the steel specimen and vice versa for the aluminum specimen. However, there is also a slight deviation in Young's modulus, with the machine-based tests differing from the robot-based tests. Moreover, the findings align closely with the specifications in the data sheet for the stainless steel and aluminum used. The data sheet for stainless steel, e.g., indicates a tensile strength ranging from 500 MPa to 700 MPa and an elongation at break greater than or equal to 45% [17]. Remarkably, both the robot-based and traditional tensile tests yield results consistent with the values specified in the aluminium and stainless steel data sheet. In the last test case, the curve of the PPH specimen is slightly higher than the other curves because the tests on the robot were performed in a too-high time interval. As a result, the material has changed. Nevertheless, the PPH specimen's deviation, lateral forces, and torques will also be analyzed in the later course of the evaluation.

Regulation Type	**Y-Modulus [GPa]**	**Strength [MPa]**	**Strain [%]**
AVG & SD Atos-based	202.61 $\pm$ 1.21	659.40 $\pm$ 1.25	48.82 $\pm$ 0.04
AVG & SD Force-based	211.45 $\pm$ 4.29	665.28 $\pm$ 1.33	49.15 $\pm$ 0.54
AVG & SD KUKA-based	215.11 $\pm$ 3.15	657.84 $\pm$ 1.17	49.07 $\pm$ 0.48
AVG & SD Robot-based	209.72 $\pm$ 6.12	660.84 $\pm$ 3.44	49.01 $\pm$ 0.44
AVG & SD Testing Machine	201.01 $\pm$ 8.81	668.92 $\pm$ 7.00	53.1 $\pm$ 2.58

Table 9.3. Comparison of the material parameters (elastic modulus, strength and strain) between the robot-based tests and the tests performed on the testing machine for the steel specimen.

Regulation Type	Y-Modulus [GPa]	Strength [MPa]	Strain [%]
AVG & SD Atos-based	72.18 ± 0.30	270.04 ± 0.66	15.07 ± 0.92
AVG & SD Force-based	73.19 ± 0.99	270.11 ± 1.09	13.43 ± 1.14
AVG & SD KUKA-based	72.25 ± 0.50	269.43 ± 0.31	14.16 ± 0.70
AVG & SD Robot-based	72.54 ± 0.81	269.86 ± 0.82	14.22 ± 1.15
AVG & SD Testing Machine	69.49 ± 0.44	267.58 ± 0.59	14.03 ± 0.96

Table 9.4. Comparison of the material parameters (elastic modulus, strength and strain) between the robot-based tests and the tests performed on the testing machine for the aluminum specimen.

Since the material characteristics (see Table 9.3 and Table 9.4) of steel and aluminum hardly differ, this initially shows that it is possible to perform robot-based material tests. To enhance the verification of sensor-guided test motions and assess accuracy (RE 6) more effectively, precise control variables such as positional deviation and lateral forces are subjected to closer scrutiny during the tensile tests. The sampling rate corresponds to the recording frequency of the ATOS 5 camera (10Hz), wherein both the positional deviation and lateral forces where aggregated and are depicted. It's important to note that the measurement of lateral forces was exclusive to the robot-based testing, as this aspect was solely under control in that context. The force sensor on a standard testing machine is designed for tension and compression tests, and as such, it can only measure forces in the direction of tension or compression.

Figure 9.7 presents the averaged position deviation data for various controlled robot test motions, alongside the deviation observed with the universal testing machine. To assess this position deviation, a coordinate system is established at the midpoint between the two clamping jaws using the ATOS 5 system. For both the testing machine and robot-based tests, the fixed clamping jaw serves as the reference point. During robot-based tensile tests, the upper clamping jaw, linked to the robot, is manipulated to match the position of the lower fixed clamping jaw. The deviation in the x-direction and y-direction signifies the variation from this reference clamping jaw. The optical-based control implemented with the ATOS 5 camera is depicted by the blue line, showcasing that, after a brief settling period, the deviation in the x-direction and y-direction can be minimized to nearly $0\,\mathrm{mm}$ for all specimens. As anticipated, the results from the tensile tests on the testing machine (indicated by the orange curve) also reveal minimal deviations. Conversely, the curve representing the position control of the internal robot control exhibits substantial deviation (green line). As previously observed in preliminary tests, the accuracy of internal robot positioning diminishes as the applied load on the robot increases.

Figure 9.8 illustrates the averaged transverse forces observed during various controlled robot test motions. The grey line traces the curve of the force control, indicating that transverse forces in the x-direction and y-direction can be reduced below $\pm\,5\,\mathrm{N}$.

In contrast, both the optical-based control (blue) and internal robot control (green) consistently yield higher transverse forces. Particularly with the steel specimen, the internal control system and optical-based controlled motions result in transverse forces exceeding $100\,\mathrm{N}$ in x-direction and over $150\,\mathrm{N}$ in y-direction.

To analyze the repeatability of motions more accurately, a detailed examination was conducted using the steel sample as an example, as it exhibited the greatest deviation and required the highest force. As depicted in Figure 9.9, the absolute deviation for the steel specimen in the tests is shown in the upper part of the graph. The curves represent the measured results of all three tests for the respective samples. It is evident that in the position-controlled mode, the deviations are nearly zero, in contrast to the force-based case where deviations vary within the range of $\pm\ 0.1\,\mathrm{mm}$. It is also evident for the force-controlled mode, that the force deviations are nearly zero, in contrast to the position-controlled mode were deviations vary within the range of $\pm\ 5\,\mathrm{N}$. This demonstrates that when the position or the force is controlled, it can consistently be repeated with minimal fluctuations (RE 3).

In summary, the assessment of conventional tensile tests demonstrates the feasibility of robot-based component testing in principle. The developed control system facilitates the compensation of inherent deformations in the robot (RE 6), enabling the execution of two test motion types at both slow velocities (RE 4) and high forces (RE 5). Furthermore, this motion can be consistently performed with repeatable accuracy, facilitating reproducibility, which is further supported by the standardized test procedure (RE 3). The extent to which the robot-based testing facility and the developed artifacts can be flexibly employed will now be subject to further evaluation in subsequent case studies.

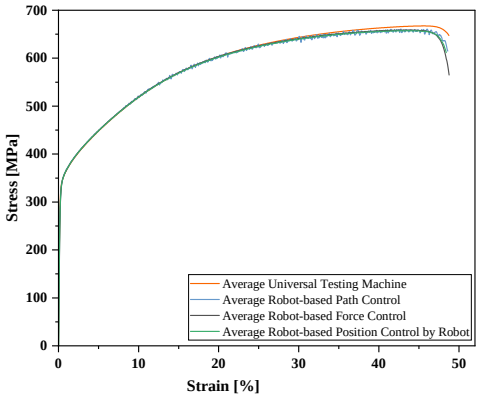

(a) Stress-strain curves for the steel specimen.

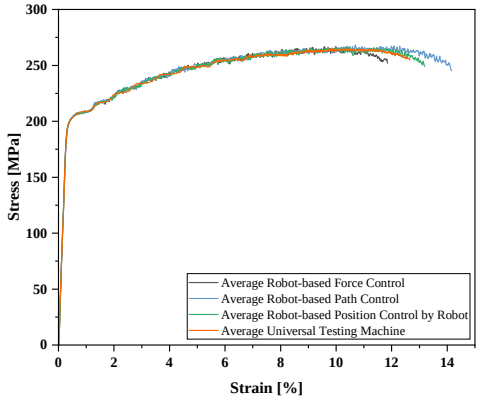

(b) Stress-strain curves for the aluminum specimen.

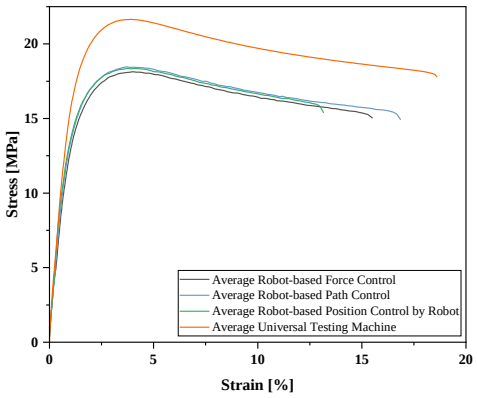

(c) Stress-strain curves for the pph specimen.

Figure 9.6. Stress-strain diagrams of the tested specimen. Four different test methods are compared: force, path and position control according to the internal robot control and tensile tests on the universal testing machine. In each case three specimens were tested and the value is averaged.

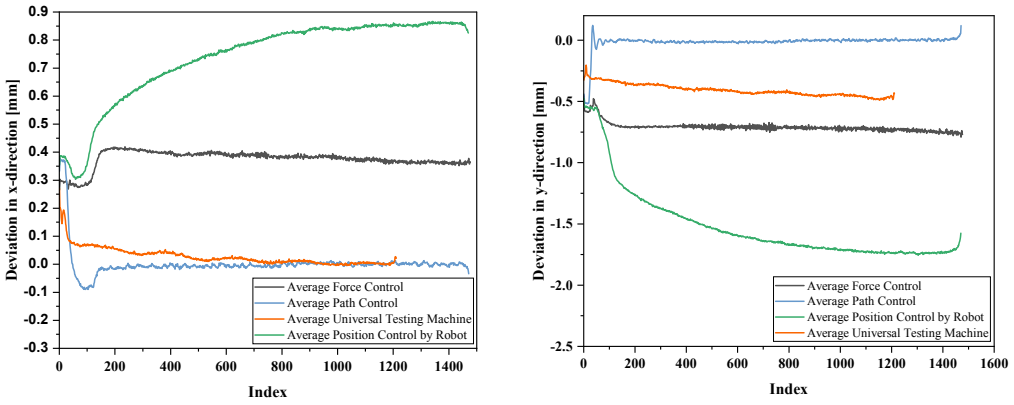

(a) Averaged position deviation in x-direction (on the left) and y-direction (on the right) for the steel specimen.

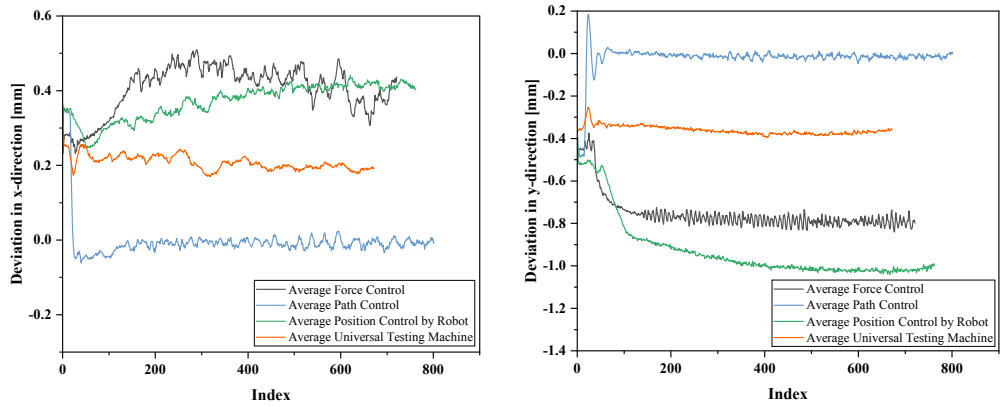

(b) Averaged position deviation in x-direction (on the left) and y-direction (on the right) for the aluminum specimen.

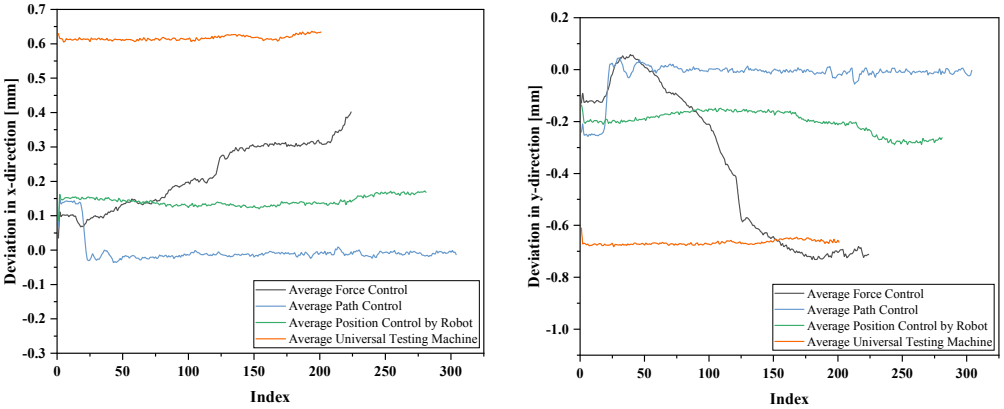

(c) Averaged position deviation in x-direction (on the left) and y-direction (on the right) for the pph specimen.

Figure 9.7. Averaged position deviation in x-direction and y-direction for the different robot-based test motions and the tests performed on the testing machine during the tensile tests for the different materials.

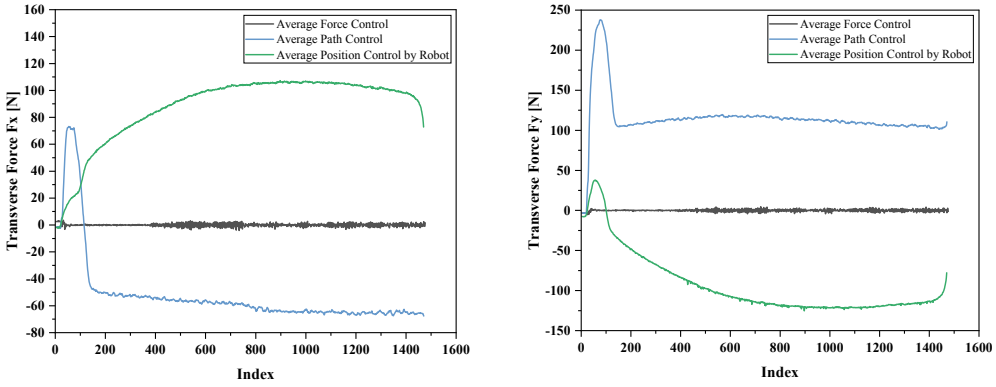

(a) Averaged transverse forces (Fx on the left and Fy on the right) for the steel specimen.

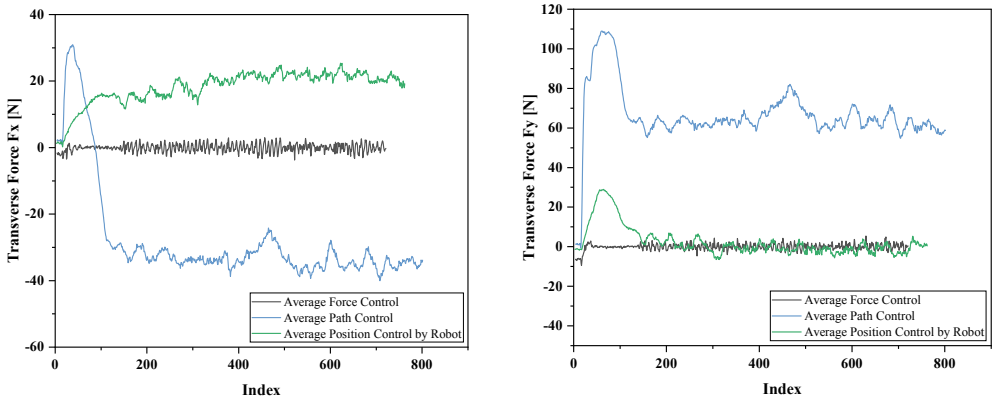

(b) Averaged transverse forces (Fx on the left and Fy on the right) for the aluminum specimen.

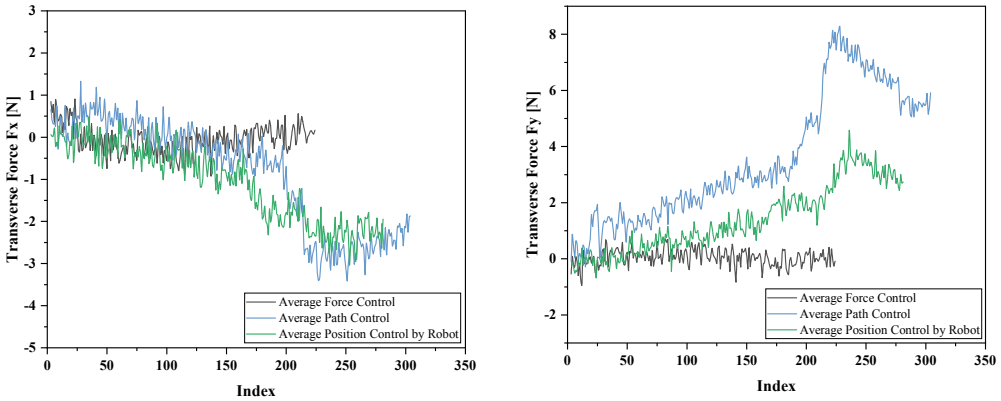

(c) Averaged transverse forces (Fx on the left and Fy on the right) for the pph specimen.

Figure 9.8. Averaged transverse forces (Fx and Fy) for the different robot-based test motions during the tensile test for the three chosen specimen materials.

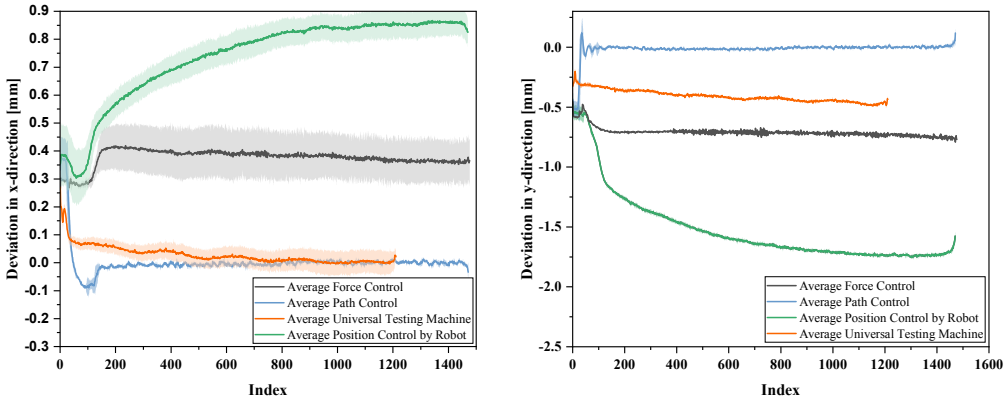

(a) Averaged position deviation deposited with variations in x-direction (on the left) and y-direction (on the right) for the steel specimen.

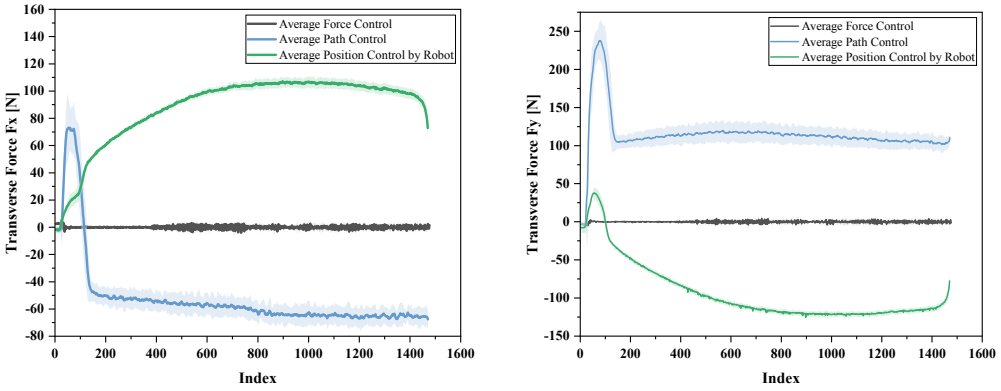

(b) Averaged transverse forces deposited with variations (Fx on the left and Fy on the right) for the steel specimen.

Figure 9.9. Averaged position (a) and force deviations (b) for the different robot-based test motions during the tensile for the three steel specimen deposited with variations.

9.2 Case Study 2: Bicycle Frame

During cycling, high loads can lead to excessive stress on the bicycle frame, potentially causing cracks that eventually result in structural failure. Even small loads can initiate micro-cracks in materials, propagating into visible macroscopic cracks under continuous cyclic loading until the structure fails. Most test benches are specific to one test object, e.g., bicycles and, therefore, are dedicated to the type of component that must be tested. Furthermore, these test benches map only a few exceptional load cases, e.g. one linear test motion. It is only possible to test one part of a bicycle frame on a test stand without rebuilding it or manufacturing a second one to test other parts of the bicycle frame. This case study will investigate how flexible (RE 1) and how accurate (RE 6) a robot can implement different testing motions with different positions and orientations. The fulfillment of the requirements resulting from this second case study can also be evaluated. The upcoming sections will delve deeper into the evaluation by describing first the experimental test setup and the test execution. This is performed using the developed standardized test procedure and the bike frame already described in Section 3.2.3. Finally, the results obtained from the experiments will be presented.

9.2.1 Experimental Setup

The first step of the standardized testing procedure was used to specify the robot-based testing facility experimental setup. In the preparation phase, the first step is analyzing the bike frame. The frame is made of aluminum, and the fork is made from carbon

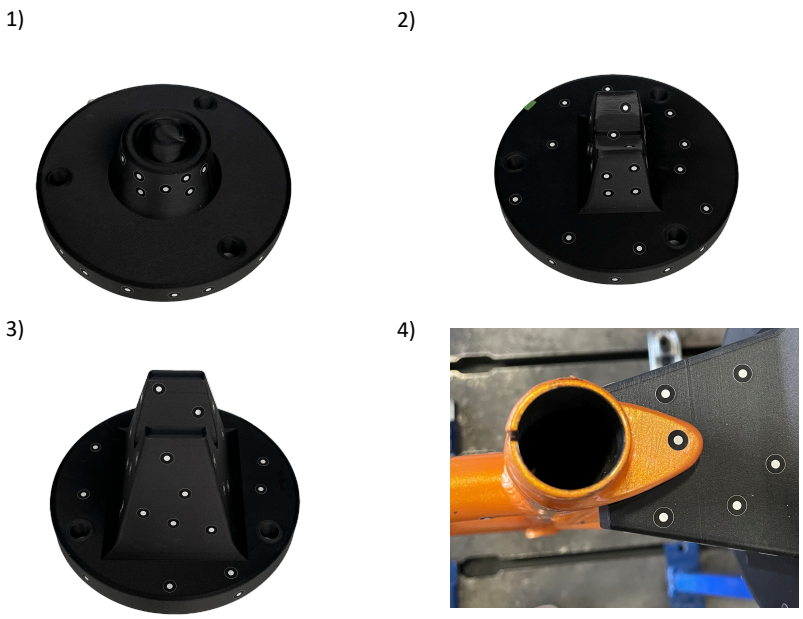

Figure 9.10. Developed end-effectors for the respective loading points (1 to 3) on the frame. (4) shows an example of the negative shape of the third end-effector.

(rigid fork). It has the following maximum dimensions 100 cm cm length x 16.5 cm width x 69 cm height and fits easily on the clamping area. The test consists of three different loading points described in more detail in Section 3.2.3. The first loading point is located at the seat post, the second loading point is located at the head tube, and the last one is located at the seat tube. Attaching the frame directly to the clamping field with these load points is not possibles. Since the frame with the t-slots and the clamping device cannot be mounted upright directly on the clamping field. Therefore, a clamping device was designed and manufactured from clamping blocks and aluminum profiles (Item), which is attached to the clamping field (see Figure 9.11). The developed clamping devices connect the bike's dropouts firmly to the clamping field and can thus be used for any bikes that also have such dropouts. The appropriate end-effector for the robot bench must first be developed to apply the loads to the frame. The respective frame shape must be taken into account in order to create a form fit. Figure 9.10 shows the three different developed end-effectors for each loading point. The fourth part of this figure shows an example of the negative shape of the third end-effector. In this case dots were glued on to measure the displacements.

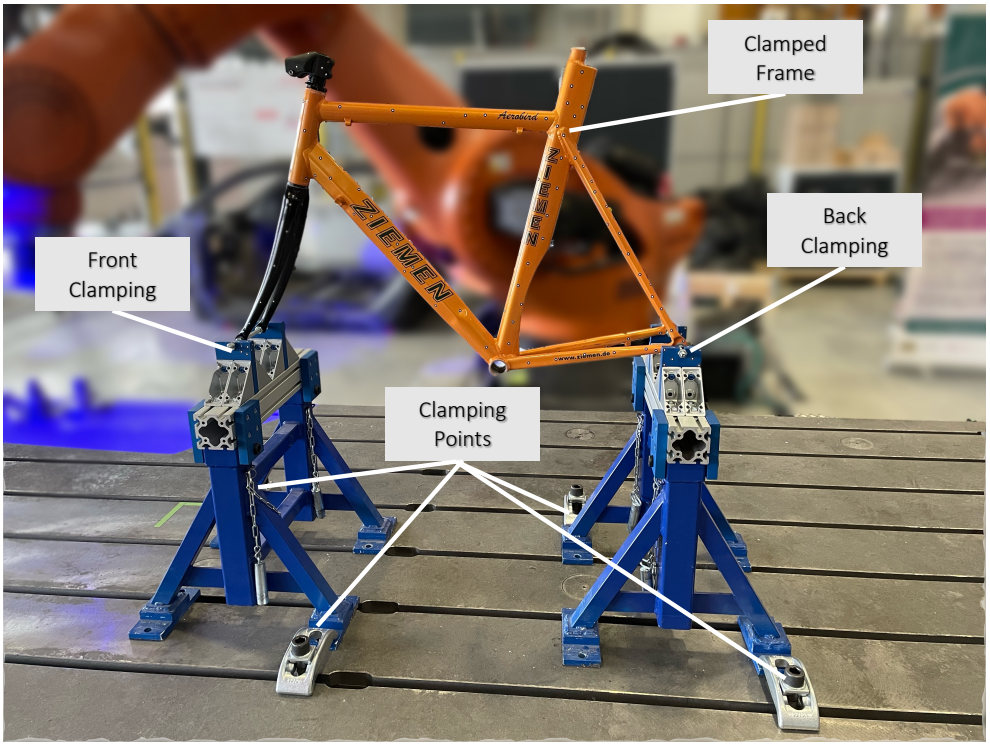

Figure 9.11. Clamped bike frame in the designed clamping device. The bike frame is attached via its drop outs to the clamping device and the clamping device is fixed on the clamping field via t-slot nuts and jaws.

With all this information, the first step of the standardized test procedure is finished. The next step is the definition of the measuring technique. Analogous to the first use case,

both available sensor systems will be used for these tests. The f/t-sensor was chosen to detect and record the forces and torques acting on the bike frame. The ATOS 5 was used as a second sensor to measure the bike displacements and the robot deviations. It was also equipped with an MV 1000 objective to ensure the largest possible image section. After the measuring technique is defined, the next step is to define the motions. Two different types of test motions (optical-based and f/t-based) for each loading point were chosen, and for each type, two test motions were carried out for each load case. The motions are summarized in Table 9.5. For the force-based motions, it was also specified for the control that all transverse forces (fx and fy) should be controlled to zero. The same applies to the optical-based control, except the absolute deviation in (lx, ly, a, b, c) is controlled to zero. The given velocities and termination criteria can be taken from the problem definition of this case study (Table 3.2). The clamping device and the chosen

Load Case	Regulation	Termination Crit.	Velocity	Orientation
1	Optical	100 N	5 mm/min	a=−93°, b=1°, c=−176°
1	Optical	1000 N	2 mm/min	a=−93°, b=1°, c=−176°
1	F/T-Based	100 N	5 mm/min	a=−93°, b=1°, c=−176°
1	F/T-Based	1000 N	2 mm/min	a=−93°, b=1°, c=−176°
2	Optical	100 N	5 mm/min	a=−90°, b=2°, c=108°
2	Optical	2000 N	2 mm/min	a=−90°, b=2°, c=108°
2	F/T-Based	100 N	5 mm/min	a=−90°, b=2°, c=108°
2	F/T-Based	2000 N	2 mm/min	a=−90°, b=2°, c=108°
3	Optical	500 N	2 mm/min	a=71°, b=56°, c=64°
3	F/T-Based	500 N	2 mm/min	a=71°, b=56°, c=64°

Table 9.5. Two different types of test motions for each regulation mode of the sensor-guided motions (optical and f/t-based) were chosen for each loading point. In addition, the same motions were also carried out with the internal KUKA control system.

robot end-effector give the orientation of the test motion. All motions in a linear test motion are in z-direction with only one velocity in this direction.

After defining the test motions, the corresponding test motion sequence must be defined. The motion sequence is the same for load case 1 and load case 2. First, the slow motion is started until the force termination criterium is fulfilled, and then the second motion is executed until its termination criterium is reached. Only one testing motion is executed for the third load case until its force termination criteria is fulfilled. After defining the motions, the component placement could be carried out. In this case, low forces have to be applied. Therefore, the position on the clamping field can be almost freely selected. A central position, for example, ensures that the robot can reach all points. Of course, it is also possible to specify a position with the help of the CASP approach. In the next step, the approach and departure motion must be defined. Since the focus is on the test motion, only two approach motions were selected (one optical and one f/t-based). The f/t-based approach motion was used for approaching the component for the f/t-based testing motions and respectively the optical approach motion was used for approaching the component for the optical based testing motions. A positioned-based motion was chosen as the departure motion. Figure 9.12, Figure 9.13 and Figure 9.14 show the final test setups for the next phase. In all cases, the ATOS 5 is mounted on the second robot. The right-handed coordinate system's orientation in which the robot is controlled and all deviations are measured is also shown in the respective figure. In the next phase, the motions were executed until the (termination criteria) maximum forces were reached, and the data from the f/t-sensor and the ATOS 5 were aggregated and recorded. This will be discussed in the next section.

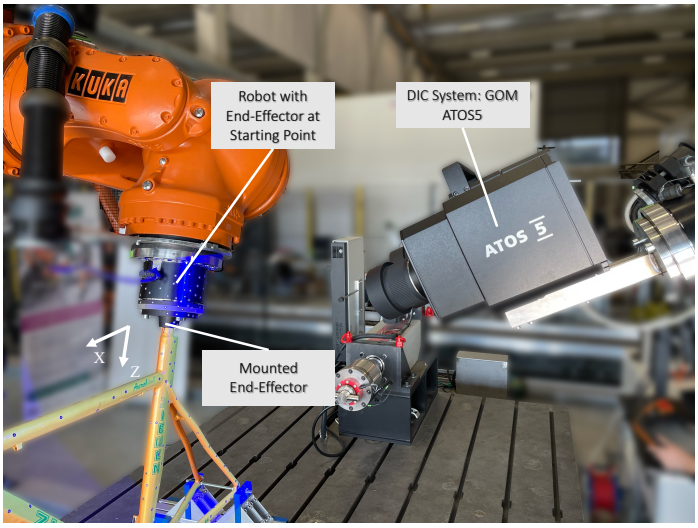

Figure 9.12. Overview of the final test setup for the first loading point with the bike frame mounted on the clamping field on the left side and the camera on the right side.

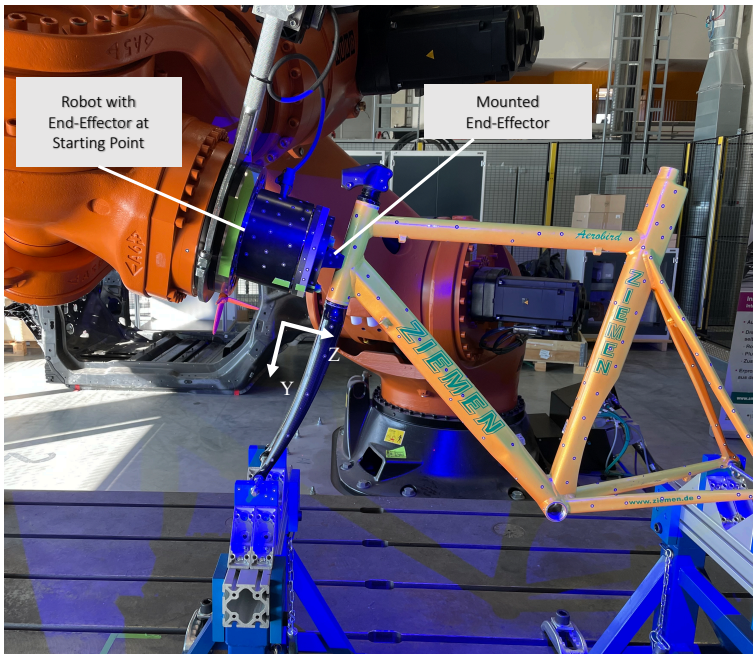

Figure 9.13. Overview of the final test setup for the second loading point with the bike frame mounted on the clamping field on the left side and the camera on the right side.

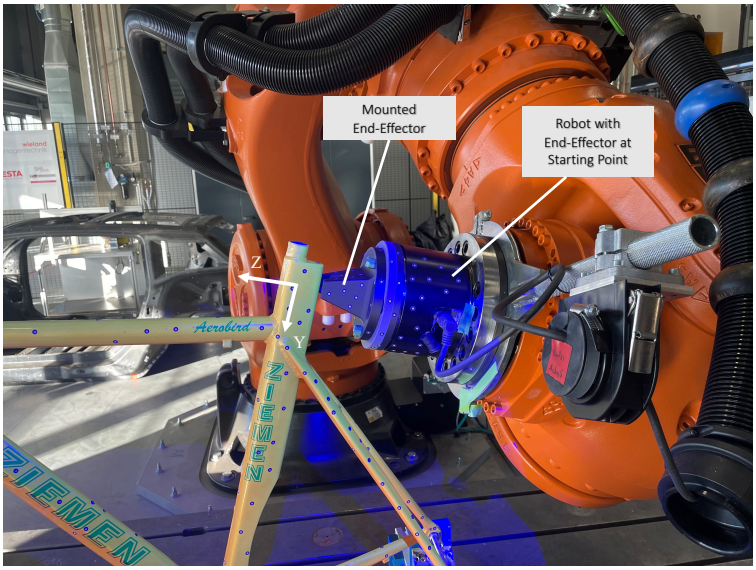

Figure 9.14. Overview of the final test setup for the third loading point with the bike frame mounted on the clamping field on the left side and the camera on the right side.

9.2.2 Analysis of the Results

How flexible (RE 1) and how accurate (RE 6) a robot can execute slow (RE 4) testing motions with different positions and orientations is to be investigated in this case study. For this purpose, the individual forces, positions, and deviations of the executed test motions are now analyzed. The sampling rate corresponds to the recording frequency of the ATOS 5 camera, capturing an image every 10Hz, wherein both the positional deviation and lateral forces where aggregated and are depicted. This is represented by the Index in all Figures. Furthermore, only the forces or deviations that were controlled are evaluated. For example, in the force-controlled case, the deviation is not evaluated.

Load Case 1: Seat Post
Figure 9.15 depicts the transverse forces in Newton (N) and the deviation in millimeter (mm) the end-effector while loading the seat post in the z-direction (green for the force and blue for the traveled distance in the z-direction) up to $2000\,\mathrm{N}$. The force is negative in this case because the sensor's internal coordinate system records it that way (see Figure 9.12). Figure 9.15a was controlled optically. The y-axis mainly shows the deviation in mm and the aggregated force is also displayed (in green). Figure 9.15b was force controlled. The y-axis shows the forces in N. In the beginning, the respective approach motion can be seen in both cases, which initially corrects the deviation in mm in the optical case (until index 1500) and reduces the forces in the force-regulated case (until index 1500). Then, the test motions are carried out, which loads the seat post up to 2000 N. It can be concluded that the deviation can be reduced to approximately ± $0.02\,\mathrm{mm}$ in x-direction and ± $0.02\,\mathrm{mm}$ in y-direction. For the force-controlled test motion, it can be concluded that the forces can be controlled to a range of $0\,\mathrm{N}$ to $2.5\,\mathrm{N}$ for both axes. Finally, the test stopped at $2000\,\mathrm{N}$, and the departure motion occurred. The departure motion has been omitted here since the focus is on the test motion.

Load Case 2: Head Tube
Figure 9.16 depicts the transverse forces in Newton (N) and the deviation in millimeter (mm) the end-effector while loading the head tube in the z-direction (green for the force and blue for the traveled distance in the z-direction) up to $1000\,\mathrm{N}$. The force is negative in this case because the sensor's internal coordinate system records it that way (see Figure 9.13). Figure 9.16a was controlled optically. The y-axis mainly shows the deviation in mm and the aggregated force is also displayed (in green). Figure 9.16b was force controlled. The y-axis shows the forces in Newton (N). Initially, both cases exhibit an initial approach motion, visible in the graph, which rectifies the deviation in millimeters in the optical case (index 100) and lessens the forces in the force-regulated case (index 100). The actual test motions are then performed, subjecting the head tube to a load of up to $1000\,\mathrm{N}$. From the results, it can be deduced that the deviation in the x-direction and y-direction can be minimized to approximately ± $0.1\,\mathrm{mm}$. For the force-regulated test motion, the data indicates effective force control within a range of ± $2.5\,\mathrm{N}$ for both axes. Furthermore, it can be seen in this test case that although an approach motion was carried out (until index 120) in the force-regulated case, strong lateral forces occur ($-4\,\mathrm{N}$ for x-direction and $3\,\mathrm{N}$ for the y-direction) at the beginning of the motion, but these can be quickly compensated in the further course.

Load Case 3: Seat Tube

The chart presented in Figure 9.17 is structured analogous to the two load cases above, and the load is applied to the seat tube. The load applied reaches up to $500\,\mathrm{N}$. Initially, both scenarios show an initial approach motion, as evident in the graph, aimed at rectifying the deviation in millimeters within the optical scenario (index 200) and mitigating forces within the force-regulated scenario (index 200). Subsequently, the actual test motion is carried out, subjecting the seat post to a load of up to $500\,\mathrm{N}$. The outcomes indicate that the deviation in both the x-direction and y-direction can be reduced to approximately ± $0.1\,\mathrm{mm}$. Regarding the force-regulated test motion, the data suggests effective control of forces within a range of ± $5\,\mathrm{N}$ for both axes. What can also be observed very well in this example is that the force curve is more homogeneous in the force-regulated motion. This did not occur so strongly in the two load cases before.

In summary, evaluating the bicycle frame demonstrates the feasibility of conducting diverse test motions on a single component. This encompasses the adaptable application of standardized testing procedures and the flexible execution of the test motions, fulfilling the first requirement (RE 1). Moreover, the motion can be executed accurately (RE 6) and at a slow velocity (RE 4). In the optical control scenario, the maximum deviations were under ± $0.1\,\mathrm{mm}$ for both the x-direction and y-direction in the most challenging scenario. In the force-regulated scenario, the maximum deviations were below ± $5\,\mathrm{N}$ for both the x-direction and y-direction in the most challenging scenario.

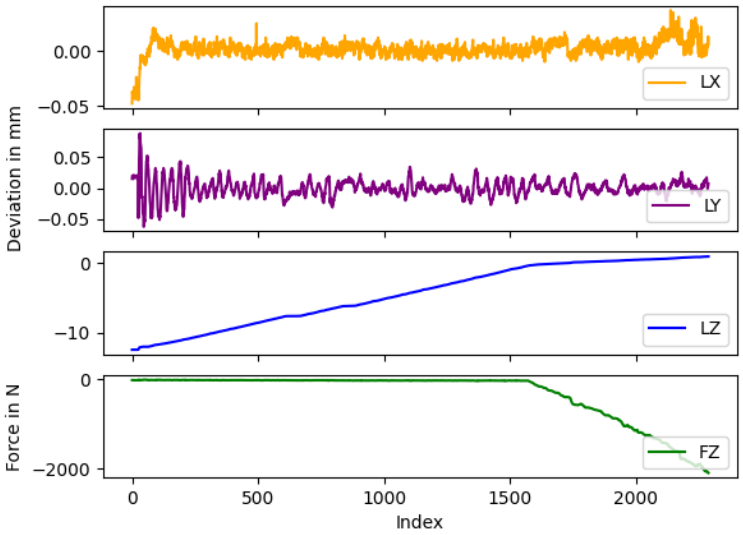

(a) Deviation in mm in x-direction, y-direction (LX, LY) of the end-effector under load using a camera-based position correction. In addition, the distance traveled in z-direction (LZ) and the occurring force in z-direction are also specified (FZ).

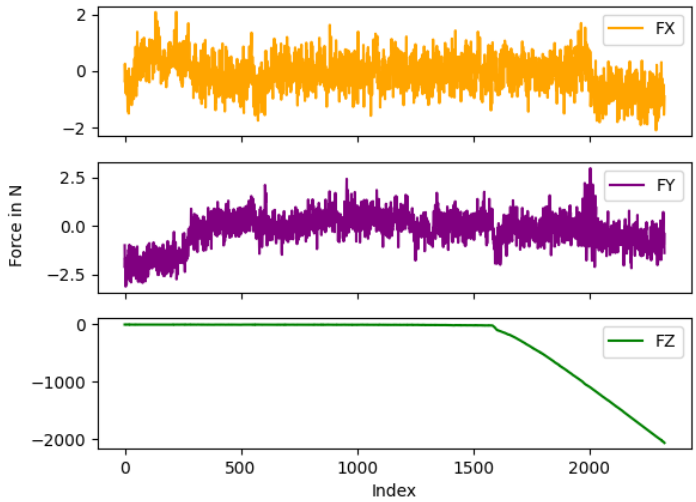

(b) Transverse forces in N in x- and y-direction (FX, FY) of the end-effector under load with the use of a force based correction. In addition, the occurring force in z-direction is also specified (FZ).

Figure 9.15. Deviation and transverse forces under load of the seat post with the use of a camera based motion correction (a) and the force based motion correction (b).

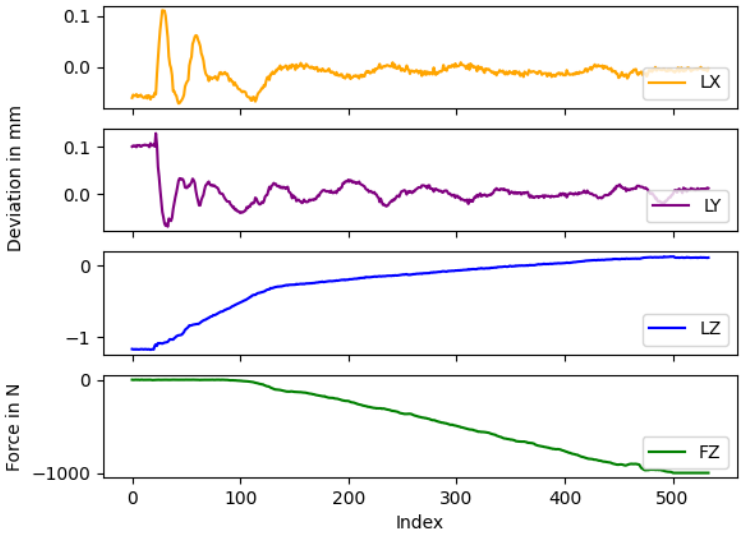

(a) Deviation in mm in x-direction, y-direction (LX, LY) of the end-effector under load using a camera-based position correction. In addition, the distance traveled in z-direction (LZ) and the occurring force in z-direction are also specified (FZ).

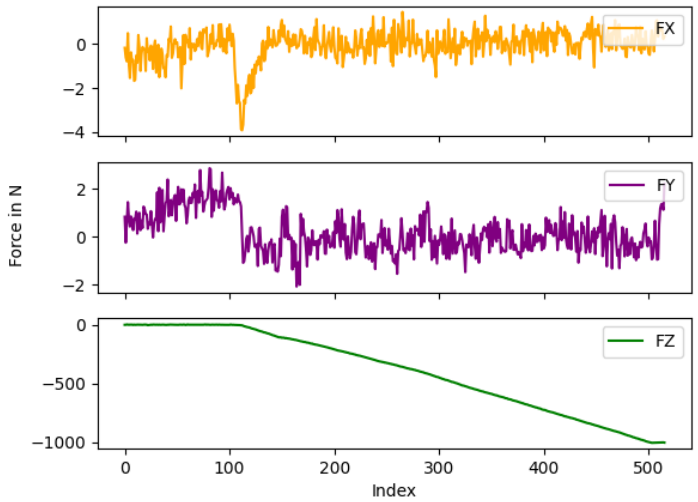

(b) Transverse forces in N in x- and y-direction (FX, FY) of the end-effector under load with the use of a force based correction. In addition, the occurring force in z-direction is also specified (FZ).

Figure 9.16. Deviation and transverse forces under load of the head tube with the use of a camera based motion correction (a) and the force based motion correction b).

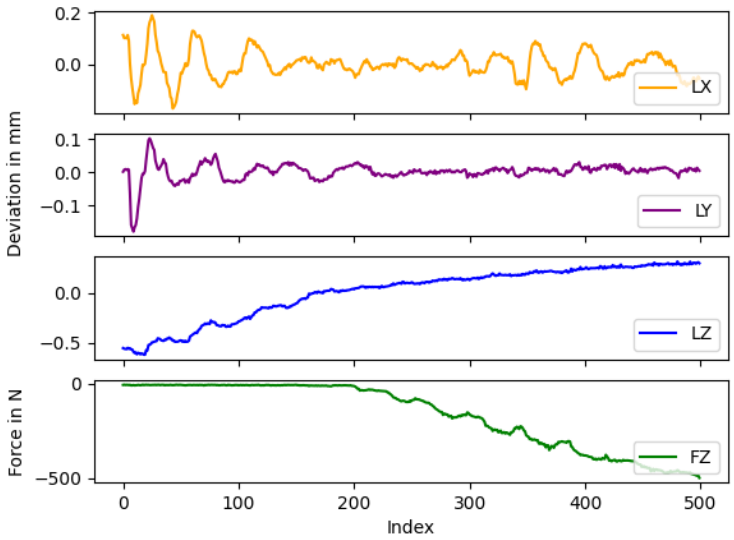

(a) Deviation in millimeter in x-direction, y-direction (LX, LY) of the end-effector under load using a camera-based position correction. In addition, the distance traveled in z-direction (LZ) and the occurring force in z-direction are also specified (FZ).

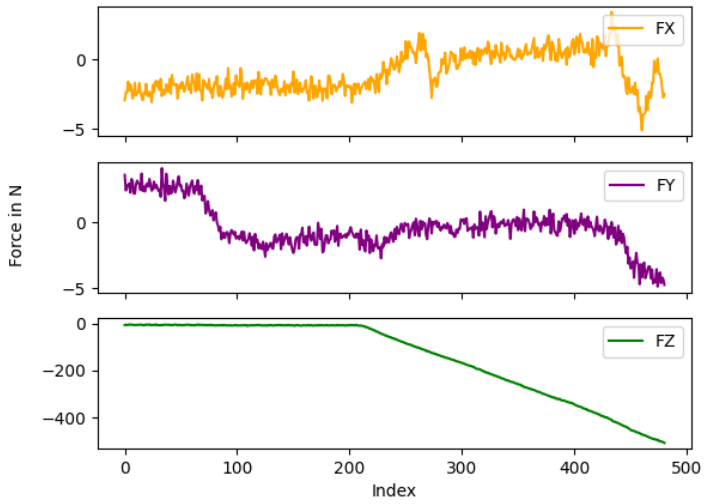

(b) Transverse forces in N in x- and y-direction (FX, FY) of the end-effector under load with the use of a force based correction. In addition, the occurring force in z-direction is also specified (FZ).

Figure 9.17. Deviation and transverse forces under load of the seat tube with the use of a camera based motion correction (a) and the force based motion correction (b).

9.3 Case Study 3: Snowboard

Like cycling sports, snowboarding necessitates equipment that emphasizes safety while accommodating a wide range of skill levels among participants. To achieve this goal, manufacturers craft snowboards using various materials and designs, allowing for adjustments in factors like flexibility, damping, weight, and cost. To ensure safety, optimal ride, handling characteristics, or sufficient strength, specialized mechanical testing procedures and test setups have been devised to test snowboards. Given snowboards' specific design and sandwich construction, they are pliable when subjected to bending and torsion, which contrasts starkly with rigid test objects such as tensile structures or bicycle frames. Consequently, this imparts a degree of complexity to testing motions, necessitating highly specialized testing setups, as elaborated in Section 3.2. This case study explores the extent of flexibility (RE 1) and precision (RE 6) achievable when employing robotic systems to execute these testing motions. Subsequent sections will delve deeply into the evaluation process, initially outlining the experimental test arrangement and the execution of tests. This involves utilizing the standardized test procedure developed earlier and utilizing the snowboard as previously described in Section 3.3.3. Ultimately, the ensuing sections will present and analyze the results gleaned from these experiments.

9.3.1 Experimental Setup

The first step of the standardized testing procedure was used to specify the robot-based testing facility experimental setup. In the preparation phase, the first step is the analysis of the snowboard. It has a sandwich construction and an overall length of $160\,\mathrm{cm}$ and a maximum width of $30\,\mathrm{cm}$. Therefore, it fits easily on the clamping area. The test consists of one loading point described in more detail in Section 3.3.3. The loading point is located at the nose of the snowboard. Since the snowboard deforms immense, it can not be mounted directly on the clamping field. Therefore, a clamping device was designed and manufactured from aluminum profiles attached to the clamping field (see Figure 9.18). The developed clamping devices connect the snowboard's binding firmly to the clamping device and can thus be used for any snowboard with the exact same binding mechanism. The appropriate end-effector for the robot bench must first be developed to apply the load to the snowboard. For this purpose, the same end-effector was used for the bending load (to keep the loading orthogonally on the snowboard surface) and for the combined load (bending and torsion). However, the end-effector was screwed tightly to the snowboard for the second case to allow torsion and consists of a simple plate with nuts that allows screwing. To screw the end-effectors together, a counterpart was mounted on the snowboard (named test tool in Figure 9.18). In this case dots were glued on to measure the displacements. The influence of the screws on the material properties can be left aside for this evaluation, as these are not the focus of this case study. Nevertheless, with a different end-effector design, this bolting can be avoided.

With all this information, the first step of the standardized test procedure is finished. The next step is the definition of the measuring technique. Analogous to the previous

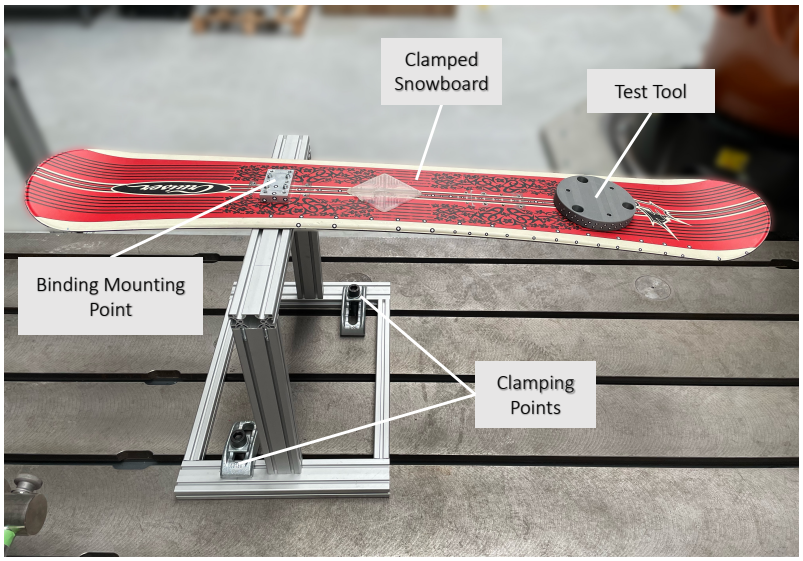

Figure 9.18. Clamped snowboard in the designed clamping device. The snowboard is attached via its binding to the clamping device and the clamping device is fixed on the clamping field via t-slot nuts and jaws.

use case, both available sensor systems will be used for these tests. The f/t-sensors were chosen to detect and record the forces and torques acting on the snowboard. The ATOS 5 was used as a second sensor to measure the snowboard displacements and the robot deviations. It was also equipped with an MV 1000 objective to ensure the largest possible image section. After defining the measurement technique, the next step is to define the motions. Two different test motions were chosen for the first load case (bending). The first was optical-based, and the second one was f/t-based. In the optical-based load case, the reference coordinate for the motion correction was placed in the snowboard so that it can be tracked by the ATOS 5 system and the bending can be corrected. For the torque-based motions, it was also specified for the control that the transverse torque (TY, TZ) should be controlled to zero. The same applies to the optical-based control, except that the absolute deviation in (lx, ly, lz, a, b, c) is controlled to zero. For the second load case (bending with torsion), one f/t-based test motion was selected. The given velocities and termination criteria for all motions can be taken from the problem definition of this case study (Table 3.3). The clamping device and the chosen robot end-effector give the orientation of the test motion. The test velocity in the z-direction determines the linear direction, and the control of the transverse forces generates a circular path that adapts to the deformation of the snowboard. The second velocity defines the rotation around the y-axis for the torsion motion, which is additionally applied to the direction in the z-axis. The motions are summarized in Table 9.6.

Load Case	**Regulation**	**Termination Crit.**	**Velocity**	Orientation
Bending	Optical	150 N	50 mm/min	a=101°, b=0.9°, c=−175°
Bending	F/T-Based	150 N	50 mm/min	a=101°, b=0.9°, c=−175°
Bending and Torsion	F/T-Based	150 N	50 mm/min bending and 10 mm/min torsion	a=101°, b=0.9°, c=−175°

Table 9.6. Overview over the snowboard test motions. Two test motions, one optical and one f/t-based, for load case one (bending) and one test motion for the second load case (bending and torsion) were chosen.

After defining the test motions, the corresponding motion sequences must be defined. Since only one test motion is executed here, no sequence is necessary. Similar to use case two (low forces), the position on the clamping field can be almost freely selected. Of course, it is also possible to specify a position with the help of the CASP approach. In the next step, the approach and departure motion must be defined. Since the focus is on the test motion, only one approach motion was selected to position the robot end-effector exactly above the counterpart of the snowboard in order to be able to screw it for the torque-regulated motions. In the optically controlled load case, the robot end-effector is not screwed to the counterpart on the snowboard. Figure 9.19 shows the final test setups for the next phase, the execution phase. The ATOS 5 was mounted on the second robot, and one robot executed the motions. The coordinate system's orientation in which the robot is controlled and all deviations are measured is also shown in the respective Figure. In the execution phase, the motions were executed until the (termination criteria) maximum forces were reached, and the data from the f/t-sensor and the ATOS 5 were aggregated and recorded. This will be discussed in the next section.

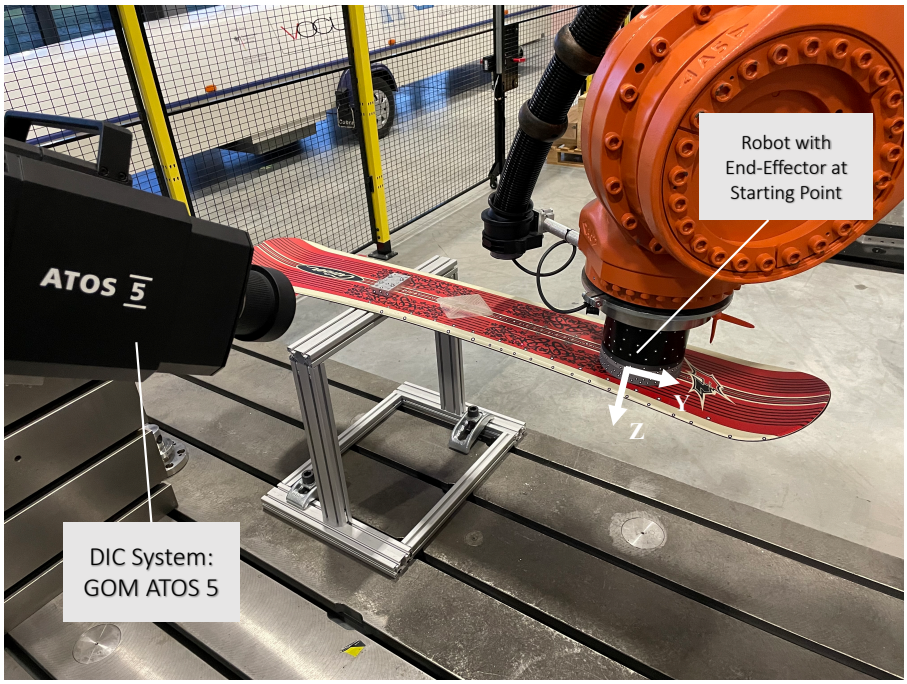

Figure 9.19. Overview of the final test setup for both load cases with the snowboard mounted on clamping field on the right side and the camera on the left side.

9.3.2 Analysis of the Results

This section discusses how far more complex and flexible test motions (RE 1) can be performed and how exactly these motions can be carried out. First, only the orthogonal load vector (bending) is considered, and then the superimposed load case is analyzed.

Bending
The graph shown in Figure 9.20 illustrates the lateral torques in Newton meter ($\mathrm{N\,m}$) and the displacement in millimeters (mm) of the end-effector during the application of a z-directional load on the snowboard, represented by the green line for the force and the blue, orange and purple line for the deviation in x,y,z-direction. This loading is conducted up to $150\,\mathrm{N\,m}$. The force is negative in this case because the sensor's internal coordinate system records the pressure in this direction (see Figure 9.19). Both scenarios show the actual testing motion is carried out, subjecting the snowboard to a load of up to $150\,\mathrm{N}$. The deviation between the two centers (end-effector and test-tool counterpart) varies between $0\,\mathrm{mm}$ and $0.1\,\mathrm{mm}$. This means that the end-effector follows the bending snowboard in this range since the reference coordinate system to which the deviation is measured was placed in the snowboard test tool. Regarding the torque-regulated test motion, the data shows the effective control of torques within a range of $1\,\mathrm{N\,m}$ for the y-axis. Furthermore, the x-axis shows that the torques settle around this axis at $4\,\mathrm{N\,m}$. Since the end-effector was screwed to the snowboard, a threshold was selected, and the

maximum in which no counter-regulation was applied was exactly at this threshold. It is conceivable that the torque cannot be reduced further due to the fixed clamping to the snowboard and the resulting residual stresses. Finally, the torques in the z-axis could be reduced to ± 2.5 N m. In conclusion, it can be deduced that if the test stamps are not screwed together (optical controlled), they lie loosely on top of each other and have the possibility of slipping or sliding off each other during the test.

Bending and Torsion

The chart depicted in Figure 9.21 portrays the lateral torques in Newton meter (N m) applied to the end-effector while subjecting the snowboard to a z-directional load (green) along with an additional torsional force around the y-axis (purple). The loading extends to 150 N. The force is presented as negative due to the sensor's internal coordinate system recording the pressure in this specific direction (as seen in Figure 9.19). This superimposed testing motion effectively demonstrates torque control within a range of 2 N m to 3 N m for the x-axis. As the end-effector was fastened to the snowboard, a threshold was determined, and the point at which no counter-regulation was applied precisely aligned with this threshold. It can be deducted that the torque might be challenging to decrease further due to the fixed attachment to the snowboard and the resultant residual stresses. The torques along the z-axis could be mitigated to approximately ± 2.5 N m. The overlay of motions in the z-direction becomes evident from the progressively increasing torque around the y-axis, reaching its zenith at around 15 N m. Consequently, it is demonstrated that both orthogonal conditions can be upheld, and this load can be augmented with torsion while rectifying the residual torque (TX).

In summary, the evaluation of the snowboard demonstrates the feasibility of conducting more complex test motions. This encompasses the adaptable application of standardized testing procedures and the execution of complex test motions, fulfilling the first requirement (RE 1). This was shown using two test motions (optical- and torque-controlled), which always managed to load the snowboard orthogonally, even though it was moving very far away. In addition, it was also shown that superimposed load cases are possible and that the shear forces and torques can be minimized here as well (RE 6).

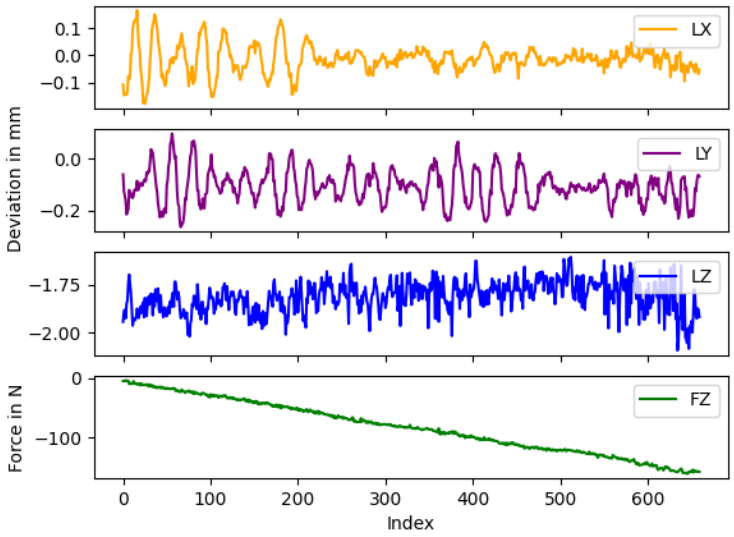

(a) Deviation in mm in x,y,z-direction (LX, LY, LZ) of the end-effector under load with the use of a camera based position correction, while the snowboard bends. In addition, the occurring force in z-direction is also specified (FZ).

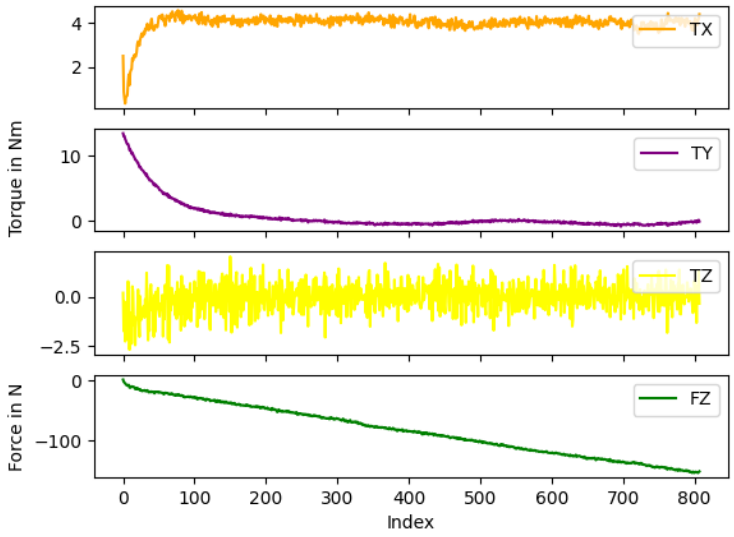

(b) Transverse torques in N m in x,y,z-direction (TX, TY, TZ) of the end-effector under load with the use of a torque based correction, while the snowboard bends. In addition, the occurring force in z-direction is also specified (FZ).

Figure 9.20. Deviation and transverse torques under load of the snowboard with the use of a camera based motion correction (a) and the torque based motion correction (b).

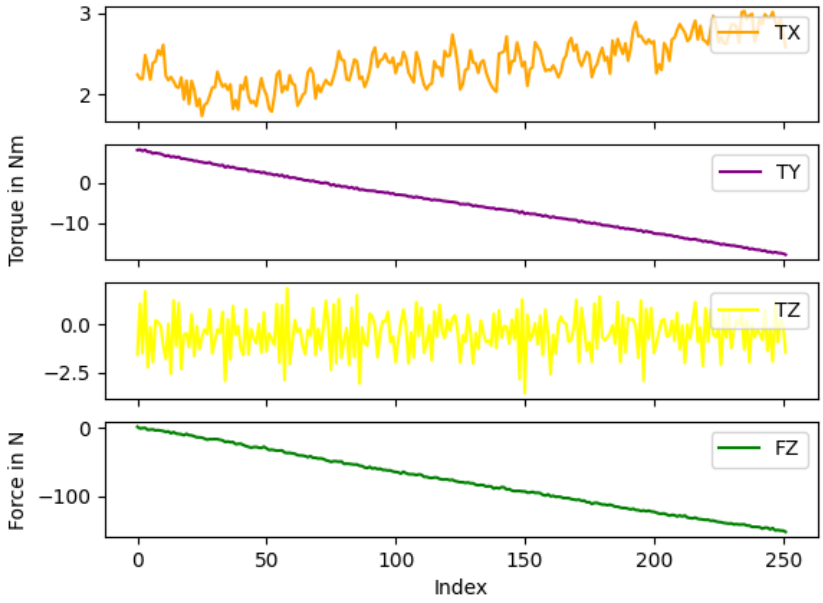

Figure 9.21. Overview of the transverse torques in N m in x-direction and z-direction (TX, TZ) of the end-effector under load with the use of a torque based correction, while the snowboard bends and torsions around the y-axis (TY). In addition, the occurring force in z-direction is also specified (FZ).

9.4 Case Study 4: Automotive Component

One vital part of a vehicle is the subframe, which, on the one hand, absorbs transmitted vibrations from the road or engine and, on the other hand, increases and optimizes the rigidity of the car body. Testing a subframe introduces additional complexities attributed to its intricate construction and multiple loading points that require simultaneous loading. This characteristic renders it fitting for the fourth case study. This case study will investigate whether testing with two robots is possible and how flexible (RE 1) and accurate (RE 6) the robots can perform test motions. For this, the following sections will delve deeper into the evaluation by describing first the experimental test setup and the test execution. This is performed using the developed standardized test procedure and the subframe already described in Section 3.4.3. This case study will also integrate the additional linear actuator (RE 2). Finally, the results obtained from the experiment will be presented.

9.4.1 Experimental Setup

The standardized testing procedure's first step was to specify the experimental setup of the robot-based testing facility. In the preparation phase, the first step is analyzing the subframe. The subframe is made of aluminum. It has the following dimensions:

96 cm length x 66 cm width x 26 cm height and fits easily on the clamping area. The test consists of three loading points described in more detail in Section 3.4.3. The first and the third loading point are located at the right pivot points of the subframe in the driving direction. The second loading point is located on the opposite side. With these load points, attaching the subframe directly to the clamping field is difficult because the frame has to withstand very high forces, and the clamping hardly makes this possible with the small contact surface that the frame offers. Therefore, a clamping device was designed and manufactured from clamping blocks and aluminum profiles (Item), which is attached to the clamping field (see Figure 9.22). The developed clamping uses the same mounting points for a secure hold that are also used for bolting the car's subframe. Moreover, the appropriate end-effectors for the robots and for the linear actuator must first be developed to apply the loads to the subframe. The respective subframe shape, which represents the wishbone shape, must be considered to create a form fit. Figure 9.23 shows the three different end-effectors for each loading point. The same numbering was chosen for the load points, e.g., the end-effector one is for the first load point. In this case, too, dots were glued on to measure the displacements.

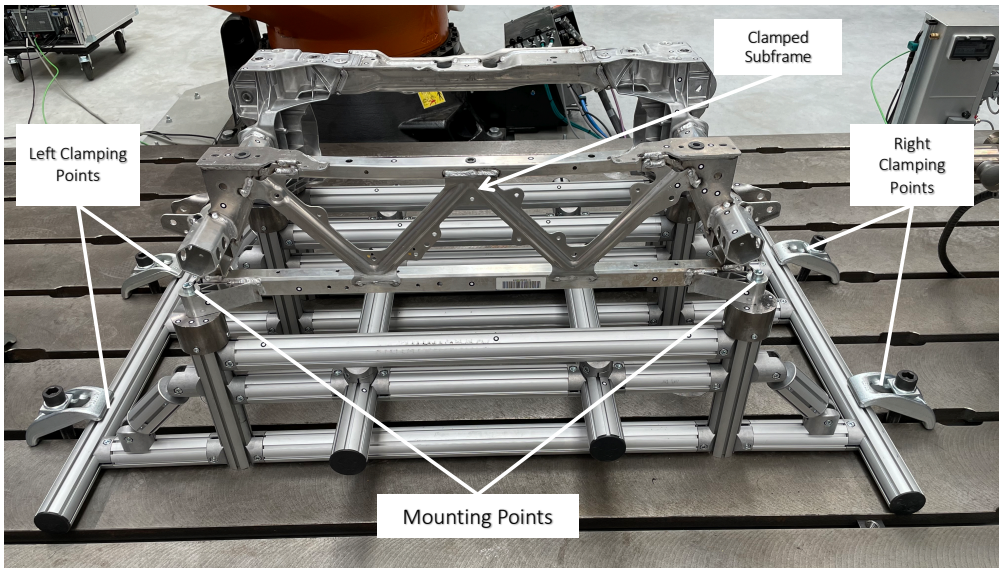

Figure 9.22. Clamped subframe in the designed clamping device. The subframe is attached via the same mounting points for a secure hold that are also used for bolting the car's subframe, The clamping device is connected to the clamping field via t-slot nuts and jaws.

With all this information, the first step of the standardized test procedure is finished. The next step is the definition of the measuring technique. Analogous to the previous use case, both available sensor systems will be used for these tests. The f/t-sensors were chosen to detect and record the forces and torques acting on the subframe. The ATOS 5 was used as a second sensor to measure the subframe displacements. It was also equipped with an MV 1000 objective to ensure the most extensive possible image section.

Figure 9.23. Developed end-effectors for the respective loading points on the subframe.

After the measuring technique definition is completed, the next step is to define the motions. Three different test motions were chosen, one for each loading point. Cases one and two should be torque-controlled, and the load point three should be force-controlled. In doing so, the two robots carry out load cases one and two, respectively, and the linear cylinder load case three. For the torque-based motions, it was also specified for the control that all transverse torques (tx, ty, tz) should be controlled to zero. The given velocities and termination criteria for all motions can be taken from the problem definition of this case study (Table 3.4). The clamping device and the chosen robot end-effector give the orientation of the test motion. The test velocity in the z-direction determines the linear direction in which the robot moves. The motions are summarized in Table 9.7.

Load Case	Regulation	Termination Crit.	Velocity	Orientation
1	Torque-based	5000 N	5 mm/min	a=89°, b=35°, c=95°
2	Torque-based	5000 N	−5 mm/min	a=89°, b=35°, c=−95°
3	Force-based	5000 N	5 mm/min	a=89°, b=35°, c=−95°

Table 9.7. Overview over the subframe test motions. Three test motions were chosen. Two torque-based motions were performed by the robots, and one force-based test motion was performed by the linear actuator.

After defining the test motions, the corresponding test motion sequence must be defined. No order is necessary since the test consists of only one test motion. However, it must be determined which robot performs which test movement. Here, robot one executes load case one, and robot two executes load case two. After specifying the motions and the motion sequence, the component placement is carried out with the help of the CASP

algorithm. The final component position is shown in 9.24. Since the focus is on the test motion, only two approach motions were chosen—one optical for the robots and one position-based for the linear actuator. Furthermore, a positioned-based motion was chosen as the departure motion. Figure 9.24 shows the final test setups for the next phase. The ATOS 5 was mounted on a tripod and aligned with the test object in this use case. The coordinate system's orientation in which the robot is controlled and all deviations are measured is also shown in the respective Figure. In the next phase, the approach motion was started, and then a break was taken to screw the end-effector to the subframe since the wishbones were also bolted on. After the approach motion, the test motions were executed until the (termination criteria) maximum forces were reached, and the data from the f/t-sensor and the ATOS 5 were aggregated and recorded. This will be discussed in the next section.

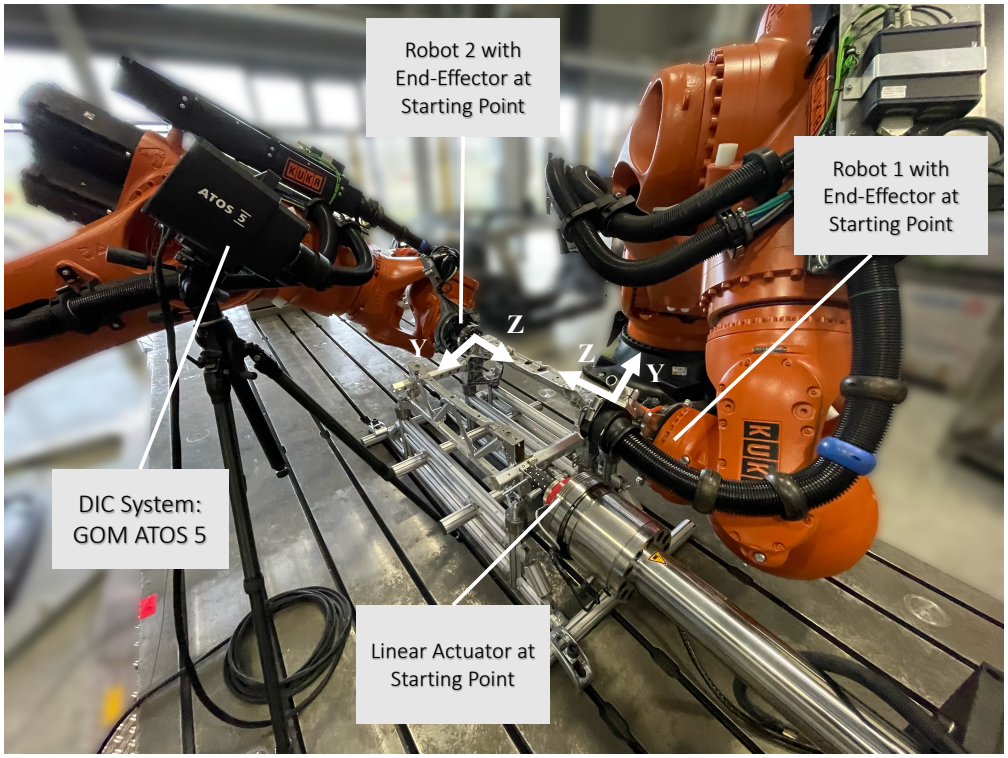

Figure 9.24. Overview of the final test setup for testing the subframes. The ATOS 5 was mounted on a tripod. The robots are and the linear actuator are positioned at their starting points.

9.4.2 Analysis of the Results

The chart depicted in Figure 9.25 shows the torques (TX, TY, TZ) and forces (FZ) occurring during the test of the subframe by both robots. The upper part (a) shows the forces and torques of robot one, and the lower part shows the forces and torques

of robot two. The loading extends to $5000\,\mathrm{N}$ for both robots. The force of robot two is presented as negative due to the sensor's internal coordinate system recording the pressure in this specific direction (as seen in Figure 9.24). The linear test cylinder is driven to load in parallel by its internal control system, which cannot be influenced further (as described in Section 8.4). The transverse torques of robot one reach their maximum of approximately $13\,\mathrm{N}$ in x-direction, at a maximum of approximately $-6\,\mathrm{N}$ in y-direction and at a maximum of approximately $-2.5\,\mathrm{N}$ in z-direction. The transverse torques of robot 2 reach their maximum of approximately $30\,\mathrm{N}$ in x-direction, at a maximum of approximately $-20\,\mathrm{N}$ in y-direction and at a maximum of approximately $-7\,\mathrm{N}$ in z-direction. This implies that the lateral torques can be effectively mitigated. Furthermore, this Figure shows that both robots start their test motion simultaneously and work synchronously. However, it's evident that the torque control was insufficiently precise, as the torques consistently rise with increasing force, particularly concerning the torque around the x-axis. In contrast, robot two compensated the torque around the y-axes very well. The origin of this effect is now being investigated in more detail.

Figure 9.26 shows the result of this optical measurement using the GOM Correlate software [28]. The direction of the strains can be displayed using arrows on the glued-on measuring points, and the corresponding strength in mm is determined using the color scale. Distortions occur, particularly at the test stamps themselves, indicating that the material used for 3D printing is too compliant. In this case, this also complicates the control since the end-effectors damp it. Furthermore, more significant strains can be observed in the rear part of the subframe. This can be deduced from the green arrows on the structure between the two robot test stamps. Displacements of up to $2.4\,\mathrm{mm}$ occur there. Maximum distortions of $3.61\,\mathrm{mm}$ occur in the entire test setup.

In summary, evaluating the subframe illustrates the practicability of conducting two simultaneous test motions. This includes the flexible utilization of standardized testing procedures and the execution of concurrent test motions, satisfying the requirement RE 1. This was demonstrated by employing one test motion for each robot. Although the test motions were exact again (RE 6), further examination is necessary to understand why the accuracy is slightly lower, and the deviations are higher than in the earlier case studies. Lastly, it was also demonstrated that integrating a third testing actuator into the overall control system can be achieved easily (RE 2).

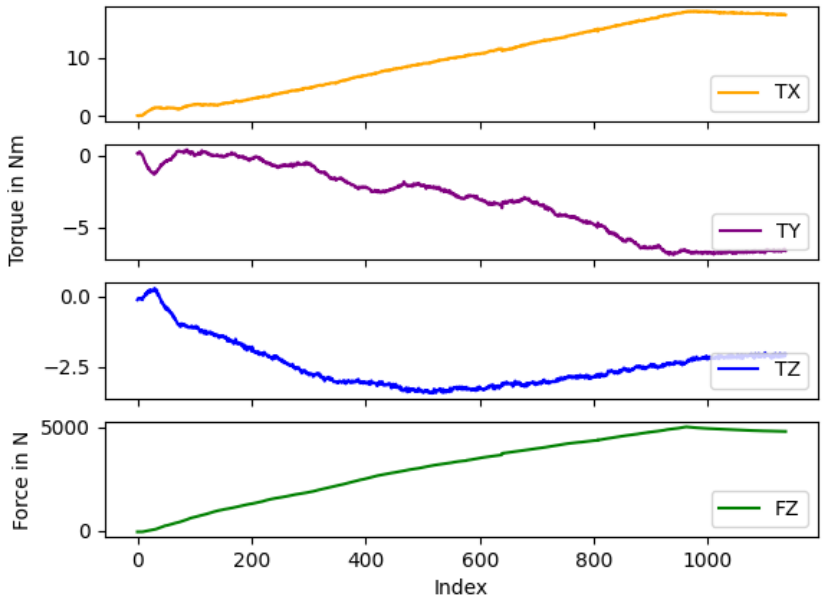

(a) Overview of the transverse torques in N m in x-direction, y-direction and z-direction (TX, TY, TZ) of robot one. In addition, the occurring force in z-direction is also specified (FZ).

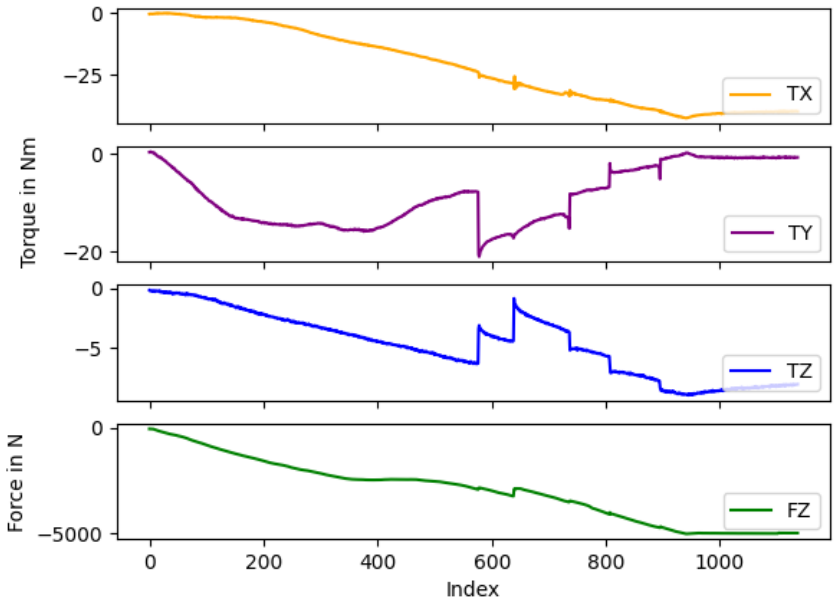

(b) Overview of the transverse torques in N m in x-direction, y-direction and z-direction (TX, TY, TZ) of robot two. In addition, the occurring force in z-direction is also specified (FZ).

Figure 9.25. Overview of the transverse torques in N m in x-direction, y-direction and z-direction (TX, TY, TZ) of the end-effectors under load with the use of a torque based correction for both robots.

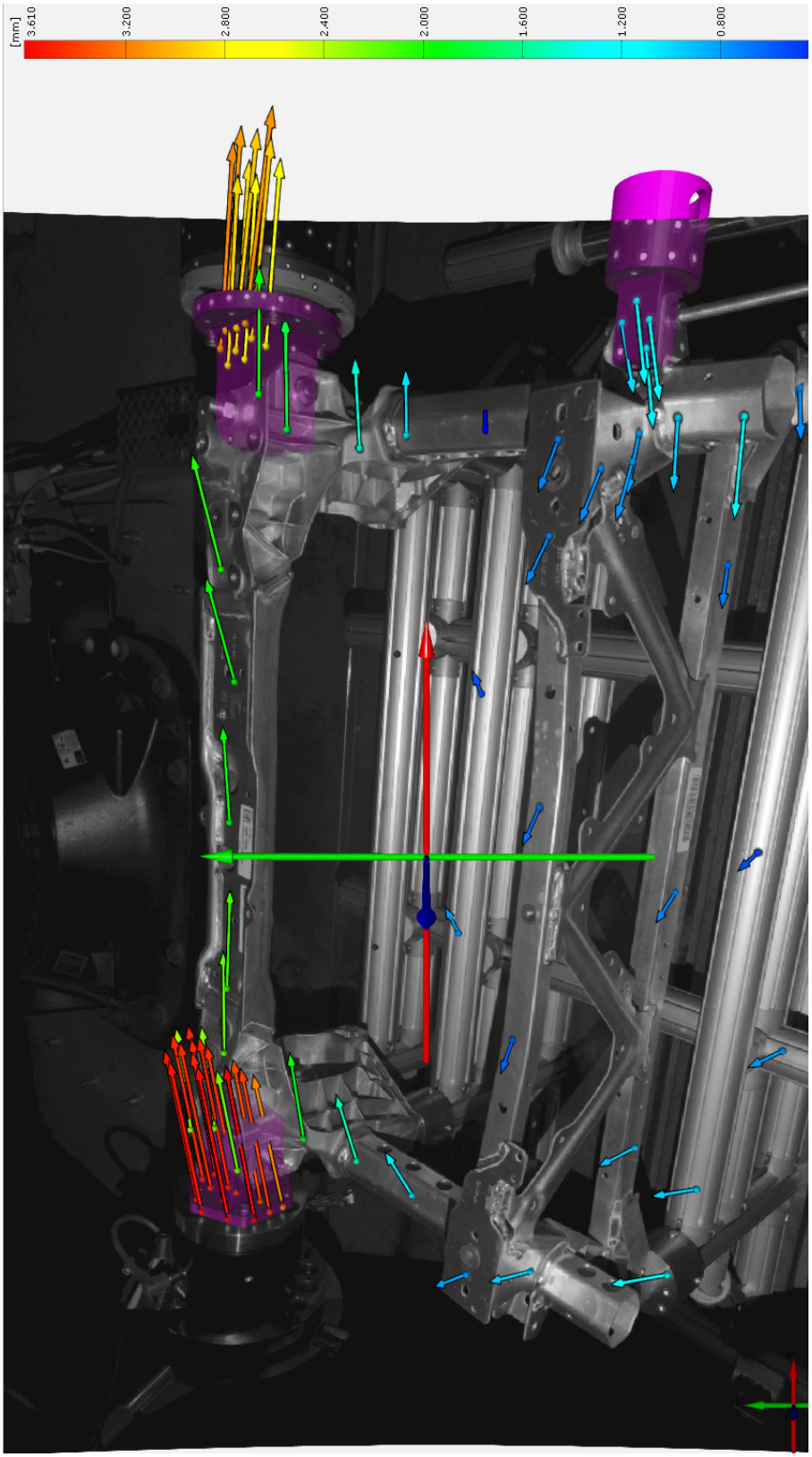

Figure 9.26. Strains in the subframe during the load case.

Summary. This chapter revisits and assesses the results achieved within the scope of this work. The thesis concludes with an outlook on possible further research questions, which deal with a higher degree of automation, hybrid regulation approaches, and the potential of future simulation environments.

10 Conclusion and Outlook

In this thesis, the initial questions are about which methods can be employed to enable the efficient and automated testing of intricate components using robots and how can the control system for the robot-based component test bench be programmed straightforwardly and intuitively. They were examined in detail and answered by presenting the general concept for software-defined robot-based component testing.

The results obtained are summarized and discussed in Section 10.1. An outlook on further research possibilities is given in Section 10.2.

10.1 Summary

To conduct automated and flexible destructive testing, there is a critical need for a versatile testing setup that can be tailored to various component tests. Industrial robots emerge as the ideal solution, offering unparalleled precision, repeatability, and adaptability. With their capability to move in six degrees of freedom (6 DOF) and cover a wide working range, these robots can execute diverse testing procedures. They can simulate real-world conditions, subject components to varying stresses, and efficiently perform intricate tests. Their agility and adaptability, driven by software rather than static hardware configurations, sets robot-based, software-defined test benches apart. These systems represent a significant shift in destructive testing, especially in Industry 4.0. Unlike conventional setups, these test benches are dynamic and flexible, allowing on-the-fly configuration adjustments through software. This dynamic approach to testing holds great promise for the manufacturing industry in the Industry 4.0 era.

With the presented approach for a software-defined robot-based testing facility and its concepts, this thesis makes an elementary contribution to enable the automation of flexible destructive component testing with industrial robots. This is made possible by a

suitable combination of several specially developed techniques and concepts, each of which addresses underlying problems in the overall context of robotics and destructive component testing. Chapter 3 presented four case studies, each with unique components and challenges for the test procedure. Classical component test setups are not able to address the requirements of all four components equally in a single test bench.

The foundation for enabling robot-based testing lies in developing and realizing a versatile facility. Chapter 4 provided an overview of such a testing facility, which was realized based on determined requirements. This was followed by a detailed description of the facility's layout, an exploration of the robots and their operational areas, and an examination of the incorporated sensors and actuators.

In addition to the physical implementation, there is a requirement for software systems which enable automated mechanical testing, effectively transforming versatile industrial robots into adaptable testing apparatuses. Since robot-based component testing is a relatively novel field, there is a scarcity of established practices and fundamental knowledge regarding software development in this domain. The standardized testing procedure presented in Chapter 5 defines this domain fundamentally and makes the complexity of robot-based destructive component testing manageable by dividing the overall approach into three phases: preparation, execution, and post-processing. In order to manage these three phrases on the software-defined testing bench, Chapter 5, also presented an overarching architecture concept. Moreover, this procedure ensures test reproducibility, serves as the foundation for the advanced concepts developed throughout this thesis, and is augmented by additional software concepts and algorithms for each phase developed as the work progresses.

The complexity of testing scenarios involves various motions and their precise sequences. Given that many robot controllers primarily handle basic motion commands, there is a need for a systematic approach to describing these movements and their sequences. In this context, Chapter 6 presented a modeling framework for robot-based testing motions and a model for organizing the execution sequence of such motions. The developed framework encompasses modeling three motion types: approach motions, which involve reaching the component, the testing motions themselves, and the departure motions that relocate the system away from the tested component.

In order to be able to perform the actual motions, the component must be placed on the test bench. Incorporating industrial robots into component testing adds complexities to positioning the test object. When placing the object for testing purposes, it is essential to consider the object's testing point reachability carefully. While robots offer greater flexibility compared to standard linear actuators, not every position on the test bench may be accessible. Moreover, industrial robots cannot apply the same forces and torques uniformly across all axis positions, even if a position is theoretically within reach. Consequently, it is necessary to calculate a position where the specimen can be tested and all required testing motions can be executed. Chapter 7 introduced an algorithmic approach for automated specimen placement named CASP: Computer Aided Specimen Placement for Robot-Based Component Testing. CASP includes a framework for mapping industrial robots' applicable forces and torques. Additionally, it

facilitates the execution of an automatic feasibility check for the required test motions and subsequently automates the specimen placement process.

Chapter 8 presented the concepts for implementing the second phase of the standardized testing procedure, the execution phase. This includes a flexible architecture for integrating robots, actuators, and sensors via standardized interfaces. Furthermore, it described the implementation concepts and details for the actual motion execution.

The case studies introduced in Chapter 3 were revisited in Chapter 9 to apply and evaluate the results of this thesis in four different use cases. Assessing the suitability of robots for flexible destructive component testing is a novel application area. To make an informed determination regarding the feasibility of employing robots in this domain, it is essential to evaluate a relevant and comparable case study. Therefore, the first case study presented in Chapter 9 was a basic feasibility check. A tensile test setup on a conventional testing machine and the same setup on a robot-based test bench were compared. The achieved results showed the feasibility of robot-based component testing in principle. In addition to this basic comparison, three further case studies with different components (bicycle frame, snowboard, and automotive component) were evaluated. Overall, the case studies showed that the developed control system compensates for inherent robot deformations and enables the flexible execution of different test motions at slow velocities, in different positions, with simultaneous execution, and at high forces. Additionally, it ensures consistent and repeatable motions for enhanced reproducibility, complemented by utilizing the developed standardized test procedure.

In summary, this thesis presented a holistic approach for software-defined robot-based component testing, which enables the flexible and automated destructive testing of various components using industrial robots.

10.2 Outlook

The domain of robot-based component testing on software-defined test benches is vast and presents numerous unresolved research questions. While the approach presented in this thesis provides a comprehensive and self-contained method for robot-based component testing, it still offers opportunities for further exploration in various aspects.

To further advance the capabilities of the flexible, software-defined robot-based test bench approach, automating the entire process of deriving component tests offers a compelling avenue for exploration and development. In this envisioned scenario, a test engineer would be equipped with a specialized editor as a step-by-step guide through the developed standardized testing procedure. Throughout this streamlined process, the test engineer would commence by conducting a comprehensive component analysis, leveraging the power of CAD (Computer-Aided Design) tools to create a detailed model of the specific component to be tested. Within this digital environment, the engineer could input and fine-tune all the critical parameters and specifications essential for the component's examination. These inputs might include identifying loading points and detailed instructions on how the component should undergo testing at the designated points. After the meticulous input of these testing parameters, an extension to the developed architecture would come into play, orchestrating the automatic generation

of all requisite motions, spanning from the initial approach to the testing phase and culminating in the departure sequence. Concurrently, the system would also calculate the precise positioning of the component on the test bench, optimizing its placement for the upcoming assessments. The comprehensive set of instructions and data would be seamlessly transmitted to the robot-based test bench after this automated preparation. With this information, the test bench would execute the entire testing procedure with high degree of automation. The robot's movements, the application of forces and torques, and the data collection processes would all be orchestrated harmoniously to ensure precision and consistency in the testing process. Furthermore, this advanced approach would empower the engineer to define the testing parameters and specify the desired performance criteria for the component at each testing point. This critical information would be the basis for evaluating the component's performance. As the testing procedures are carried out, the system automatically collects and processes the data, comparing it against the predefined performance criteria. Consequently, the results would allow analyzing the component's performance in each time step.

So far, two types of control (f/t-based and optical-based) have been considered in this thesis. In order to make the robot-based test bench even more flexible, further types of control would be conceivable. Integrating hybrid regulation methods that combine force/torque-based sensing with optical systems could bring advancements. Combining force/torque sensing with optical systems such as 3D vision enables robots to have a multi-dimensional view of the component under test. This data fusion provides enhanced sensing and perception capabilities, allowing robots to detect changes, defects, or deviations that individual sensing methods may miss. This will empower the testing mechanism with more dynamic adaptation capabilities. When deviations or irregularities are detected optically, the robot can, e.g., instantly adjust its force and motion to compensate for these irregularities and vice versa. Furthermore other hybrid types of regulation are also conceivable. Robots could perform complex tests by combining classical control techniques, which provide stability and reliability, with learning-based approaches, which adapt to varying conditions. This adaptability is especially valuable when dealing with components that have complex or unpredictable behaviors. The integration of AI-driven algorithms would allow optimizing the testing procedures. It can, for example, learn from previous test runs, and the motions could be adjusted to achieve the desired outcomes more efficiently. This reduces, e.g., the testing time. While hybrid regulation methods offer immense potential, there are a lot of challenges to overcome, such as ensuring the reliability of AI-driven algorithms and addressing safety concerns in autonomous testing scenarios.

In the future, more advanced robotics simulations could offer even more benefits within the simulation of robot-based component testing. Currently FEM simulations are used to forecast component behavior under various conditions, empowering engineers to preemptively address potential challenges before physical testing, thus diminishing the requirement for expensive prototypes. Integrating physical component behavior into robotic simulation has the potential to enhance precision and foresight for the motion planing significantly. Furthermore can the integration of live data into simulations facilitate adjustments and optimization of test scenarios, streamlining the testing process.

Such data can also accelerate the identification of critical test parameters in pre-analysis and post-analysis.

Moreover, there is potential for expanding the testing facility itself. Integrating more powerful robots and additional sensors within this expanded space can enhance the effectiveness and efficiency of robot-based component testing. Including more sensors can yield a more comprehensive and detailed dataset during and after testing, facilitating a more thorough analysis of the component's performance and behavior. At runtime additional sensor data such as from a laser tracker can be employed to increase the robots' positional accuracy. More powerful robots, on the other hand, can manage heavier loads and execute tests that demand greater force or torque. This expanded testing capability broadens the scope for evaluating components under more rigorous conditions, ensuring their resilience across diverse operational scenarios.

Bibliography

[1] Alpine skis - Determination of elastic properties. Standard DIN EN 5902:2013-09, DIN Deutsches Institut für Normung e. V., Berlin, DE, 2013.

[2] Standard Terminology Relating To Snowboardings. Standard ASM F1107-04(2021), ASTM International, 100 Barr Harbor Drive, West Conshohocken, PA 19428-2959 USA„ 2016.

[3] Standard Test Methods for Bicycle Forks. Standard ASTM F 2273:2016, ASTM International, 100 Barr Harbor Drive, West Conshohocken, PA 19428-2959 USA„ 2016.

[4] Standard Test Methods for Bicycle Frames. Standard ASTM F 2211:2019, ASTM International, 100 Barr Harbor Drive, West Conshohocken, PA 19428-2959 USA„ 2019.

[5] Cycles - Safety requirements for bicycles. Standard DIN EN 4210:2023, DIN Deutsches Institut für Normung e. V., Berlin, DE, 2019.

[6] Plastics — Determination of tensile properties – Part 1: General principles. Standard DIN EN 527-1:1996, DIN Deutsches Institut für Normung e. V., Berlin, DE, 2019.

[7] Metallic materials – Tensile testing – Part 1: Method of test at room temperature. Standard DIN EN 6892-1:2019, DIN Deutsches Institut für Normung e. V., Berlin, DE, 2019.

[8] Ieee standard for a precision clock synchronization protocol for networked measurement and control systems. *IEEE Std 1588-2019 (Revision ofIEEE Std 1588-2008)*, 2020. doi: 10.1109/IEEESTD.2020.9120376.

[9] Robots and robotic devices — Vocabulary. Standard DIN EN 8373:2021, International Organization for Standardization, Geneva, C, 2021.

[10] ABB Asea Brown Boveri Ltd. 3D Quality Inspection In-line, 2023. URL `https://new.abb.com/products/robotics/functional-modules/3dqi-in-line`. (accessed on 12.06.2023).

[11] ABB Asea Brown Boveri Ltd. Integrated Force Control, 2023. URL `https://new.abb.com/products/robotics/application-equipment-and-accessories/integrated-force-control`. (accessed on: 09.08.2023).

[12] ABB Asea Brown Boveri Ltd. RobotStudio, 2023. URL `https://new.abb.com/products/3HAC031177-001/robotstudio`. (accessed on: 09.08.2023).

[13] M. Abdullah, H. Roth, M. Weyrich, J. Wahrburg, and A. Lakshm. Evaluation of online-guiding software platforms for sensor integration with industrial robot controller over ethernet network. *International Journal of Materials, Mechanics and Manufacturing*, 4: 171–174, 01 2015. doi: 10.7763/IJMMM.2016.V4.249.

[14] T. Abrahamsson and D. Kammer. Finite element model calibration using frequency responses with damping equalization. *Mechanical Systems and Signal Processing*, 62-63, 03 2015. doi: 10.1016/j.ymssp.2015.02.022.

[15] K. Alemzadeh and D. Raabe. Prototyping Artificial Jaws for the Bristol Dento-Munch Robo-Simulator; 'A parallel robot to test dental components and materials'. In *2007 29th Annual International Conference of the IEEE Engineering in Medicine and Biology Society*, pages 1453–1456, 2007. doi: 10.1109/IEMBS.2007.4352574.

[16] H.-J. Bargel and G. Schulze. *Werkstoffkunde*. Springer-Verlag, 2008.

[17] Batz+Burgel GmbH. Stahl-Halbzeug Edelstahl V2A (1.4301), 2023. URL https://batz-burgel.com/metallhandel/lieferant-stahl/edelstahl-v2a/. (accessed on: 25.09.2023).

[18] A. K. Bedaka, J. Vidal, and C.-Y. Lin. Automatic robot path integration using three-dimensional vision and offline programming. *The International Journal of Advanced Manufacturing Technology*, 102:1–16, 06 2019. doi: 10.1007/s00170-018-03282-w.

[19] F. Beeh and H. Wörn. Occubot vi - an intelligent robot system for seat testing applications. In *Intelligent Autonomous Systems 7*, pages 26–29. IOS Press, 2002.

[20] H. Bhatkar, R. Dakshinamoorthy, V. B., and N. Vijayakumar. Simulating human body touch automotive tests using industrial robot and intelligent grippers equipped with sensors. 11 2013. doi: 10.4271/2013-01-2823.

[21] A. Bindauf, C. Angrick, and G. Prokop. Fahrwerkscharakterisierung an einem hochdynamischen achsprüfstand. *ATZ - Automobiltechnische Zeitschrift*, 116:76–81, 12 2014. doi: 10.1007/s35148-014-2016-4.

[22] R. Bogue. The role of robotics in non-destructive testing. *Industrial Robot: An International Journal*, 37(5):421–426, 2010.

[23] F. Bolourchi. Bicycle frame stresses by means of finite element analysis. *American Society of Mechanical Engineers, Design Engineering Division (Publication) DE*, 1:25–28, 01 1986.

[24] C. Borsellino, L. Calabrese, R. Passari, and A. Valenza. *Study of Snowboard Sandwich Structures*, pages 967–976. 01 2005. ISBN 1-4020-3444-X. doi: 10.1007/1-4020-3848-8_97.

[25] K. Buffinton, S. Shooter, I. Thorpe, and J. Krywicki. Laboratory, computational and field studies of snowboard dynamics. *Sports Engineering*, 6:129–137, 01 2003. doi: 10.1007/BF02859890.

[26] B. Caillaud and J. Gerstmayr. Shape optimization of a snowboard sidecut geometry. *Sports Engineering*, 25, 09 2022. doi: 10.1007/s12283-022-00380-7.

[27] B. Caillaud, R. Winkler, M. Oberguggenberger, M. Luger, and J. Gerstmayr. Static model of a snowboard undergoing a carved turn: validation by full-scale test. *Sports Engineering*, 22, 06 2019. doi: 10.1007/s12283-019-0307-4.

[28] Carl Zeiss GOM Metrology GmbH. IGOM Correlate Pro, 2023. URL https://www.gom.com/en/products/zeiss-quality-suite/gom-correlate-pro. (accessed on: 04.09.2023).

[29] S. Caro, C. Dumas, S. Garnier, and B. Furet. Workpiece placement optimization for machining operations with a kuka kr270-2 robot. In *2013 IEEE International Conference on Robotics and Automation*, pages 2921–2926, 2013. doi: 10.1109/ICRA.2013.6630982.

[30] S. Cavalieri and F. Chiacchio. Analysis of opc ua performances. *Computer Standards & Interfaces*, 36(1):165–177, 2013. ISSN 0920-5489. doi: https://doi.org/10.1016/j.csi.2013.06.004. URL https://www.sciencedirect.com/science/article/pii/S0920548913000640.

[31] S. Chellamuthu and M. Ali. Experimental study on tensile behavior of multi wall carbon nanotube reinforced epoxy composites. *Journal of Applied Sciences Research*, 8:3253–3259, 07 2012.

[32] Y. Cheng, C. Lee, and M.-T. Tsai. Multi-objective optimization of an on-road bicycle frame by uniform design and compromise programming. *Advances in Mechanical Engineering*, 8, 02 2016. doi: 10.1177/1687814016632985.

[33] P. Clifton, A. Subic, and A. Mouritz. Snowboard stiffness prediction model for any composite sandwich construction. *Procedia Engineering*, 2:3163–3169, 06 2010. doi: 10.1016/j.proeng.2010.04.127.

[34] T. W. Clyne and J. E. Campbell. *Tensile Testing*, page 81–106. Cambridge University Press, 2021. doi: 10.1017/9781108943369.006.

[35] D. Covill, S. Begg, E. Elton, M. Milne, R. Morris, and T. Katz. Parametric finite element analysis of bicycle frame geometries. *Procedia Engineering*, 72:441–446, 2014. ISSN 1877-7058. doi: https://doi.org/10.1016/j.proeng.2014.06.077. URL https://www.sciencedirect.com/science/article/pii/S1877705814005931. The Engineering of Sport 10.

[36] R. Damasevicius, R. Maskeliunas, G. Narvydas, R. Narbutaite, D. Połap, and M. Woźniak. Intelligent automation of dental material analysis using robotic arm with jerk optimized trajectory. *Journal of Ambient Intelligence and Humanized Computing*, 11, 12 2020. doi: 10.1007/s12652-020-02605-8.

[37] Dassault Systems. Delmia, 2023. URL https://www.3ds.com/products/delmia/portfolio. (accessed on: 09.08.2023).

[38] J. Davis. *Tensile Testing*. ASM International, 12 2004. ISBN 978-1-62708-355-3. doi: 10.31399/asm.tb.tt2.9781627083553. URL https://doi.org/10.31399/asm.tb.tt2.9781627083553.

[39] Department of faculty 3mE, TU Delft. Biaxial tester, 2023. URL https://www.tudelft.nl/3me/over/afdelingen/maritime-and-transport-technology/research/ship-and-offshore-structures/facilities/biaxial-tester. (accessed on 25.06.2023).

[40] Department of faculty 3mE, TU Delft. Hexapod, 2023. URL https://www.tudelft.nl/3me/over/afdelingen/maritime-and-transport-technology/research/ship-and-offshore-structures/facilities/hexapod. (accessed on 25.06.2023).

[41] H. Derhamy, J. Rönnholm, J. Delsing, J. Eliasson, and J. van Deventer. Protocol interoperability of opc ua in service oriented architectures. In *2017 IEEE 15th International Conference on Industrial Informatics (INDIN)*, pages 44–50, 2017. doi: 10.1109/INDIN.2017.8104744.

[42] B. Devaiah, R. Purohit, R. Rana, and V. Parashar. Stress analysis of a bicycle frame. *Materials Today: Proceedings*, 5(9, Part 3):18920–18926, 2018. ISSN 2214-7853. doi: https://doi.org/10.1016/j.matpr.2018.06.241. Materials Processing and characterization, 16th – 18th March 2018.

[43] E. Doebelin. *Measurement Systems: Application and Design*. McGraw-Hill Mechanical Engineering Series. McGraw-Hill, 1990. ISBN 9780070173385. URL https://books.google.de/books?id=9NtSAAAAMAAJ.

[44] R. Dosil, X. M. Pardo, X. R. Fdez-Vidal, A. García-Díaz, and V. Leborán. A new radial symmetry measure applied to photogrammetry. *Pattern Analysis and Applications*, 16: 637–646, 2013.

[45] J.-M. Drouet and Y. Champoux. Development of a three-load component instrumented stem for road cycling. *Procedia Engineering*, 34:502–507, 12 2012. doi: 10.1016/j.proeng.2012.04.086.

[46] M. Ersoy and S. Gies. *Fahrwerkhandbuch: Grundlagen – Fahrdynamik – Fahrverhalten– Komponenten – Elektronische Systeme – Fahrerassistenz – Autonomes Fahren– Perspektiven*. 01 2017. ISBN 96-135, 233-235, 374, 544-590, 591-596. doi: 10.1007/978-3-658-15468-4.

[47] M. Filipenko, A. Poeppel, A. Hoffmann, W. Reif, A. Monden, and M. Sause. Virtual commissioning with mixed reality for next-generation robot-based mechanical component testing. In *ISR 2020; 52th International Symposium on Robotics*, pages 1–6, 2020.

[48] J. Fraden. *Handbook of Modern Sensors: Physics, Designs, and Applications*.

[49] J. Fu, X. Xu, J. Li, D. Ma, and D. Yu. *Optimization of Subframe Mounting System to Reduce the Interior Booming*, pages 521–533. 11 2013. ISBN 978-3-642-33831-1. doi: 10.1007/978-3-642-33832-8_40.

[50] Giant Bicycles. The truth about road frame testing, 2013. URL `https://www.giant-bicycles.com/_upload/showcases/2013/TCR_FrameTestingData.pdf`. (accessed on: 29.06.2023).

[51] J. Gotlih, T. Karner, K. Gotlih, and B. Miran. Accuracy improvement of robotic machining based on robot's structural properties. *The International Journal of Advanced Manufacturing Technology*, 108, 05 2020. doi: 10.1007/s00170-020-05438-z.

[52] D. Grewal, C. Lund, E. Rossetter, and S. Dean. Experimental measurement of selected snowboard mechanical properties. *Journal of Astm International*, 3, 01 2006. doi: 10.1520/JAI14194.

[53] S. Gul, J. Shiriyev, V. Singhal, O. Erge, and C. Temizel. Chapter three - advanced materials and sensors in well logging, drilling, and completion operations. In C. Temizel, M. M. Sari, C. H. Canbaz, L. A. Saputelli, and O. Torsæter, editors, *Sustainable Materials for Oil and Gas Applications*, volume 1 of *Advanced Materials and Sensors for the Oil and Gas Industry*, pages 93–123. Gulf Professional Publishing, 2021. ISBN 978-0-12-824380-0. doi: https://doi.org/10.1016/B978-0-12-824380-0.00004-9. URL `https://www.sciencedirect.com/science/article/pii/B9780128243800000049`.

[54] J. Hanke, C. Eymüller, A. Poeppel, J. Reichmann, A. Trauth, M. Sause, and W. Reif. Sensor-guided motions for robot-based component testing. In D. Brugali, P. C.-Y. Sheu, and J. Tsai, editors, *2022 Sixth IEEE International Conference on Robotic Computing (IRC), 5-7 December 2022, Naples, Italy*, pages 81 – 84, 2022. doi: 10.1109/irc55401.2022.00021.

[55] J. Hanke, C. Eymüller, J. Reichmann, A. Trauth, M. Sause, and W. Reif. Software-defined testing facility for component testing with industrial robots. In *2022 IEEE 27th International Conference on Emerging Technologies and Factory Automation (ETFA)*, pages 1–8, 2022. doi: 10.1109/ETFA52439.2022.9921625.

[56] J. Hanke, M. S. Matthias, C. Eymüller, M. E. Müller, A. Poeppel, and W. Reif. Casp: Computer aided specimen placement for robot-based component testing. In *Proceedings of the 20th International Conference on Informatics in Control, Automation and Robotics (ICINCO)*, pages 374–382, 2023. doi: 10.5220/0012155000003543.

[57] K. Harada, T. Tsuji, K. Nagata, N. Yamanobe, and H. Onda. Validating an object placement planner for robotic pick-and-place tasks. *Robotics and Autonomous Systems*, 62(10):1463–1477, 2014. ISSN 0921-8890. doi: https://doi.org/10.1016/j.robot.2014.05.014. URL `https://www.sciencedirect.com/science/article/pii/S0921889014001092`.

[58] J. A. Haustein, K. Hang, J. Stork, and D. Kragic. Object placement planning and optimization for robot manipulators. In *2019 IEEE/RSJ International Conference on Intelligent Robots and Systems (IROS)*, pages 7417–7424. IEEE, 2019.

[59] M. Hull and F. BOLOURCHI. Contributions of rider-induced loads to bicycle frame stress. *Journal of Strain Analysis for Engineering Design - J STRAIN ANAL ENG DESIGN*, 23: 105–114, 07 1988. doi: 10.1243/03093247V233105.

[60] IEC TR 62541-1. OPC Unified Architecture: Overview and Concepts. Standard, International Organization for Standardization, 2020.

[61] IEC TR 62541-14. OPC Unified Architecture - Part 14: PubSub. Standard, International Organization for Standardization, 2020.

[62] IEC TR 62541-4. OPC Unified Architecture - Part 4: Services. Standard, International Organization for Standardization, 2020.

[63] IEC TR 62541-5. OPC Unified Architecture - Part 5: Information Mod. Standard, International Organization for Standardization, 2020.

[64] ISO 9283:1998. Manipulating industrial robots - Performance criteria and related test methods. Standard, 1998.

[65] D. Jansen and H. Buttner. Real-time ethernet: the ethercat solution. *Computing and Control Engineering*, 15(1):16–21, 2004.

[66] C. Ji, J.-K. Na, Y.-S. Lee, Y.-D. Park, and M. Kimchi. Robot-assisted non-destructive testing of automotive resistance spot welds. *Welding in the World*, 65:1–8, 10 2020. doi: 10.1007/s40194-020-01002-1.

[67] M. Karkun and S. Dharmalingam. 3d printing technology in aerospace industry – a review. *International Journal of Aviation, Aeronautics, and Aerospace*, 01 2022. doi: 10.15394/ijaaa.2022.1708.

[68] M. Kebbach, R. Grawe, A. Geier, E. Winter, P. Bergschmidt, D. Kluess, D. D'Lima, C. Woernle, and R. Bader. Effect of surgical parameters on the biomechanical behaviour of bicondylar total knee endoprostheses – a robot-assisted test method based on a musculoskeletal model. *Scientific Reports*, 9:1–11, 10 2019. doi: 10.1038/s41598-019-50399-3.

[69] K. Khutal, G. Kathiresan, K. Ashok, B. Simhachalam, and D. Jebaseelan. Design validation methodology for bicycle frames using finite element analysis. *Materials Today: Proceedings*, 22:1861–1869, 01 2020. doi: 10.1016/j.matpr.2020.03.085.

[70] U. Kim, D.-H. Lee, Y. B. Kim, D.-Y. Seok, and H. R. Choi. A novel six-axis force/torque sensor for robotic applications. *IEEE/ASME Transactions on Mechatronics*, 22(3):1381–1391, 2017. doi: 10.1109/TMECH.2016.2640194.

[71] A. Kohlstedt, S. Olma, P. Traphöner, K.-P. Jäker, and A. Trächtler. Kinematics-based force/position control of a hexapod in a hil axle test rig. In M. Bargende, H.-C. Reuss, and J. Wiedemann, editors, *17. Internationales Stuttgarter Symposium*, pages 1217–1230, Wiesbaden, 2017. Springer Fachmedien Wiesbaden.

[72] K. Kraus. *Photogrammetrie, 7. Auflage*. Berlin, Germany: Walter de Gruyter Verlag, 2004.

[73] L. Kuczek, P. Marczak, W. Muzykiewicz, M. Mroczkowski, P. Packo, and D. Drop. Research on an innovative flex bicycle frame with a softtail vibration damping system. *Advances in Science and Technology Research Journal*, 17:290–303, 02 2023. doi: 10.12913/22998624/159041.

[74] H. A. Kuhn and D. Medlin. *Mechanical testing and evaluation*, volume 8. ASM international Material Park, OH, USA, 2000.

[75] KUKA AG. KR 1000 titan, 2023. URL `https://www.kuka.com/en-de/products/robot-systems/industrial-robots/kr-1000-titan`. (accessed on: 16.05.2023).

[76] KUKA AG. KR C4, 2023. URL `https://www.kuka.com/de-de/produkte-leistungen/robotersysteme/robotersteuerungen/kr-c4`. (accessed on: 16.05.2023).

[77] KUKA AG. Application and robot programming, 2023. URL https://www.kuka.com/en-de/services/engineering/application-and-robot-programming. (accessed on: 16.05.2023).

[78] KUKA AG. KUKA Robot Selector, 2023. URL https://www.kuka.com/en-de/products/robot-systems/software/cloud-software/kuka-robot-selecto.

[79] KUKA AG. KUKA OccuBot: the intelligent test system, 2023. URL https://www.kuka.com/en-de/products/robot-systems/ready2_use/occubot. (accessed on: 16.05.2023).

[80] KUKA AG. KUKA.EtherNet KRL – The control system of the future KR C4, 2023. URL https://www.kuka.com/-/media/kuka-downloads/imported/87f2706ce77c4318877932fb36f6002d/kuka_pb_controllers_en.pdf?rev=e8d133f6ddc64b3cb5329645eea0cc8e&hash=90B1C2377022BEC4AA9EAF67B28F5735. (accessed on: 09.08.2023).

[81] KUKA AG. KUKA.ForceTorqueControl, 2023. URL https://www.kuka.com/en-de/products/robot-systems/software/application-software/kuka-forcetorquecontrol. (accessed on: 09.08.2023).

[82] KUKA AG. KUKA.RobotSensorInterface, 2023. URL https://www.kuka.com/en-de/products/robot-systems/software/application-software/kuka_robotsensorinterface. (accessed on: 09.08.2023).

[83] KUKA AG. KUKA.Sim, 2023. URL https://www.kuka.com/en-de/products/robot-systems/software/planning-project-engineering-service-safety/kuka_sim. (accessed on: 09.08.2023).

[84] E. Kus, R. Gruninger, and R. Huppi. Integration of intelligent sensors for sensor-guided motions in industrial robot applications. pages 1480 – 1485, 10 2008. doi: 10.1109/ICAL.2008.4636387.

[85] J.-H. Kwon and D. Lee. Variability analysis of vibrational responses in a passenger car considering the uncertainties of elastomers. *Proceedings of the Institution of Mechanical Engineers, Part C: Journal of Mechanical Engineering Science*, 230, 10 2015. doi: 10.1177/0954406215612816.

[86] A. Köllner, C. Cameron, and M. Battley. Measurement and analysis system for bicycle field test studies. *Procedia Engineering*, 72:350–355, 12 2014. doi: 10.1016/j.proeng.2014.06.061.

[87] H. Lasi, R. Fettke, H. Kemper, T. Feld, and M. Hoffman. Application-Pull and Technology-Push as Driving Forces for the Fourth Industrial Revolution. *Business & information systems engineering*, 6:239–242, 2014.

[88] J. Lee. Apply force/torque sensors to robotic applications. *Robotics*, 3(2):189–194, 1987. ISSN 0167-8493. doi: https://doi.org/10.1016/0167-8493(87)90007-6. URL https://www.sciencedirect.com/science/article/pii/0167849387900076. Special Issue: Sensors.

[89] J. Liao. Fatigue test and analysis on subframe in fuel cell car. *Advanced Materials Research*, 472-475:1915–1920, 02 2012. doi: 10.4028/www.scientific.net/AMR.472-475.1915.

[90] Z.-Y. Liao, Q.-H. Wang, H.-L. Xie, J.-R. Li, X.-F. Zhou, and T.-H. Pan. Optimization of robot posture and workpiece setup in robotic milling with stiffness threshold. *IEEE/ASME Transactions on Mechatronics*, 27(1):582–593, 2022. doi: 10.1109/TMECH.2021.3068599.

[91] H. Lim and S. Hoag. Plasticizer effects on physical–mechanical properties of solvent cast soluplus films. *AAPS PharmSciTech*, 14, 05 2013. doi: 10.1208/s12249-013-9971-z.

[92] Y. Lin, H. Zhao, and H. Ding. Posture optimization methodology of 6r industrial robots for machining using performance evaluation indexes. *Robotics and Computer-Integrated Manufacturing*, 48:59–72, 12 2017. doi: 10.1016/j.rcim.2017.02.002.

[93] W. Linder. *Digital photogrammetry*, volume 1. Springer, 2009.

[94] T. Lozano-Perez, J. Jones, E. Mazer, P. O'Donnell, W. Grimson, P. Tournassoud, and A. Lanusse. Handey: A robot system that recognizes, plans, and manipulates. In *Proceedings. 1987 IEEE International Conference on Robotics and Automation*, volume 4, pages 843–849, 1987. doi: 10.1109/ROBOT.1987.1087847.

[95] R. K. Malhan, A. M. Kabir, B. Shah, and S. K. Gupta. Identifying feasible workpiece placement with respect to redundant manipulator for complex manufacturing tasks. In *2019 International Conference on Robotics and Automation (ICRA)*, pages 5585–5591, 2019. doi: 10.1109/ICRA.2019.8794353.

[96] W. Matschinsky. *Radführungen der Straßenfahrzeuge: Kinematik, Elasto-Kinematik und Konstruktion*. Springer, 1998. ISBN 9783540641551.

[97] X. Meng, Y. Sun, J. He, W. Li, and Z. Zhou. Multi-objective lightweight optimization design of the aluminium alloy front subframe of a vehicle. *Metals*, 13:705, 04 2023. doi: 10.3390/met13040705.

[98] C. Mineo, S. G. Pierce, P. I. Nicholson, and I. Cooper. Robotic path planning for non-destructive testing – a custom matlab toolbox approach. *Robotics and Computer-Integrated Manufacturing*, 37:1–12, 2016. ISSN 0736-5845. doi: https://doi.org/10.1016/j.rcim.2015.05.003. URL https://www.sciencedirect.com/science/article/pii/S0736584515000666.

[99] Mitsubishi Electric Corporation. Industrial Robots MELFA, 2023. URL https://www.mitsubishielectric.com/fa/products/rbt/robot/pmerit/option/force/index.html. (accessed on: 09.08.2023).

[100] MTS Systems. Multi-Axial Simulation Table (MAST) Systems, 2022. URL https://www.mts.com/en/products/automotive/subsystem-component-test-systems/multi-axial-simulation-table-systems. (accessed on 25.06.2023).

[101] J. Nam, H. Shin, and G.-J. Choi. Durability prediction for automobile aluminum front subframe using nonlinear models in virtual test simulations. *International Journal of Automotive Technology*, 15, 06 2014. doi: 10.1007/s12239-014-0062-2.

[102] P. Neto and N. Mendes. Direct off-line robot programming via a common cad package. *Robotics and Autonomous Systems*, 61(8):896–910, 2013. ISSN 0921-8890. doi: https://doi.org/10.1016/j.robot.2013.02.005. URL https://www.sciencedirect.com/science/article/pii/S0921889013000419.

[103] M. Nierenberger, M. Poncelet, S. Pattofatto, A. Hamouche, B. Raka, and J. Virely. Multiaxial testing of materials using a stewart platform: Case study of the nooru-mohamed test. *Experimental Techniques*, 38(2):74–83. doi: https://doi.org/10.1111/j.1747-1567.2012.00807.x.

[104] Nissan Motor Co., Ltd. Domo arigato, Mrs. Doorboto, 2023. URL https://usa.nissannews.com/en-US/releases/domo-arigato-mrs-doorboto. (accessed on: 16.05.2023).

[105] OASIS Open. MQTT Version 5.0 OASIS Standard, 2019. URL https://docs.oasis-open.org/mqtt/mqtt/v5.0/mqtt-v5.0.html. (accessed on: 15.08.2023).

[106] OPC Foundation. Unified Architecture, 2023. URL https://opcfoundation.org/about/opc-technologies/opc-ua/. (accessed on: 15.08.2023).

[107] Y. Pan. Subframe structural strength and modal analysis of a car and structure modification. *Jixie Qiangdu/Journal of Mechanical Strength*, 39:1490–1494, 12 2017. doi: 10.16579/j.issn.1001.9669.2017.06.039.

[108] Z. Pan, J. Polden, N. Larkin, S. V. Duin, and J. Norrish. Recent progress on programming methods for industrial robots. In *ISR 2010 (41st International Symposium on Robotics) and ROBOTIK 2010 (6th German Conference on Robotics)*, pages 1–8, 2010.

[109] M. Paulweber and K. Lebert. *Prüfstandstypen*, pages 11–108. Springer Fachmedien Wiesbaden, Wiesbaden, 2014. ISBN 978-3-658-04453-4. doi: 10.1007/978-3-658-04453-4_2. URL https://doi.org/10.1007/978-3-658-04453-4_2.

[110] L. Perez, S. Rodríguez-Jiménez, N. Rodríguez, R. Usamentiaga, and F. D. Garcia. Digital twin and virtual reality based methodology for multi-robot manufacturing cell commissioning. *Applied Sciences*, 10:3633, 05 2020. doi: 10.3390/app10103633.

[111] S. Pischinger and U. Seiffert. Gesamtfahrzeug. In *Vieweg Handbuch Kraftfahrzeugtechnik*, pages 125–167, 98–199, 211, 261–279, 306–307, 338–343, 360–440, 726–728. Springer, 2021.

[112] J. Postel and J. K. Reynolds. Telnet protocol specification. Technical report, 1983.

[113] L. Regenwetter, C. Weaver, and F. Ahmed. Framed: An automl approach for structural performance prediction of bicycle frames. *Computer-Aided Design*, 156:103446, 2023. ISSN 0010-4485. doi: https://doi.org/10.1016/j.cad.2022.103446. URL https://www.sciencedirect.com/science/article/pii/S0010448522001798.

[114] X. Ren, X. Xu, F. Yuan, Z. Yin, and X. He. Semantic speckle: A novel auto-located speckle pattern for dic measurement. *Applied Optics*, 61, 07 2022. doi: 10.1364/AO.465070.

[115] S. Rizvi, S. Agrawal, and Q. Murtaza. Automotive industry and industry 4.0-circular economy nexus through the consumers' and manufacturers' perspectives: A case study. 07 2023. doi: 10.1016/j.rser.2023.113517.

[116] T. Sakata and S. Kawai. Dynamic bending analysis of snowboards. *Transactions of the Japan Society of Mechanical Engineers Series C*, 61:1469–1475, 04 1995. doi: 10.1299/kikaic.61.1469.

[117] K. Schiebold. *Zerstörende Werkstoffprüfung: Metallographische Werkstoffprüfung und Dokumentation der Prüfergebnisse*. Springer-Verlag, 2018.

[118] SCPI Consortium. Standard commands for programmable instruments (SCPI), 1999. URL http://www.ivifoundation,org/docs/SCPI-99.pdf. (accessed on: 16.05.2023).

[119] J. Sellors. Titanium rear subframe bonded titanium structures. *Journal of light metal welding*, 53:442–447, 11 2015.

[120] B. Siciliano, L. Sciavicco, L. Villani, and G. Oriolo. Robotics: Modelling, Planning and Control. 2010.

[121] B. Siciliano, O. Khatib, and T. Kröger. *Springer handbook of robotics*. Springer, 2016.

[122] I. M. Smith. Numerical methods in finite element analysis, k.-j. bathe and e. l. wilson, prentice-hall inc., englewood cliffs, n.j., 1976. *International Journal for Numerical and Analytical Methods in Geomechanics*, 1(3), 1977. doi: https://doi.org/10.1002/nag.1610010308.

[123] Sourav, A. Sharma, and M. Pandey. Material selection and analysis of bicycle frame. In J. Singh, S. Kumar, and U. Choudhury, editors, *Innovations in Cyber Physical Systems*, pages 771–780, Singapore, 2021. Springer Singapore.

[124] A. Subic, P. Clifton, J. Beneyto Ferre, A. LeFlohic, Y. Sato, and V. Pichon. Investigation of snowboard stiffness and camber characteristics for different riding styles. *Sports Engineering*, 11:93–101, 02 2009. doi: 10.1007/s12283-008-0008-x.

[125] A. Subic, P. Clifton, J. Kovacs, F. Mylonas, and A. Rochefort. Experimental installation for evaluation of snowboard simulated onsnow dynamic performance. *Procedia Engineering*, 2:2605–2611, 06 2010. doi: 10.1016/j.proeng.2010.04.039.

[126] Technische Universität Hamburg. Hexapod Prüfanlage, 2023. URL `https://www.tuhh.de/hexapod/startseite.html`. (accessed on 25.06.2023).

[127] M. Tekieli, S. De Santis, G. Felice, A. Kwiecień, and F. Roscini. Application of digital image correlation to composite reinforcements testing. *Composite Structures*, 160:670–688, 12 2017. doi: 10.1016/j.compstruct.2016.10.096.

[128] D. Toal, C. Flanagan, C. Jones, and B. Strunz. Subsumption architecture for the control of robots. *Proceedings Polymodel-16*, 01 1995.

[129] J. Vanwalleghem, I. De Baere, M. Loccufier, and W. Van Paepegem. Development of a test rig and a testing procedure for bicycle frame stiffness measurements. *Sports Engineering*, 21, 09 2017. doi: 10.1007/s12283-017-0248-8.

[130] D. Wagner, D. Mainz, T. Gerhards, and X. Chen. Carbon fiber composite chassis components, opportunities and challenges. 09 2021. doi: 10.46720/f2020-mml-059.

[131] H.-F. Wang and Y.-L. Zhang. Cad/cam integrated system in collaborative development environment. *Robotics and Computer-Integrated Manufacturing*, 18(2):135–145, 2002. ISSN 0736-5845. doi: https://doi.org/10.1016/S0736-5845(01)00027-8. URL `https://www.sciencedirect.com/science/article/pii/S0736584501000278`.

[132] Y. Wang, J. Jiang, C. Wanintrudal, C. Du, D. Zhou, L. Smith, and L. Yang. Whole field sheet-metal tensile test using digital image correlation. *Experimental Techniques - EXP TECH*, 34:54–59, 03 2010.

[133] T. Weingartshofer, C. Hartl-Nesic, and A. Kugi. Optimal tcp and robot base placement for a set of complex continuous paths. pages 9659–9665, 05 2021. doi: 10.1109/ICRA48506.2021.9561900.

[134] D. Weyns and T. Holvoet. From reactive robotics to situated multiagent systems: A historical perspective on the role of environment in multiagent systems. volume 3963, pages 63–88, 10 2005. ISBN 978-3-540-34451-3. doi: 10.1007/11759683_5.

[135] F. Wolfsperger and H. Rhyner. Mechanical and dynamical properties of racing snowboards and their modification by different binding plates. *Procedia Engineering*, 72:356–361, 12 2014. doi: 10.1016/j.proeng.2014.06.062.

[136] Y. Xia, L. Zhao, Z. Liu, and K. Zhu. Optimization of machining position for wheel hub polishing robot based on the kinematic index. In *2022 8th International Conference on Control, Automation and Robotics (ICCAR)*, pages 155–160, 2022. doi: 10.1109/ICCAR55106.2022.9782642.

[137] C. Zheng, Y. An, Z. Wang, H. Wu, X. Qin, B. Eynard, and Y. Zhang. Hybrid offline programming method for robotic welding systems. *Robotics and Computer-Integrated Manufacturing*, 73:102238, 2022. ISSN 0736-5845. doi: https://doi.org/10.1016/j.rcim.2021.102238. URL `https://www.sciencedirect.com/science/article/pii/S0736584521001198`.

[138] ZwickRoell GmbH & Co. KG. roboTest R Robotic Testing System, 2023. URL `https://www.zwickroell.com/products/automated-testing-systems/robotest-r-robotic-testing-system/`. (accessed on 12.06.2023).

[139] ZwickRoell GmbH & Co. KG. Biaxial Testing Machine for Biomaterials, 2023. URL https://www.zwickroell.com/products/static-materials-testing-machines/biaxial-and-triaxial-testing-machines/biaxial-testing-machine-for-biomaterials. (accessed on 12.06.2023).

[140] ZwickRoell GmbH & Co. KG. Cruciform Testing Machines, 2023. URL https://www.zwickroell.com/products/static-materials-testing-machines/biaxial-and-triaxial-testing-machines/testing-machines-for-cruciform-tests/. (accessed on 12.06.2023).

[141] ZwickRoell GmbH & Co. KG. Torsion Testers, 2023. URL https://www.zwickroell.com/products/static-materials-testing-machines/biaxial-and-triaxial-testing-machines/torsion-testers/. (accessed on 12.06.2023).

List of Figures

List of Tables

Supervised Student Research Projects and Theses

Lukas Kilian. “Generierung einer automatischen Prüfbewegung zur Komponentenprüfung”. Bachelor Thesis. University of Augsburg, 2022

Tobias Thiele. “Simulation von kraftgeregelten Bewegungen von Industrierobotern”. Bachelor Thesis. University of Augsburg, 2023

Maximilian Enrico Müller. “Berechnung eines Kräftemodells zur automatisierten Bauteilplatzierung für die roboter-basierte Komponentenprüfung”. Internship Project. University of Augsburg, 2023

Tobias Hofstetten. “Implementierung und Evaluation von Fusionierungsmechanismen von Sensordaten mittels OPC UA PubSub”. Internship Project. University of Augsburg, 2023

Moritz Lachenmayer. “Erstellung eines dig. Zwillings für eine selbstorganisierende Produktionsanlage”. Internship Project. University of Augsburg, 2023

Maximilian Enrico Müller. “Robarista: Orchestrierung von Anlagen- und Roboterfähigkeiten für eine Barista Anwendung”. Bachelor Thesis. University of Augsburg, 2023

Own Publication

1. Julian Hanke, Matthias Stüben, Christian Eymüller, Maximilian Enrico Müller Alexander Poeppel and Wolfgang Reif "CASP: Computer Aided Specimen Placement for Robot-Based Component Testing" In 2023 Proceedings of the 20th International Conference on Informatics in Control, Automation and Robotics (ICINCO).
2. Julian Hanke, Christian Eymüller, Alexander Poeppel, Julia Reichmann, Anna Trauth, Markus Sause and Wolfgang Reif "Sensor-guided motions for robot-based component testing" In 2022 Sixth IEEE International Conference on Robotic Computing (IRC).
3. Julian Hanke, Christian Eymueller, Julia Reichmann, Anna Trauth, Markus Sause and Wolfgang Reif "Software-defined testing facility for component testing with industrial robots" In 2022 IEEE 27th International Conference on Emerging Technologies and Factory Automation (ETFA).
4. Julian Hanke, Oliver Kosak, Alexander Schiendorfer and Wolfgang Reif "Self-organized resource allocation for reconfigurable robot ensembles" In 2018 IEEE 12th International Conference on Self-Adaptive and Self-Organizing Systems (SASO).
5. Christian Eymüller, Julian Hanke, Alwin Hoffmann, Markus Kugelmann, and Wolfgang Reif. "Real-time capable OPC-UA Programs over TSN for distributed industrial control". In 2020 25th IEEE International Conference on Emerging Technologies and Factory Automation (ETFA), volume 1, pages 278–285, 2020.
6. Christian Eymüller, Julian Hanke, Alwin Hoffmann, Alexander Poeppel, Constantin Wanninger, and Wolfgang Reif. "Towards a Real-Time Capable Plug & Produce Environment for Adaptable Factories". In 2021 26th IEEE International Conference on Emerging Technologies and Factory Automation (ETFA), pages 1–4, 2021.
7. Christian Eymüller, Julian Hanke, Alwin Hoffmann, Wolfgang Reif, Markus Kugelmann, and Florian Grätz. "RealCaPP: Real-time capable Plug & Produce communication platform with OPC UA over TSN for distributed industrial robot control". In 2021 IEEE 17th International Conference on Automation Science and Engineering (CASE), pages 585–590, 2021.
8. Christian Eymüller, Julian Hanke, Alexander Poeppel, and Wolfgang Reif. "Towards Self-Configuring Plug & Produce Robot Systems Based on Ontologies". In 2023 9th International Conference on Automation, Robotics and Applications (ICARA), pages 23–27, 2023.